CARBON NANOMATERIAL-BASED BIOSENSING

by

Yanan Chen

B.S. in Chemistry, Nanjing University, 2007

Submitted to the Graduate Faculty of

the Kenneth P. Dietrich School of

Arts and Sciences in partial fulfillment

of the requirements for the degree of

Doctor of Philosophy

University of Pittsburgh

2013

UNIVERSITY OF PITTSBURGH

the Dietrich Graduate School of Arts and Sciences

This dissertation was presented

by

Yanan Chen

It was defended on

January 9, 2013

and approved by

Dr. Ren ã A. S. Robinson, Assistant Professor, Department of Chemistry

Dr. Adrian Michael, Professor, Department of Chemistry

Dr. Steven R. Little, Associate Professor, Department of Chemical and Petroleum Engineering

Dissertation Advisor: Dr. Alexander Star, Associate Professor, Department of Chemistry

CARBON NANOMATERIAL-BASED BIOSENSING

Yanan Chen, PhD

University of Pittsburgh, 2013

Carbon nanomaterials, including carbon nanotubes (CNTs) and graphene, are exciting materials that have been the focus of research in recent years. They have unique physical and chemical properties such as high carrier mobility, high surface-to-volume ratio, and robustness, and are thus considered to be ideal candidates to interact with biological systems. However, the pristine carbon nanomaterials usually suffer from the lack of solubility in aqueous systems. Furthermore, these materials are extremely sensitive to any change in their immediate environment, so it is necessary to decorate these materials with receptor molecules to provide specificity. Therefore the chemical functionalizations of carbon nanomaterials are important before such materials can be incorporated into biosensing devices. There are commonly two approaches of functionalizing carbon nanomaterials, namely covalent and noncovalent methods. Covalent functionalization can provide robust chemical groups onto the surface of carbon nanomaterials. However, this method may disrupt the sp^2 structure of carbon nanomaterials and affect the electronic properties of these materials. Noncovalent functionalization can bring the desired functionalization while maintaining the intrinsic electronic properties intact, but leaching of the absorbed materials may be a problem.

In this dissertation, both methods have been used to functionalize carbon nanomaterials towards biosensors. Using noncovalent functionalization scheme, we built two sensing platforms. We used epigallocatechin gallate (EGCG) to noncovalently attach to the surface of

single-walled carbon nanotubes (SWNT) and fabricated a resistor-based sensor for hydrogen peroxide. Using porphyrin-based glycoconjugate, we explored the sensitivity of SWNT/glycoconjugate composites towards lectins. Lectins are sugar-binding proteins that exist on the surface of bacteria. Sensing of lectins may lead to the development of bacteria detectors. Furthermore, to explore an optimized system for lectin sensing, we used SWNTs and graphene, as well as different glycoconjugates. It was found out that SWNTs performed better than chemically converted graphene (CCG). Although CCG was not suitable for sensing of lectins using noncovalent functionalization, holey reduced graphene oxide (hRGO), with its interconnected graphene nanoribbon structure and abundant oxygen-containing groups, may be a good platform for biosensing. The functionalization of these groups with antimicrobial peptide can provide specificity to certain bacteria, towards the fabrication of a bacteria detector.

TABLE OF CONTENTS

PREFACE ..... **XX**

1.0 INTRODUCTION **1**

1.1 BIOSENSORS **1**

1.2 CARBON NANOMATERIALS AND THEIR APPLICATIONS **3**

1.2.1 Carbon nanotubes and graphene **3**

1.2.2 Methods of Chemical Functionalization – Noncovalent and Covalent **7**

1.2.3 The Applications of Carbon Nanomaterials in Biosensors **11**

2.0 EXPLORING THE CHEMICAL SENSITIVITY OF A CARBON NANOTUBE/GREEN TEA COMPOSITE **16**

2.1 CHAPTER PREFACE **16**

2.2 INTRODUCTION **17**

2.3 EXPERIMENTAL **18**

2.4 RESULTS AND DISCUSSION **21**

2.5 CONCLUSIONS **34**

2.6 ACKNOWLEDGEMENT **35**

2.7 SUPPORTING INFORMATION **35**

3.0 NANOELECTRONIC DETECTION OF LECTIN-CARBOHYDRATE INTERACTIONS USING CARBON NANOTUBES **43**

3.1 CHAPTER PREFACE 43

3.2 INTRODUCTION 44

3.3 EXPERIMENTAL 47

3.4 RESULTS AND DISCUSSION 50

3.5 CONCLUSIONS 59

3.6 ACKNOWLEDGEMENT 59

3.7 SUPPORTING INFORMATION 60

4.0 ELECTRONIC DETECTION OF LECTINS USING CARBOHYDRATE FUNCTIONALIZED NANOSTRUCTURES:

GRAPHENE *VERSUS* CARBON NANOTUBES 63

4.1 CHAPTER PREFACE 63

4.2 INTRODUCTION 64

4.3 EXPERIMENTAL 66

4.4 RESULTS AND DISCUSSION 69

4.5 CONCLUSIONS 88

4.6 ACKNOWLEDGEMENT 88

4.7 SUPPORTING INFORMATION 89

5.0 CARBON NANOMATERIALS FOR BACTERIA DETECTION 98

5.1 CHAPTER PREFACE 98

5.2 INTRODUCTION 99

5.3 EXPERIMENTAL 100

5.4 RESULTS AND DISCUSSION 103

5.5 CONCLUSIONS 115

6.0 SUMMARY AND FUTURE WORK 116

BIBLIOGRAPHY 118

LIST OF TABLES

Table 4-1. Glycoconjugates used in this study with their respective specific and control (non-specific) lectins 72

Table 4-2. Comparison of K_d values obtained by FET and ITC methods..... 86

LIST OF FIGURES

Figure 1-1. Schematic diagram showing the basic components of a biosensor..... 2

Figure 1-2. (a) Conceptual analogy of carbon nanotube (CNT) formation by "rolling up" of a single sheet of graphene and (b) graphene sheet demonstrating "roll-up" vectors (n, m).[18] 5

Figure 1-3. (a) Covalent functionalization schemes of CNTs using amidation or azomethine ylide cycloaddition[27]; (b) Schematic showing various covalent functionalization chemistry of graphene or GO.[30] 8

Figure 1-4. Noncovalent functionalization schemes for (a) SWNT [31] and (b) graphene [30] 10

Figure 1-5. (a) Schematic representation of SWNT FET biosensors,[4b] (b) Schematic illustration of a glucose oxidase (GOD) functionalized CVD-graphene device for detection of glucose. [41] . 12

Figure 1-6. (a) AFM image of holey reduced graphene oxide (hRGO) and (b) conductivity versus potential (liquid gate) plot for RGO (black circles) and hRGO (solid red line). [22] 14

Figure 2-1. (a) Chemical structure of epigallocatechin gallate (EGCG). (b) Photograph of four vials with green tea (left), SWNT and green tea (middle left), 4.4×10^{-4} M EGCG sonicated with ca. 1 mg of SWNTs (middle right) and SWNTs in water (right). (c) UV-Vis-NIR absorption spectra of SWNT (black), EGCG (green), and SWNT/EGCG (red) as thin films on quartz. Inset displays a photograph of transparent SWNT/EGCG conductive film on a quartz slide. (d) FTIR

spectrum of bare SWNTs (black), EGCG in MeOH (4×10^{-4} M) (green) and SWNT/EGCG composite after heating at 140 ℃ for 20 min (red). 22

Figure 2-2. (a) Schematic illustration of SWNT/EGCG composite device. (b) Optical images and scanning electron microscope (SEM) image of the SWNT/EGCG film deposited on CERDIP package with Si chip containing four interdigitated Au electrodes. (c) Relative conductance versus time dependence of four interdigitated devices (shown in different colors) coated with SWNT/EGCG composite cycled between H_2O_2 and H_2O vapor pulses (H_2O_2 concentration was calculated as 45 ppm). (d) Relative conductance versus time dependence of four interdigitated devices coated with SWNT/EGCG composite cycled between dry N_2 and N_2 bubbled through different saturated salt solutions generating different levels of relative humidity (%)..... 25

Figure 2-3. Relative conductance versus time response to varying concentrations of H_2O_2 of (a) SWNT/EGCG pre-mixed composite, (b) of bare SWNT device, (c) of SWNT/EGCG layer-by-layer composite, (d) SWNT/EGCG/(Fe_2O_3 nanoparticles) layer-by-layer composite and (e) SWNT/(Fe_2O_3 nanoparticles) layer-by-layer composite. Insets show the schematic device architectures. (f) Relative conductance change vs. concentration plot of SWNT/EGCG (black) and SWNT/EGCG/(Fe_2O_3 nanoparticles) (red). (g) Fenton's catalysis mechanism includes the coordination of Fe^{3+} by polyphenols in EGCG, subsequent iron reduction and semiquinone formation, and reduction of Fe^{3+} to form a quinone species and Fe^{2+} (reaction 1). H_2O_2 is reduced by Fe^{2+}, resulting in the formation of •OH radical (reaction 2). (Ref [74])..... 29

Figure 2-4. (a) Chemical structures of possible oxidation products of EGCG with H_2O_2 (Ref [79] and [77b]). (b) FTIR spectrum of SWNT/EGCG composite before (black) and after exposure to 10^{-2} M H_2O_2 (Red). 32

Figure 2-5. (a) Schematic illustration of the liquid-gate FET testing device setup. (b) Current versus liquid gate potential curves of SWNT/green tea composite device acquired before (black solid) and after adding 10^{-4} M (red dot), 10^{-3} M (blue dash) and 10^{-2} M (green dot dash) H_2O_2. (c) Threshold voltage shift versus H_2O_2 concentration plot. 33

Figure 3-1. (a) Schematic illustration of glycoconjugate-functionalized single-walled carbon nanotubes (SWNTs)-FET for selective detection of lectins. (b) Chemical structure of porphyrin-based glycoconjugates for noncovalent functionalization of SWNTs. Table shows the selected glycoconjugates and their specific lectins and controls. (c) Optical image of a Si/SiO_2 chip with micropatterned interdigitated electrodes. SEM image of interdigitated electrodes used for device fabrication. Inset shows the SWNTs deposited by dielectrophoresis technique between the microelectrodes. 46

Figure 3-2. Electronic detection of carbohydrate-lectin interactions: Conductance (G) vs gate voltage (V_g) of bare NTFET device, after functionalization with (a) β-D-galactose, (b) α-D-mannose, (c) α-L-fucose and after attachment with 2 μM selective lectin and their controls. (d) Same experiment as in panel (a) with PA-IIL as control and varying concentration of the selective lectin (PA-IL) (2 nM-10 μM). Inset shows the biosensor calibration plot: normalized change in the device conductance versus PA-IL concentration. (e) Langmuir isotherm of data presented in panel (d) with calculated lectin dissociation constant (K_d). Lectin binding experiments were performed in the presence of 5 μM Ca^{2+}. (f) Fluorescence image of ConA-Alexa 488 attached on α-D-mannose (left panel) and α-L-fucose (right panel) functionalized SWNTs. 51

Figure 3-3. (a) G vs V_g curves for bare SWNT, after ZnTTP functionalization (without glycoconjugate) and after ConA (mannose specific lectin)(green). (b) UV-vis absorption spectra

of pristine SWNTs, after functionalization with α-D-mannose and after ConA (mannose specific lectin). 53

Figure 3-4. Atomic force microscope images of (a) bare SWNTs, (b) SWNT functionalized with α-D-mannose glycoconjugate, and (c) after ConA attachment. Lectin attachment was performed in the presence of 5 μM Ca^{2+}. 58

Figure 4-1. (a) Optical image of wirebonded Si chip with multiple photolithography patterned Au/Ti electrodes. Inset shows scanning electron microscopy (SEM) image of one set of the interdigitated electrodes (left, SWNT-FET; right, CCG-FET). (b) Schematic illustration of the liquid-gated FET configuration (left, SWNT-FET; right, CCG-FET). (c, d) Nanoelectronic detection of carbohydrate-lectin interactions: Conductance (G) vs gate voltage (Vg) of (c) bare SWNT-FET and (d) bare CCG-FET device device after functionalization with β-D-galactose pyrene-based glycoconjugates (1a) and after attachment with 2 μM non-specific (control) lectin ConA and 2 μM specific lectin PA-IL. (e) Comparison of the normalized responses (Vg = –0.5 V) to 2 μM control lectin and to 2 μM specific lectin for biosensors: SWNT+1a, 1b, 1c or 2a, 2b, 2c, CCG+1a, 1b, 1c or 2a, 2b, 2c. All measurements were performed in electrolyte-gated FET configuration in PBS (pH 7), Ag/AgCl reference electrode, with source-drain voltage of 50 mV. Lectin binding experiments were performed in the presence of 5 μM Ca^{2+}..... 73

Figure 4-2. Computer-aided models of (a) SWNT/1a/PA-IL interaction, (b) SWNT/2a/PA-IL interaction, (c) CCG/ 1a/PA-IL interaction, and (d) CCG/ 2a/PA-IL interaction. 78

Figure 4-3. Atomic force microscope (AFM) images of (a) bare SWNTs, (b) SWNT functionalized with 1b, (c) after incubation with PA-IL (control) and (d) after ConA attachment; (e) bare CCG, (f) CCG functionalized with 1b, (g) after incubation with PA-IL (control) and (h) after ConA attachment. Lectin attachment was performed in the presence of 5 μM Ca^{2+}. 80

Figure 4-4. Fluorescence image of α-D-mannose glycoconjugates functionalized SWNT-FET device incubated with fluorescently-labeled lectin ConA-Alexa488. 83

Figure 4-5. Biosensor calibration plot: normalized change in the device conductance (V_g = –0.5 V) *versus* PA-IL concentration of (a) SWNT-FET and (c, e) CCG-FET (data from three devices). Langmuir isotherm of (b) SWNT-FET data presented in panel (a), (d) for CCG-FET with their corresponding calculated lectin dissociation constants (K_d). (f) Langmuir isotherm of CCG/1c and PA-IIL interaction, with calculated lectin dissociation constant K_d. 85

Figure 4-6. Titration of (a) PA-IL (0.05 mM) by compound 1a (1.7 mM) and (b) titration of PA-IIL (0.05 mM) by compound 1c (0.5 mM). Top: control (injection of glycocompound in buffer), middle: titration of lectin, bottom: integration of peaks with a fitting curve obtained from a two site model. 86

Figure 5-1. Schematic illustration of AMP functionalized hRGO-FET for selective detection of bacterial cells. 103

Figure 5-2. Electronic detection of bacteria-AMP interactions. Conductance (G) vs gate voltage (V_g) of bare hRGO FET device, after functionalization with AMP, after incubation with blocking buffer and after incubation with (a) 10^7 cfu/mL *E. coli* O157:H7 and (b) 10^7 cfu/mL *Salmonella typhimurium.* 105

Figure 5-3. Control experiment with nonspecific bacteria. Conductance (G) vs gate voltage (V_g) of bare hRGO FET device, after functionalization with AMP, after incubation with blocking buffer and after incubation with (a) 10^7 cfu/mL *Listeria*, (b) 5 μM BSA. 107

Figure 5-4. Comparison of the normalized responses (V_g=-0.5V) of Magaini I functionalized hRGO FET devices to controls: 10^7 cfu/mL of *Listeria* and 5 μM BSA; and specifics: 10^7 cfu/mL of *E.coli* O157:H7 and *Salmonella*. 108

Figure 5-5. Electronic detection, control experiments. Conductance (G) vs gate voltage (V_g) of bare rHGO FET device, (a) after incubation with blocking buffer and after attachment with 10^7 cfu/mL *E. coli* O157:H7 , (b) after incubation with AMP without the carboxylic group activation step, after incubation with blocking buffer and after incubation with 10^7 cfu/mL *E. coli* O157:H7..... 110

Figure 5-6. Comparison of the normalized responses (V_g=-0.5V) of hRGO FET devices to controls: 10^7 cfu/mL of *E.coli* O157:H7: Bare hRGO FET without AMP functionalization step, hRGO FET incubated with AMP solution overnite without EDC/NHS activation step, hRGO FET functionalized with AMP with EDC/NHS activation..... 111

Figure 5-7. (a) SEM image of the functionalized device surface after incubation with *E. coli* O157:H7. (b) AFM image showing the attachment of bacteria to hRGO surface. 112

Figure 5-8. (a) Conductance (G) vs gate voltage (V_g) of bare P3-SWNT FET device, after incubation with blocking buffer and after incubation with 10^7 cfu/mL *E. coli* O157:H7, (b) comparison of the normalized responses (V_g=-0.5V) of Magaini I functionalized hRGO FET devices and P3-SWNT FET to specific bacteria: 10^7 cfu/mL of *E.coli* O157:H7..... 114

LIST OF SUPPORTING FIGURES

Figure-S 2-1. TGA of SWNT (black), EGCG (green) and SWNT/EGCG composite (red). 36

Figure-S 2-2. Raman spectra of pristine SWNTs (black) and SWNT/EGCG composite (red)... 36

Figure-S 2-3. (a) AFM image of SWNTs treated with 4.4×10^{-4} M EGCG. Section analysis reveals that SWNTs appear 4–9 nm in diameter after modification with EGCG. (b) AFM image of bare SWNTs. Section analysis reveals that bare SWNTs exist as small bundles with diameter around 2 – 6 nm. 37

Figure-S 2-4. Transmission electron microscopy (TEM) images of SWNTs treated with (a) 4.4×10^{-4}M EGCG in water and (b) bare SWNTs in DMF solution (bare SWNTs cannot be dispersed in pure water). 37

Figure-S 2-5. Atomic Force Microscopy (AFM) images of the SWNT/EGCG composite thin film (a) before and (b) after incubation in water for 4 hours. AFM section analysis demonstrates 10% decrease in the film thicknesses from 68 nm to 61 nm after incubation in water, indicating insignificant leaching over the tested time period. (c) Electrical conductance of SWNT/EGCG composite device versus time after addition of water. The device demonstrates a stable baseline while it is immersed in water. (d) Current vs. voltage measurement of bare SWNTs thin film before addition of water (black) and after the added water is dried (red), showing no change in the film conductance. 38

Figure-S 2-6. (a) Relative conductance response versus time dependence of four interdigitated devices coated with bare SWNTs exposed to H_2O_2 vapor pulses. (b) Relative conductance response versus time dependence of three interdigitated devices coated with bare SWNTs and exposed to varying relative humidity pulses. (c) Relative humidity (RH) calibration plot of SWNT/EGCG composite material (black) and bare SWNTs (red). 39

Figure-S 2-7. Optical image depicting the swelling of a SWNT/EGCG composite because of increasing relative humidity (scale in millimetres). 40

Figure-S 2-8. Relative conductance versus time response to varying concentrations of H_2O_2 of SWNT/EGCG/(Fe_2O_3 Nanoparticle) composite. The composite was prepared by mixing and sonicating the components together. 40

Figure-S 2-9. (a) A photograph of transparent and conductive SWNT/EGCG film on a quartz slide. (b) Schematic illustration of thin film. The black arrow shows the direction of the current *i*, *L* is the length of the film and *A* is the cross-sectional area. 42

Figure-S 3-1. G vs Vg data for NTFET devices functionalized (a) with α-D-mannose glycoconjugate and measured after incubation with 2 μM ConA lectin (PA IIL as control) and (b) with α-L-fucose glycoconjugate and measured after attachment with 2 μM selective PA-IIL lectin (Con A as control). Lectin incubations were 40 min and measurements were done in 20 mM PBS (pH 7) with 5 μM Ca^{2+}. V_{ds} = 50 mV. 60

Figure-S 3-2. (a) G vs Vg curves for bare SWNT, glycoconjugate α-D-mannose functionalized SWNT device measured after 2 μM ConA lectin (in PBS(pH 7) with 5 μM Ca^{2+}) solution for 40 min (solid line) and 18 hrs (dashed line). (b) Relative response of a total of 15 different NTFET devices incubated with lectins for 40 min and 18 hrs. NTFET devices were functionalized with α-D-mannose, β-D-galactose and α-D-fucose glycoconjugates for selective detection of 2 μM

PA-IL, PA-IIL and ConA lectins, respectively (in PBS (pH 7) with 5 μM Ca^{2+}). The relative response was measured at Vg = − 0.5 V. 61

Figure-S 3-3. G vs Vg curves measured for bare SWNT, and after 2 μM ConA lectin (in PBS (pH 7) with 5 μM Ca^{2+}) attachment. 62

Figure-S 3-4. Contact angle of water droplet on quartz substrate with (a) spray casted bare SWNT (87°) and after (b) Glycoconjugate (α-D-mannose) functionalization (55 °). 62

Figure-S 4-1. (a) UV-vis-NIR spectra of bare SWNT (black), SWNT functionalized with 1b (red) and after interaction with ConA (blue). (b) UV-vis-NIR spectra of bare CCG (black), CCG functionalized with 1b (red) and after interaction with ConA (blue). 92

Figure-S 4-2. Nanoelectronic detection of carbohydrate-lectin interactions: Conductance (G) vs gate voltage (Vg) of bare SWNT-FET device, after functionalization with (a) α-D-mannose (1b) and (b) α-L-fucose (1c) pyrene-based glycoconjugates and after attachment with 2 μM control lectin and 2 μM specific lectin (in the presence of 5 μM Ca^{2+})..... 93

Figure-S 4-3. Nanoelectronic detection of carbohydrate-lectin interactions: Conductance (G) vs gate voltage (Vg) of bare CCG-FET device, after functionalization with (a) α-D-mannose (1b) and (b) α-L-fucose (1c) pyrene-based glycoconjugates and after attachment with 2 μM non-specific (control) lectin and 2 μM specific lectin (in the presence of 5 μM Ca^{2+}). 93

Figure-S 4-4. Control experiment: (G) vs gate voltage (Vg) of bare CCG FET device, after exposure to 2 μM control lectin ConA (in the presence of 5 μM Ca^{2+}). 94

Figure-S 4-5. Nanoelectronic detection of carbohydrate-lectin interactions: Conductance (G) vs gate voltage (Vg) of bare CCG FET device, after functionalization with (a) β-D-galactose (2a), (b) α-D-mannose (2b), and (c) α-L-fucose (2c) porphyrin-based glycoconjugates and after

attachment with 2 μM non-specific (control) lectin and 2 μM specific lectin (in the presence of 5 μM Ca^{2+}). 95

Figure-S 4-6. (a) Same experiment as in Figure 2c with 10 μM ConA as control and varying concentration of the specific lectin (PA-IL) (2 nM-10 μM). (b) Same experiment as in Figure 2c with 10 μM ConA as control and varying concentration of the specific lectin (PA-IL) (2 nM-10 μM). 96

Figure-S 4-7. Nanoelectronic detection of carbohydrate-lectin interactions: Conductance (G) vs gate voltage (Vg) of bare NTFET device, after functionalization with β-D-galactose prophyrin-based glycoconjugate and after incubation with a mixture solution of 2 μM of PA-IL (specific) and 2 μM of ConA (non-specific) (in the presence of 5 μM Ca^{2+}). Inset shows the comparison between the normalized responses to a pure sample of specific lectin and a mixed sample of specific and non-specific lectins. 97

PREFACE

I first want to thank my research advisor Dr. Alexander Star for his generous help and guidance through my PhD journey. He has been and will be my role-model through my career. I also wish to express my gratitude to my colleagues in the lab and collaborators outside of the lab. They helped me grow by sharing their ideas and experiences with me. Additionally, I want to thank the members of my committee, Dr. Ren ã Robinson, Dr. Adrian Michael and Dr. Steve Little. They inspired me so much over the past three years.

Thanks and loves also go to my dear parents. They encouraged and supported me to pursue my dream. I cannot say enough thank-you to them. I also want to thank my friends for listening to me and comforting me when I felt lost.

Last but not least, I want to thank my dear husband Long Qin, for his unconditional love and support. Without you being there, I could not have come this far. Thank you and love you.

1.0 INTRODUCTION

1.1 BIOSENSORS

Biosensors are analytical tools commonly used to detect biological species, including but not limited to, proteins, DNA, antibodies, and even whole cells.[1] The role of biosensors is to transduce biological processes, such as antibody/antigen interactions, DNA hybridization, or even biochemical reactions, into measurable signals. The concept of biosensor was first introduced by Leland C. Clark.[2] In 1962 he developed an electrochemical biosensor for glucose based on the oxidation of glucose to gluconic acid catalyzed by glucose oxidase (GOD). Since then, researchers in different fields (chemistry, physical, engineering, etc.) have been working on the development and improvement of biosensors.

Biosensors are usually comprised of biological detectors (or receptors), transducers and signal processors[1,3] (Figure 1-1). Biomolecules like proteins, enzymes, antibodies, nucleic acids or even whole cells can be used as biological detectors (receptors). These detectors should have high specificity for the target analytes in complex biological environment. When coupled with transducer, the receptor can generate electrical or optical signals that are proportional to the analyte concentration.

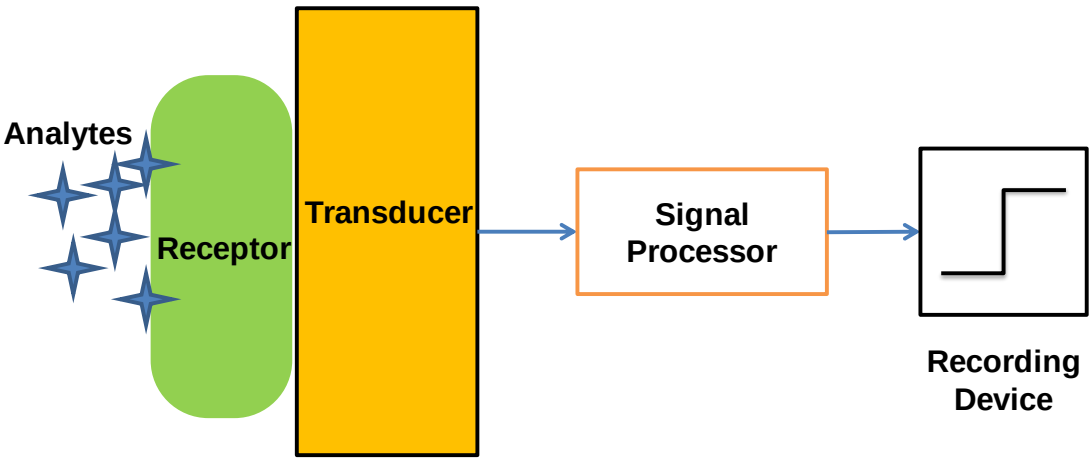

Figure 1-1. Schematic diagram showing the basic components of a biosensor

The existing biosensors include electronic, electrochemical, optical, and thermal sensors.[1] Electronic and electrochemical transducers are based on the current, potential or conductance. [4] Optical sensors transduce the change in absorbance, emission or resonance.[5] Thermal sensors are based on the heat change in the reactions.[6] There is also the relatively newly developed piezoelectric sensors, which are based on the generation of electric current from vibrating crystals by small change in the mass of biomolecule adsorbed on the substrate surface.[7] Among these techniques, electronic sensors have the advantages of low-cost, high sensitivity and easy operation.

Biosensors have been used in the fields of medical diagnostics,[8] food safety,[9] environmental monitoring[10] and biological warfare[11]. Researchers are still searching for more robust, reliable, and simple-to-operate biosensors with high sensitivity and selectivity. Recently, a new trend of using nanomaterials in biosensors has developed. Nanowires, nanoparticles, quantum dots, and carbon nanomaterials have been used for biosensor applications.[12, 13] The exploration of such materials may lead to sensors with better selectivity, sensitivity, and longer operational lifetime.[13]

1.2 CARBON NANOMATERIALS AND THEIR APPLICATIONS

Carbon nanomaterials mainly include fullerenes, single-walled carbon nanotubes, multi-walled carbon nanotubes, and graphene. They are comprised of sp^2 hybridized carbon atoms and can be conceptually visualized as graphene sheet derivatives. Since their discovery, carbon nanomaterials have attracted a lot of attention from researchers all over the world. Their unique properties and versatile chemistry have opened the paths towards various applications. In the work of this dissertation, single-walled carbon nanotubes (SWNTs) and graphene (including its derivatives) have been used for the development of biosensing platforms.

1.2.1 Carbon nanotubes and graphene

An article published in the Soviet *Journal of Physical Chemistry* in 1952 first described the observation of 50 nanometer diameter tubes made of carbon.[14] However, this finding was largely unnoticed, since the article was in the Russian language and was published during the Cold War. Most academic and popular literatures still state that carbon nanotubes were first discovered by Iijima in 1991[15] and he observed multi-walled carbon nanotubes (MWNTs). Two years later, Iijima and Ichihashi of NEC and Bethune and colleagues of the IBM Almaden Research Center in California synthesized single-walled carbon nanotubes (SWNTs).[16] Synthesis of SWNTs can be achieved by several methods including arc discharge, laser ablation, high-pressure carbon monoxide (HiPco), chemical vapor deposition (CVD).[17] Large quantities of carbon nanotubes can be synthesized by these well-developed methods and they are already commercially available.

Single-walled carbon nanotubes contain only one carbon wall and are one-dimensional (1-D) nanomaterials. They can be visualized as an atomically thin layer of sp^2 hybridized carbon, rolled up into a cylinder along an (n, m) lattice vector in the graphene plane (Figure 1-2). The (n,m) indices determine the diameter, chirality and electronic properties of each SWNT. If m=0, the nanotubes are called "zigzag". If n=m, "armchair". If |n-m|=3q, where q is an integer, the SWNTs are metallic, otherwise they are semiconducting. [18]

SWNTs have diameters of about 0.4 to 2.0 nanometers and lengths ranging from several hundred of nanometers up to micrometers.[19] SWNTs have an extraordinarily large percentage of surface atoms, and they are very sensitive to the immediate change in their environment. As a result, they are the ideal materials to transduce biological processes into detectable signals. However, pristine SWNTs are highly hydrophobic and not soluble in aqueous solution, which limited their applications in biological field.

Graphene is a single-layer sheet of sp^2-bonded carbon atoms arranged in a honeycomb lattice (Figure 1-2, a). Ever since the first isolation of free-standing graphene sheets in 2004,[20] their fascinating properties, such as high specific surface area, electronic conductivity, and exceptional mechanical strength, have attracted the attention of the scientific community. [21]

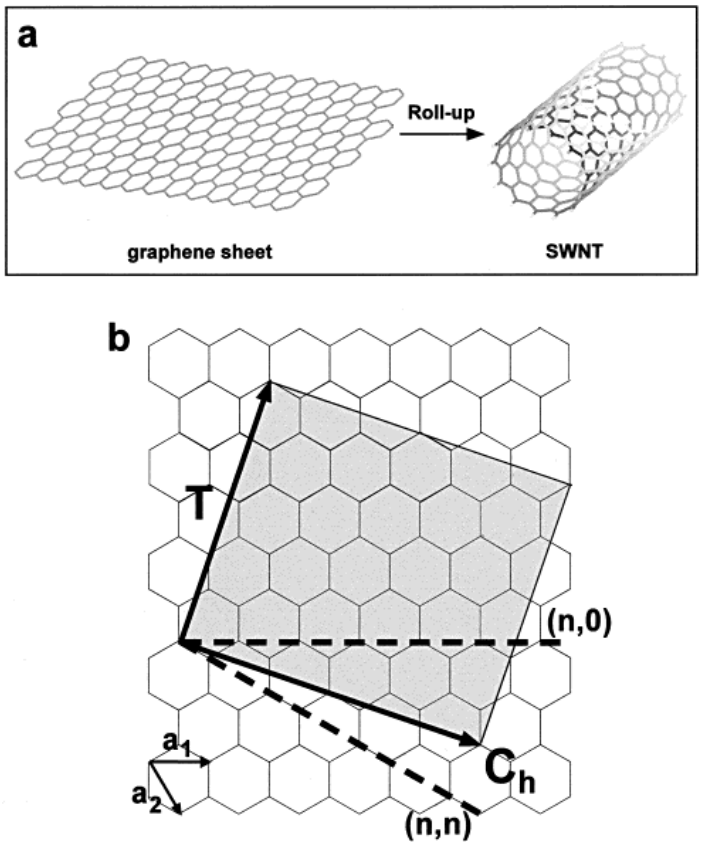

Figure 1-2. (a) Conceptual analogy of carbon nanotube (CNT) formation by "rolling up" of a single sheet of graphene and (b) graphene sheet demonstrating "roll-up" vectors (n, m).[18]

Graphene can be obtained by several methods. A single-layer graphene (SLG) was first obtained by mechanical cleavage of graphite.[20] The pristine single-layer graphene is a semi-metal with zero bandgap. However, mechanical exfoliation is low in throughput and the obtained graphene size is small. Graphene can also be chemically synthesized by exfoliating graphite through oxidation to yield graphite oxide, and this material is then sonicated to produce graphene oxide (GO). Graphene oxide can be subsequently reduced to produce reduced graphene oxide (RGO) (a. k. a. chemically converted graphene (CCG)). [22] This method provides a path for low-cost mass production of graphene. The GO can be reduced by chemical method (hydrazine method), thermal reduction, photothermal reduction, or electrochemical reduction.[23] It must be kept in mind that the RGO obtained by chemical method can be different from the SLG due to the defects in sp^2 carbon lattice and the oxygenated groups caused by oxidation for chemical exfoliation of graphene oxide from graphite. Chemical vapor deposition (CVD) method has also been extensively explored for the growth of graphene film on transition metal substrates.[24] CVD growth can produce large-size graphene for device fabrication and the shape of the film can be controlled. Another advantage is that it allows the in-situ doping of heteroatoms into the carbon lattice and the electronic property of the graphene film can be tuned. However, this method may suffer from the existence of defects, impurities and post-CVD transfer of the graphene film.[23]

GO and RGO have been used for biological applications like biosensing as well as delivery platforms to deliver drug molecules and DNAs.[25] Several types of biosensors have been developed, including fluorescence resonance energy transfer (FRET) based biosensors, field-effect transistor (FET) based biosensors.[23]

1.2.2 Methods of Chemical Functionalization – Noncovalent and Covalent

Covalent functionalization is robust and versatile, and it has been used to functionalize SWNTs for biosensing and drug delivery.[26] One of the most commonly used covalent functionalizations of SWNTs utilizes the carboxylic groups (-COOH) on SWNT sidewalls and ends. The as-produced SWNTs have a small number of carboxylic groups, and –COOH can be additionally introduced by strong acids oxidation.[26, 27] Further introduction of functional groups can be achieved by converting the –COOH to acyl chlorides, following by the direct formation of amide bonds or adding a diamine linker.[26, 27] Carbodiimide activated amidation of amino group-containing molecules with the carboxylic groups on CNTs has also been used as an effective method for functionalization.[28] Oxidized SWNTs can also react with azido-group-containing molecules through Staudinger coupling.[29] Azomethine ylide derivatives have been used to functionalize SWNT through 1,3-dipolar cycloaddition.[26, 27] Diazonium reaction has also shown successful chemical functionalization of SWNTs.[26] (Figure 1-3 a)

GO has abundant functional groups like carboxyl, epoxy and hydroxyl groups that allow further functionalization through reaction including amide formation or amine-epoxy reaction.[30] However, the presence of the oxygen-containing groups on the basal plane of graphene disrupts the π-conjugation and affects the conductivity of graphene. (Figure 1-3 b)

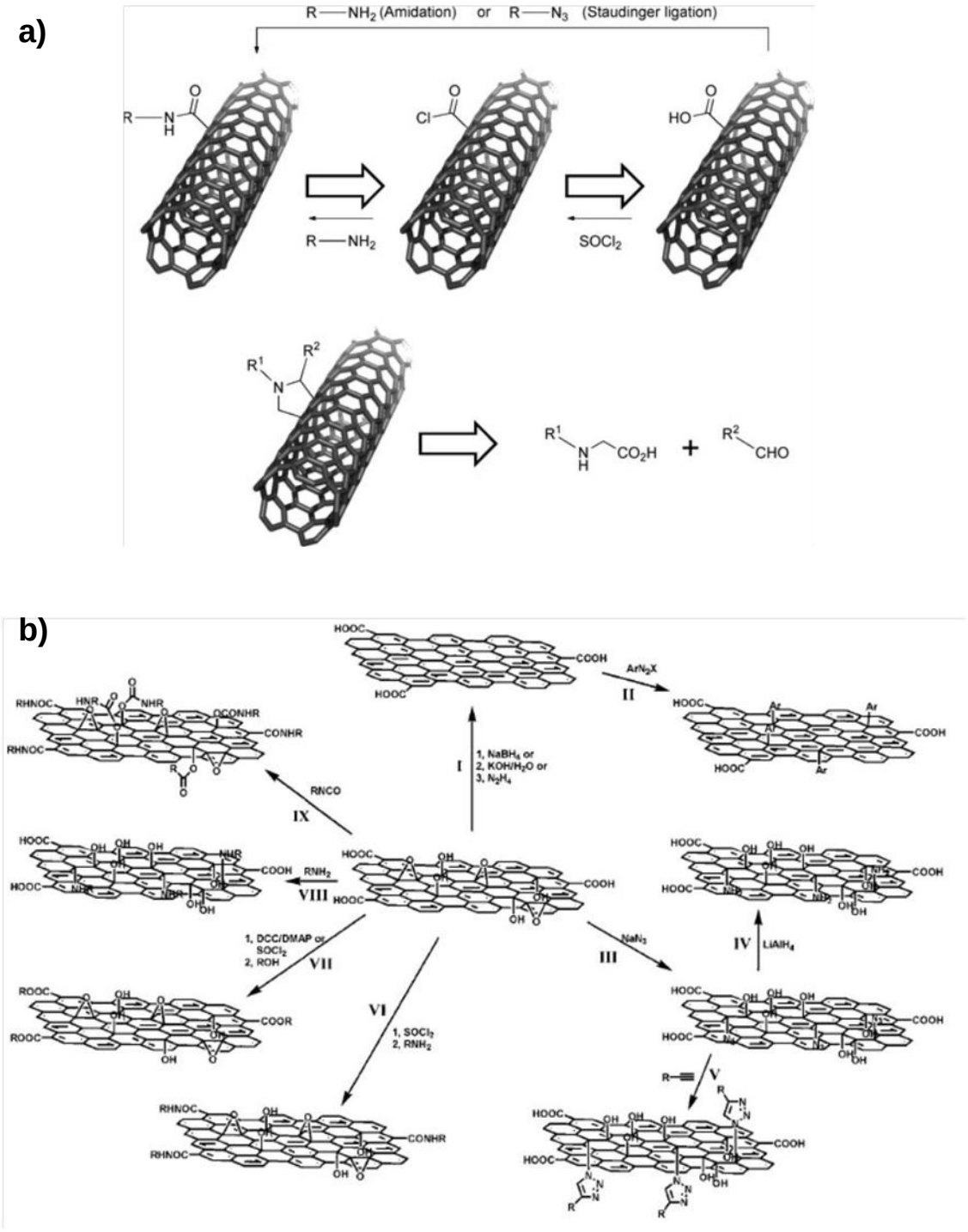

Figure 1-3. (a) Covalent functionalization schemes of CNTs using amidation or azomethine ylide cycloaddition[27]; (b) Schematic showing various covalent functionalization chemistry of graphene or GO.[30]

Despite versatile synthetic opportunities, covalent functionalization methods have certain limitations for biosensor development. Covalent functionalization may disrupt the graphitic structure of SWNT or graphene and affect the intrinsic electronic properties of the nanomaterials. Therefore, noncovalent functionalization is considered as a simple and effective alternative to the covalent methods. Various molecules can be used to noncovalently functionalize SWNTs and graphene via hydrophobic binding or π-π stacking interactions. The advantage of noncovalent functionalization is that it does not create defects on the SWNT or graphene surface and thus preserve their intrinsic electronic properties. Pyrene or porphyrin derivatives have strong affinity to the sidewalls of the SWNT or the graphene surface through π-π stacking by the aromatic moieties (Figure 1-4, a).[31] Surfactants and supermolecular wrapping by polymers are also commonly used for SWNT noncovalent functionalization.[19,32] Graphene can also be functionalized by small molecules or polymers (Figure 1-4, b). [30]

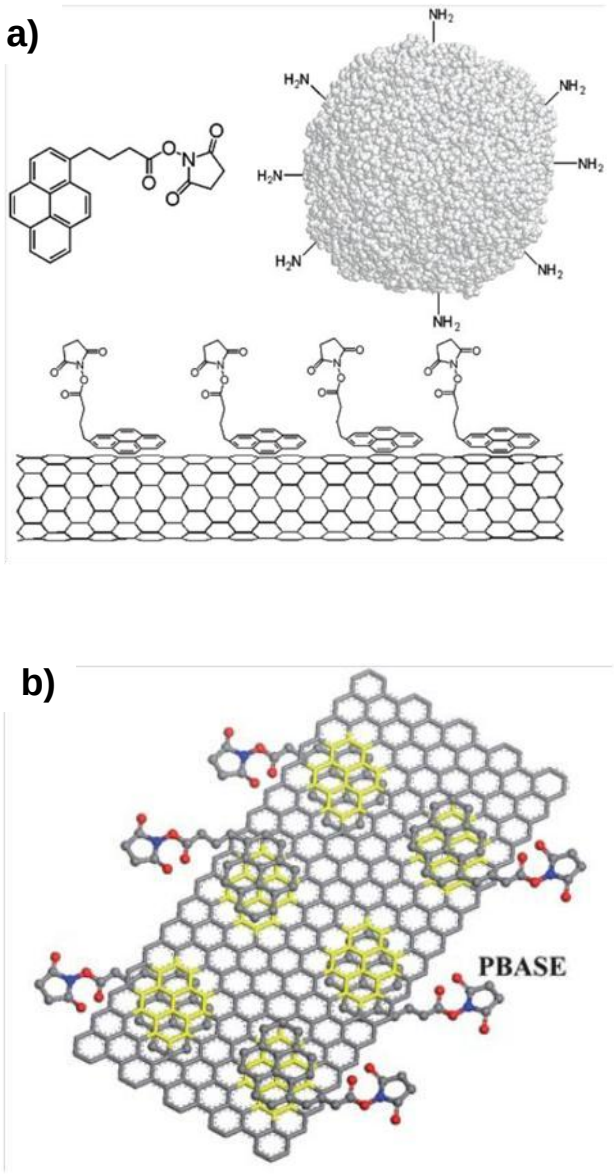

Figure 1-4. Noncovalent functionalization schemes for (a) SWNT [31] and (b) graphene [30]

1.2.3 The Applications of Carbon Nanomaterials in Biosensors

Because of their extremely small sizes and unique electronic properties, SWNTs are of great interests for the development of resistor- and field-effect-transistor-based biosensors. Dekker[33] and Avouris[34] were first to demonstrate that semiconducting SWNTs can be configured into field-effect transistor (FET) devices. SWNTs demonstrate p-type semiconducting FET characteristics and are very sensitive to changes in their environment. Proximity of charged or polarized biomolecules can cause a gating effect on isolated semiconducting or networks of SWNTs. When decorated with proper detection probes, SWNT FET can be used to detect proteins, DNA molecules or enzymes.[4b] Figure 1-5a shows the schematic illustration of a SWNT-FET biosensor. [4b]

Electrochemical biosensors based on SWNTs have also been intensively studied. SWNT can transduce and amplify the electron transfer in the biological process and thus considered an ideal material for working electrodes. SWNTs can be deposited randomly onto conductive surfaces in a mat configuration.[35] Also, SWNTs forests formed by shortened SWNTs organized vertically have also been used for sensor development.[36] Reports on successfully using SWNTs for electrochemical biosensors demonstrate detection of glucose[37], DNA hybridization[38], and specific protein binding[35].

Optical biosensors based on SWNTs are also an intensively studied topic. SWNT band gap fluorescence has been used for NIR-imaging in biological systems.[39] SWNTs can also be used as Raman tags for detection of protein interactions, DNA hybridization or antibody-antigen interactions. [40]

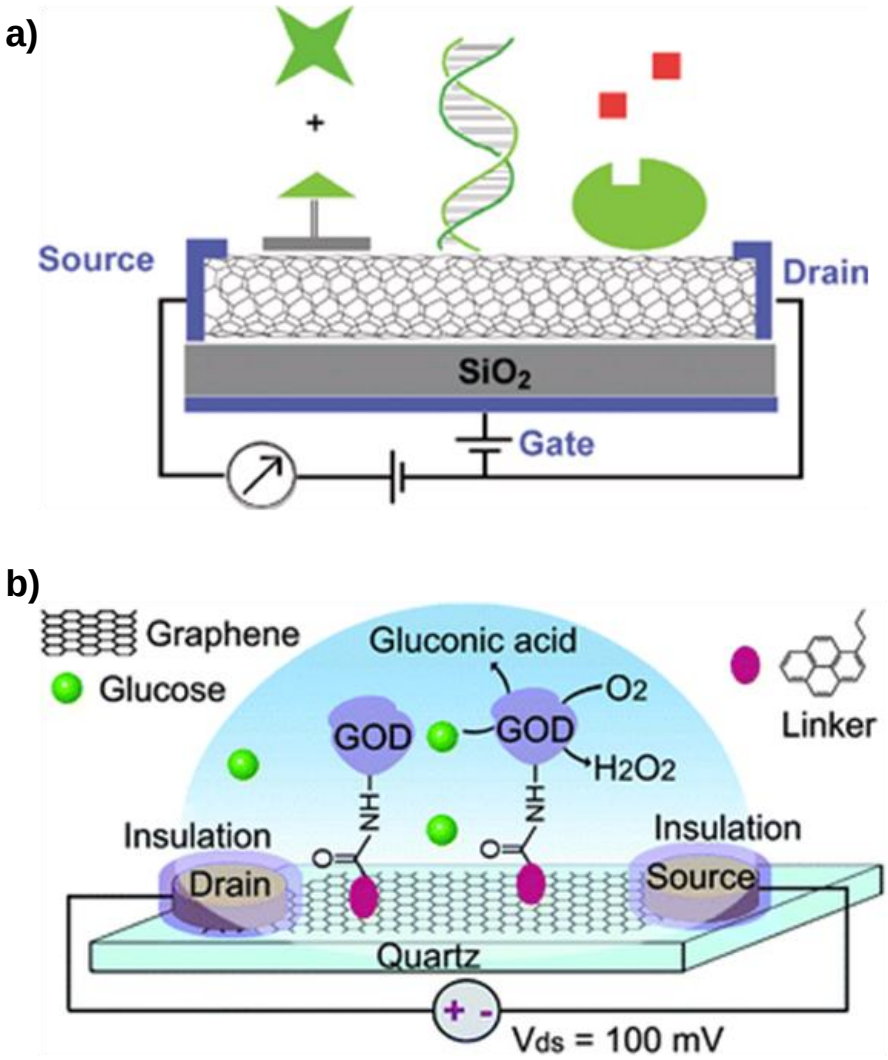

Figure 1-5. (a) Schematic representation of SWNT FET biosensors,[4b] (b) Schematic illustration of a glucose oxidase (GOD) functionalized CVD-graphene device for detection of glucose. [41]

Graphene is also being developed for biosensors in the recent years. RGO has been studied as a promising electrochemical sensor material, due to its unique electrochemical and structural properties.[23] Graphene has a large electrochemical potential window which allows the detection of molecules with high oxidation or reduction potentials. Also, electron transfer can be enhanced on RGO and the abundant chemical groups on RGO offer the convenience for functionalizations. Reported electrochemical sensors based on graphene materials include hydrogen peroxide sensor,[42] glucose sensor,[43] protein marker sensor[44] and dopamine sensor[45].

Graphene oxide can fluoresce in a wide range of wavelength and has the potential to serve as a universal fluorescence label for optical imaging.[23] GO can also quench fluorescence with superior efficiency. Based on its fluorescence and quenching abilities, GO can serve as either an energy donor or acceptor in a fluorescence resonance energy transfer (FRET) sensor. DNA sensor[46] and pathogen sensor[47] have already been developed.

Nanopores are molecular diameter pores that reside on an insulating membrane, which can be used as molecular detector with high sensitivity.[23] When a molecule passes through a nanopore that connects two separated electrolyte solutions, the ionic current flowing through the pore will be partially blocked, producing a current that is determined by the charge state and subtle molecular structure of the occupying molecule. The thinner the nanopore membrane is, the higher resolution of molecules can be achieved. Since single-layer graphene is the thinnest material known, it has been proposed that it can be used for DNA sequencing. [48]

Graphene electronic biosensors have been developed to detect biomolecules like saccharide, proteins, and DNA.[23] CVD-grown graphene sensor was fabricated to electrically detect glucose and glutamate.[41] The detection was mediated by enzymes functionalized on the graphene sheet. RGO has also been used to develop a thin-film based sensor for immunoglobulin

G (IgG) detection with an ultralow detection limit.[49] Gold nanoparticles and anti-IgG antibody conjugates were assembled onto RGO sheets by electrospray and electrostatic force directed assembly. A blocking buffer containing Tween 20, fish gelatin and BSA were used to prevent nonspecific binding to the RGO sheet. Other examples include protein sensor [50] and DNA sensor. [51]

Holey reduced graphene oxide (hRGO) (Figure 1-6, a) can be visualized as interconnected graphene nanoribbons (GNRs).[22] It has been proposed that these nanoribbons can provide quantum confinement and edge effects that will tune the graphene from semi-metal to seminconducting. Indeed, in our experiments, hRGO exhibited enhanced p-type semiconducting behavior compared to RGO (Figure 1-6, b). This enhanced semiconducting property, as well as the oxygenated groups on the edges of the holes, make hRGO promising for sensing application. Our group has explored the chemical sensing performance of hRGO. It was found that, when decorated with platinum nanoparticles, hRGO exhibited a selective response to hydrogen gas.[52]

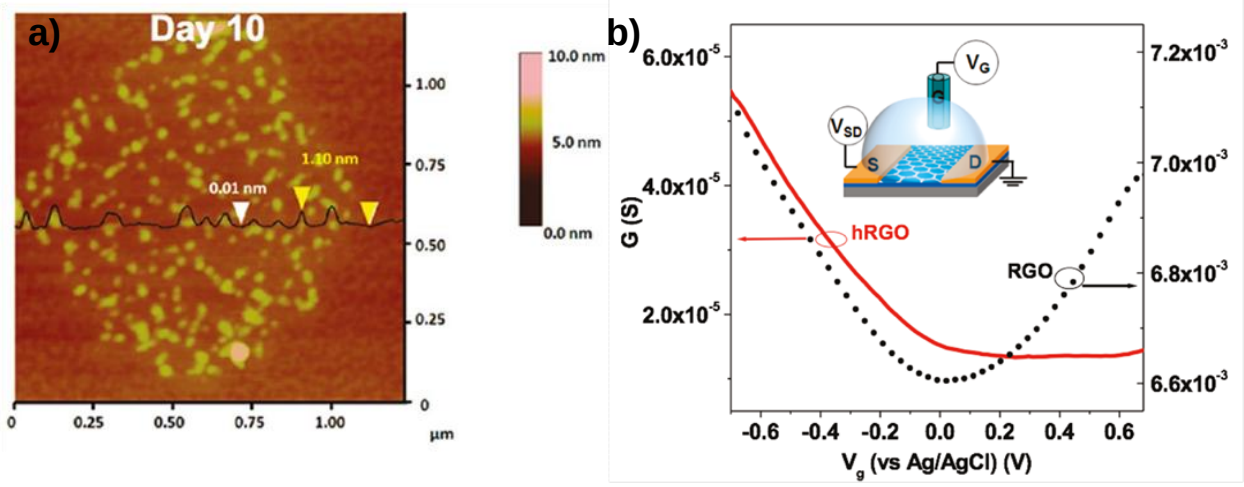

Figure 1-6. (a) AFM image of holey reduced graphene oxide (hRGO) and (b) conductivity versus potential (liquid gate) plot for RGO (black circles) and hRGO (solid red line). [22]

In this dissertation, both SWNT and graphene materials have been used for the development of biosensors. In Chapter 2, a SWNT resistor-based biosensor was developed for the detection of hydrogen peroxide. EGCG molecule from green tea was used to noncovalently functionalize SWNT network. In Chapter 3, SWNT FET was noncovalently decorated with porphyring-based glycoconjugate and its sensitivity toward lectin molecules was assessed. In Chapter 4, we compare the performances of SWNT and graphene in terms of lectin sensing, when noncovalently functionalized with porphyrin- or pyrene-based glycoconjugates. It was found that SWNTs performed better in such sensor setup. In Chapter 5, hRGO was covalently functionalized with antimicrobial peptide (AMP) for the detection of bacteria. The performance of the hRGO devices was compared with FET devices comprised of networks of oxidized SWNTs.

2.0 EXPLORING THE CHEMICAL SENSITIVITY OF A CARBON NANOTUBE/GREEN TEA COMPOSITE

2.1 CHAPTER PREFACE

The aim of this work was to investigate the chemical sensitivity of a carbon nanotube/green tea composite. We fabricated and characterized SWNT/epigallocatechin gallate (EGCG) thin films and measured their relative conductance as a function of hydrogen peroxide concentrations. The material contained in this chapter was published as an article in the journal *ACS Nano*; the figures and table in this chapter have been reproduced with permission from *ACS Nano* **2010**, *4*, 6854. Copyright 2010 American Chemical Society; the full citation is listed as Reference 53 in the bibliography section.

List of Authors: Yanan Chen, Yang Doo Lee, Harindra, Vedala, Brett L. Allen, and Alexander Star

2.2 INTRODUCTION

Single-walled carbon nanotubes (SWNTs) continue to be of increasing importance in a variety of areas including materials and life sciences.[54] Because of their size (approximately 1-3 nm in diameter, 1 μm long) and their unique physical and electronic properties, that is to say, high tensile strength, chemical stability, and electrical conductivity, SWNTs are an ideal material to interface with biological systems. For many biological applications, however, their dispersibility in aqueous media becomes the main problem. There have been a variety of methods developed to increase dispersion of this material in water by non-covalent functionalization including using surfactants,[55] polymers,[56] and biomolecules such as DNA, peptides, polysaccharides, and proteins.[57] Recently it has been shown that green tea can disperse nanotubes in aqueous solutions.[58]

Made solely from the leaves of *Camellia sinensis*, green tea has undergone extensive research for its antioxidant abilities.[59] Specifically, antioxidant properties can be derived from the presence of catechins. These organic compounds, which are a group of water-soluble polyphenols,[60] consist of epicatechin (EC), epicatechin gallate (ECG), epigallocatechin (EGC), and epigallocatechin gallate (EGCG).[61] Studies have shown that such compounds possess biological activity exhibiting not only antioxidant behavior,[62] but antitumor [63] and anticancer [63b,64] effects as well. Among antioxidants present, EGCG is the most abundant and has the strongest activity.[65] This compound reacts readily with reactive oxygen species (ROS) such as superoxide (O_2^-), hydroxyl radicals (OH), and hydrogen peroxide (H_2O_2).[66]

Here we examine the chemical sensitivity of a SWNT/EGCG composite to H_2O_2 exposure. This composite material was characterized by transmission electron microscopy (TEM), atomic force microscopy (AFM), Fourier transform infrared (FTIR) spectroscopy,

Raman spectroscopy and ultraviolet-visible-near-infrared (UV-Vis-NIR) absorption spectroscopy in thin films. Additionally, electrical conductivity of the SWNT/EGCG composite was measured on interdigitated Au electrodes upon exposure to H_2O_2 vapors, relative humidity, and varying concentrations of H_2O_2 in water. Two different device architectures, namely a SWNT/EGCG pre-mixed composite and a SWNT/EGCG layer-by-layer composite, were tested for their response to H_2O_2. The mechanism of the electrical response to H_2O_2 was further evaluated by comparing the SWNT/EGCG composite with bare SWNTs and by adding Fe_2O_3 nanoparticles (NP) into the composite in order to generate $^{\cdot}OH$ radicals by Fenton catalysis.[67] We also performed FTIR spectroscopy and studied the response of a SWNT/green tea composite in a three electrode electrolyte-gated field-effect transistor (FET) configuration to investigate the sensing mechanism.

2.3 EXPERIMENTAL

Materials. HiPco single-walled carbon nanotubes (SWNTs) were purchased from Carbon Nanotechnologies, Inc. (Grade/Lot#: P2/P0329). Epigallocatechin gallate hydrate (EGCG) was obtained from TCI America and green tea was purchased from Amore Pacific. N, N–Dimethylformamide (DMF) and hydrogen peroxide (30%) were purchased from EMD chemical and J. T. Baker, respectively. Fe_2O_3 nanoparticles were purchased as nanopowder from Sigma (544884, <50nm). All reagents were used as received without further purification.

Preparation of SWNT and green tea or EGCG composites. The fabrication of the composites was carried out by sonicating approximately 1 mg of SWNTs in 20 mL of 0.3 mg/mL green tea (or 4×10^{-4} M EGCG) at room temperature (Sonicator: Branson 5510) for 1 hr.

The solution was then centrifuged (Fisher Scientific centrific model 228) at 3400 RPM for 15 minutes. The supernatant was then filtered and washed with deionized water subsequently to remove any unbound green tea (EGCG). The resulting material was then dispersed in water to obtain SWNT/green tea (SWNT/EGCG) suspension (resulting concentration 0.05 mg/mL).

Thin films on quartz slides for spectroscopic analysis were made by spray coating a heated quartz slide (140 ℃) with the above SWNT/green tea (SWNT/EGCG) suspension. Thin film of bare SWNTs were prepared by spray coating SWNT suspension in DMF at 180 ℃.

Thin Film Characterization. Spectroscopic measurements were made using a UV-Vis-NIR spectrophotometer (Lambda 900, Perkin Elmer Instruments). FTIR was performed on a Nicolet Avatar 360 FTIR spectrometer. SWNT/EGCG composite (solid) was ground with KBr finely and the powder mixture was then crushed in a mechanical die press to form a translucent pellet through which the beam of the spectrometer can pass. SWNT/EGCG composite after exposure to H2O2 in solution was filtered and dried. A pellet of this material was made in the same way as mentioned above. FTIR of EGCG was taken by drop-casting and drying a solution of EGCG in methanol on a NaCl salt window.

Scanning electron microscopy (SEM) was performed on a Philips XL30 FEG microscope at an accelerating voltage of 10 keV to characterize the morphology of deposited thin films. Transmission electron microscopy (TEM) images were obtained with a Philips/FEI Morgagni microscope. The electron-beam accelerating voltage of the TEM was held constant at 80 keV for all imaging. All samples were suspended in water, dropcasted onto a lacey-carbon TEM grid (Pacific Grid-Tech), and allowed to dry in ambient. Atomic force microscopy (AFM) characterization was carried out on a Multimode scanning-probe microscope (Veeco). Samples were prepared by spin-coating SWNT/EGCG composite (suspended in water) onto a freshly

cleaved sheet of mica surface. After 45 min of drying in ambient conditions, the images were taken. Tapping-mode experiments using supersharp tips (AppNano ACL-SS) (2 nm) allowed for the intricate characterization of all samples. Raman measurements of the thin films were performed on a Renishaw inVia Raman microscope (excitation wavelength, 633 nm).

Metal interdigitated devices (Au/Ti, 100 nm/30 nm) with interelectrode spacing of 10 m were patterned on a Si/SiO2 substrate using conventional photolithography. One chip (2mm×2mm) containing four identical devices was then set into a 40-pin ceramic dual in-line package (CERDIP) and wire-bonded using Au wire. Devices were subsequently isolated from the rest of the package by epoxying the inner cavity. Fabrication of bare SWNTs conductance measurement was made by sonicating approximately 1 mg of SWNTs in 20 mL DMF and drop-casting 40 μL of the dispersion directly on the Si chip in the package device mentioned above. The fabrication of SWNT/EGCG composite devices was carried out by drop-casting 40 μL SWNT/EGCG suspension on a chip and allowing to dry in ambient. For the layer-by-layer SWNT/EGCG device architecture, SWNTs were first deposited onto the electrodes by dielectrophoresis (DEP) method using SWNTs suspension in DMF (Agilent 33250A 80 MHz Function/Arbitrary Waveform Generator, 10 MHz, 8.00 Vpp). After washing with DMF and drying at 180 ℃, the devices were incubated with 4.4×10^{-4} M EGCG solution. For SWNTs/EGCG/Fe_2O_3 nanoparticle devices, a SWNT/EGCG device was first prepared and Fe_2O_3 nanoparticle suspension in water was then drop-casted on the electrodes and allowed to dry.

Conductance measurements on composite devices were carried out on a custom test-board using Zephyr software.31 Using a Keithley 2602 dual-source meter and Keithley 708A switching mainframe, we were able to monitor all devices on a single chip at a given time.

Device switching was performed at 500 milliseconds, displaying near-real time responses for each device.

To investigate the sensing mechanism of H_2O_2 and show application of green tea in chemical sensing, we studied the response of SWNT/green tea composite in a three electrode electrolyte-gated field-effect transistor (FET) configuration. In this setup, a home built fluid chamber was mounted on the CERDIP package to hold small volume (100 μL) of electrolyte. The conductance of SWNT transistor device was tuned using double distilled water as electrolyte. A Ag/AgCl reference electrode connected to a voltage source (Keithley 4200) was used a gate electrode. A liquid gate potential was applied to the reference electrode with respect to grounded drain electrode, while maintaining a constant bias voltage (10 mV) between the source and drain voltage. To obtain a negligible leakage current (10 nA), the gate potential was scanned from -750 mV to 750 mV.

2.4 RESULTS AND DISCUSSION

Using green tea and EGCG (Figure 2-1a), SWNTs were dispersed in water through sonication. Figure 2-1, b shows these suspensions in water which were stable for up to three months. As the catechin is comprised of phenol groups, it is thought that dispersion occurs through π-π stacking with the nanotube's graphitic lattice. Presumably, the noncovalent interaction between SWNTs and cathechin leads to the disaggregation of SWNT bundles and provides a stable dispersion by sonication.[58]

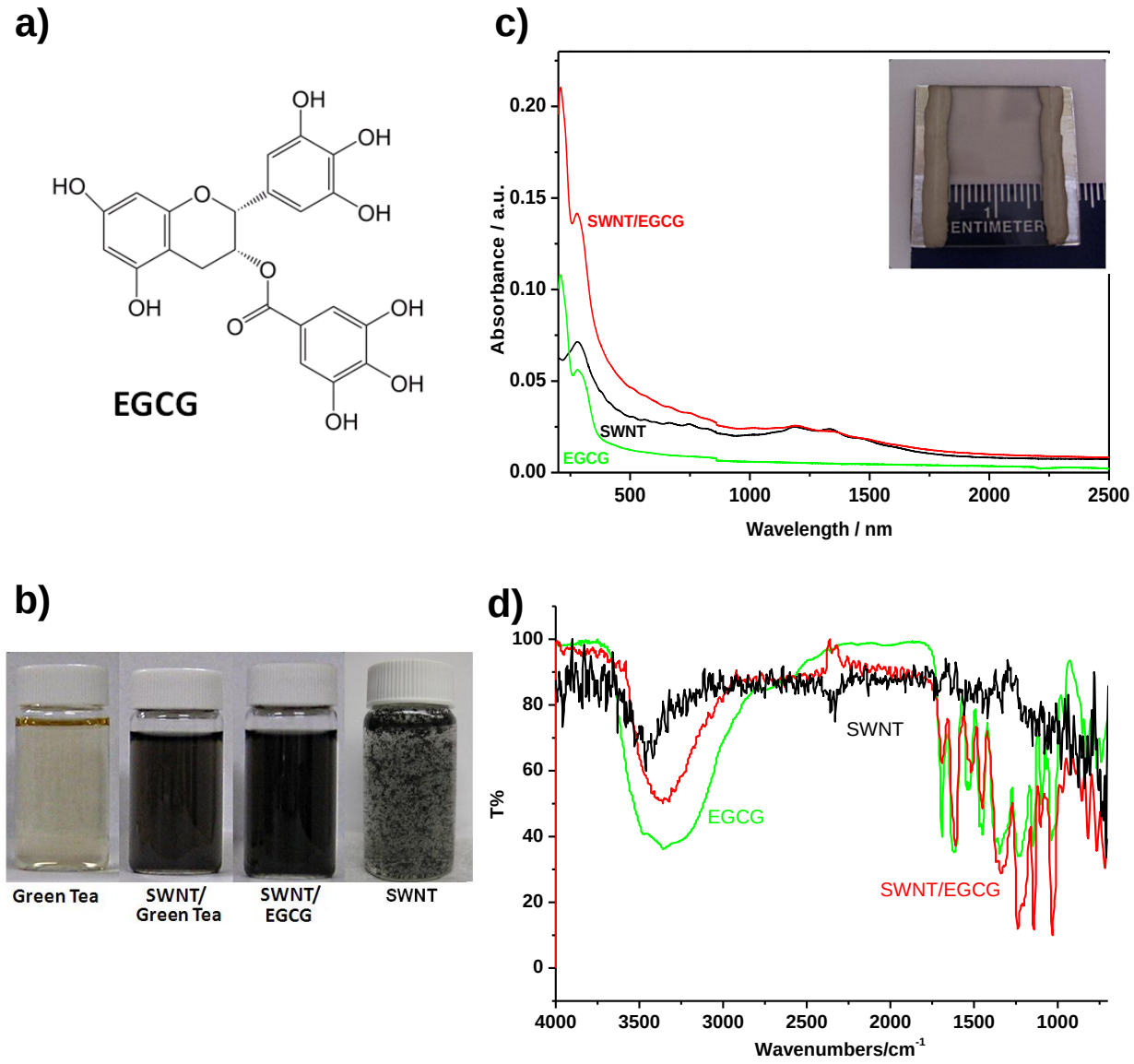

Figure 2-1. (a) Chemical structure of epigallocatechin gallate (EGCG). (b) Photograph of four vials with green tea (left), SWNT and green tea (middle left), 4.4 × 10^{-4} M EGCG sonicated with ca. 1 mg of SWNTs (middle right) and SWNTs in water (right). (c) UV-Vis-NIR absorption spectra of SWNT (black), EGCG (green), and SWNT/EGCG (red) as thin films on quartz. Inset displays a photograph of transparent SWNT/EGCG conductive film on a quartz slide. (d) FTIR spectrum of bare SWNTs (black), EGCG in MeOH (4×10^{-4} M) (green) and SWNT/EGCG composite after heating at 140 ℃ for 20 min (red).

To study the interaction between EGCG and carbon nanotubes, spectroscopic measurements were taken of a spray-cast film on a quartz slide using UV-Vis-NIR spectroscopy. The resulting spectrum is a superposition of SWNTs and EGCG spectra (Figure 2-1, c), in a good agreement with previous solution studies.[58] It should be mentioned here that the thin films of SWNT/EGCG composite for UV-Vis-NIR studies were prepared by spray-casting the solution to a quartz slide at 140 ℃ to prevent nanotube agglomeration through drying and provide uniform films. EGCG was stable to this thermal treatment because, after the heating, the EGCG absorption spectrum in the composite demonstrates no shift compared to pure EGCG (prepared by drop-casting EGCG solution and drying at room temperature) (Figure 2-1, c). Furthermore, an FTIR spectrum of SWNT/EGCG composite (heated at 140 ℃ for 20 min) showed peaks (eg. 3360 cm^{-1}, 1610 cm^{-1}, 1450 cm^{-1} and 1140 cm^{-1}) characteristic of EGCG (in MeOH) , yet additional evidence of the composite thermal stability (Figure 2-1, d). In fact, the SWNT/EGCG composite shows no degradation up to 200 ℃, according to thermogravimetric analysis (TGA) (Figure-S 2-1). Combined with TGA results, the spectroscopic results confirm that this composite is stable at the temperature we adopted to prepare the thin films. Interactions between SWNTs and EGCG in the composite were further characterized by Raman spectroscopy, AFM and TEM. The Raman spectra of a SWNT/EGCG composite and pristine SWNT were mostly similar (Figure-S 2-2), indicating noncovalent interaction between EGCG and SWNT with a negligible effect on SWNT vibration modes.[68] To confirm EGCG coverage and provide information about composite surface morphology, we characterized the composite using AFM and TEM. In AFM images, the surface of the SWNT/EGCG composite appears to be covered unevenly (Figure-S 2-3, a), clearly showing different morphology from pristine SWNTs (Figure-S 2-3, b). Similar change in morphology was observed in TEM imaging. SWNTs in the

composite are covered with an amorphous coating (Figure-S 2-4). Because of the difficulty in dispersing pristine SWNTs in water (Figure 2-1, b), for AFM and TEM, we used SWNTs suspension in DMF to provide information of uncovered, bare SWNTs.

The thin films of SWNT/EGCG composite were both transparent and conductive (Figure 2-1, c, inset). The electrical conductance of the films (10 films) was measured as 271 ± 61 μS. These values are comparable to 325 ± 105 μS conductance of thin films made from bare SWNTs (13 films) prepared by spray-coating a SWNT suspension in DMF at 180 ℃. Taken into account the thin film thickness measured by AFM (Figure-S 2-5), the conductivities can be calculated as 22.9 ± 5.1 S/cm and 27.4 ± 8.9 S/cm, for SWNT/EGCG and SWNT thin films, respectively (see Supporting Info for calculation details). The small decrease in the thin film conductivities could be due to the conformal coating of EGCG on the individual SWNTs thereby causing an increase in inter-nanotube separation.

In order to examine the chemical sensitivity of the composite to varying concentrations of H_2O_2, SWNT/EGCG composite devices were fabricated by drop-casting SWNT/EGCG on Si chips with four interdigitated Au electrodes (Figure 2-2, a and b). Conductance measurements on composite devices were carried out on a custom test-board using Zephyr software.[69] Using a Keithley 2602 dual-source meter and Keithley 708A switching mainframe, we monitored all devices on a single chip at a given time.

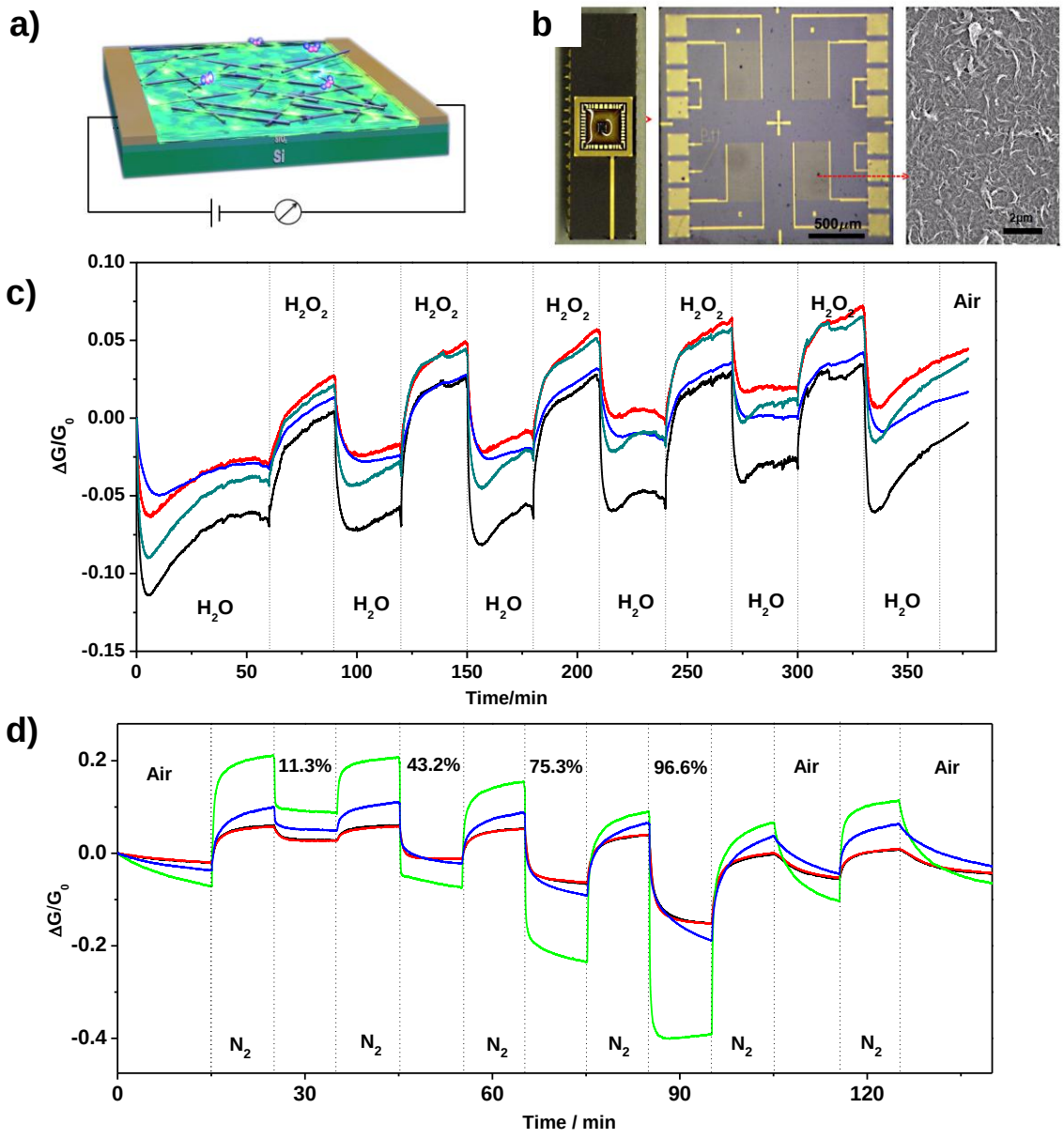

Figure 2-2. (a) Schematic illustration of SWNT/EGCG composite device. (b) Optical images and scanning electron microscope (SEM) image of the SWNT/EGCG film deposited on CERDIP package with Si chip containing four interdigitated Au electrodes. (c) Relative conductance versus time dependence of four interdigitated devices (shown in different colors) coated with SWNT/EGCG composite cycled between H_2O_2 and H_2O vapor pulses (H_2O_2 concentration was calculated as 45 ppm). (d) Relative conductance versus time dependence of four interdigitated devices coated with SWNT/EGCG composite cycled between dry N_2 and N_2 bubbled through different saturated salt solutions generating different levels of relative humidity (%).

We first investigated the effect of H_2O_2 vapors by measuring relative conductance ($\Delta G/G_0$) versus time as H_2O_2 vapors were pulsed using N_2 as a carrier gas. Devices were tested under a constant applied voltage of 50 mV at room temperature. H_2O_2 vapors were pulsed at 30 minute intervals, with saturated water vapor acting as the "off" state. Water and H_2O_2 vapors were generated by passing 660 sccm (standard cubic centimeters per minute) of N_2 gas through bubblers filled with deionized water and 1 M H_2O_2 solution, respectively. As shown in Figure 2-2c, device exposure to H_2O_2 vapors resulted in a conductance increase and the device response was constant during the test. Bare SWNTs devices, however, showed no obvious response to H_2O_2 vapors, and no stable baseline was achieved under device exposure to high relative humidity (Figure-S 2-6, a). By using saturated water vapor as the "off" state, we attempted to isolate the composite response to H_2O_2 vapors from any effects of relative humidity. However, the effect was not fully eliminated. The H_2O_2 concentration in the vapor was calculated[70] to be 45 ppm and its effect on the composite conductance was largely masked by the change in relative humidity. The measured relative humidities of H_2O vapor and H_2O_2 vapor were 92% and 80%, respectively.

In fact, SWNT/EGCG composite devices have a large response to water vapors. Figure 2d shows the normalized response of the composite device to the effects of relative humidity by pulsing varying relative humidity using N_2 as a carrier gas. Briefly, controlled relative humidity was created by passing N_2 gas through different saturated salt solutions including LiCl, K_2CO_3, NaCl, and KH_2PO_4 corresponding to relative humidities of 11.3%, 43.2%, 75.3%, and 96.6%, respectively.[71] Relative humidities were pulsed at 10 minute intervals, with dry N_2 acting as the "off" state. As relative humidity increases, conductance of SWNT/EGCG devices decreases. It

is also quite notable that this response is one order of magnitude larger for the SWNT/EGCG composite over that of bare nanotubes (Figure-S 2-6, b and c).

Such a decrease in conductance for the SWNT/EGCG composite is typical of most SWNT/polymer composites.[72] EGCG, hydrophilic in nature, has a high affinity for water. As this layer gets hydrated two effects may occur. The first effect involves the expansion of the EGCG composite, at high relative humidity, as we confirmed by volume change of the composite. The composite expands twice when relative humidity is increased from 0% to 100% (Figure-S 2-7). As swelling of this composite occurs, nanotubes are separated further apart and the percolation through the SWNT network is decreased resulting in a decrease in conductance. Additionally, water molecules can create charge traps on nanotube networks,[73] resulting in the change in the conductance.

To overcome effects of relative humidity, we performed liquid measurements. The stability of the SWNT/EGCG thin films in aqueous environment was tested by measuring the thickness of the thin films before and after their exposure to water for 4 hours and monitoring the conductance of the thin film immersed in water. The small variation in the thin film thickness (Figure-S 2-5a and b) and the stable conductance over the test time (Figure-S 2-5c and d) indicated insignificant leaching and confirmed the film stability. We have already made mention that EGCG is a strong antioxidant and, as such, should have a specific response for ROS such as H_2O_2, as opposed to response of the thin films to water. In liquid measurements, the composite should be fully hydrated, and thus, the conductance change will be only due to the result of ROS in the solution.

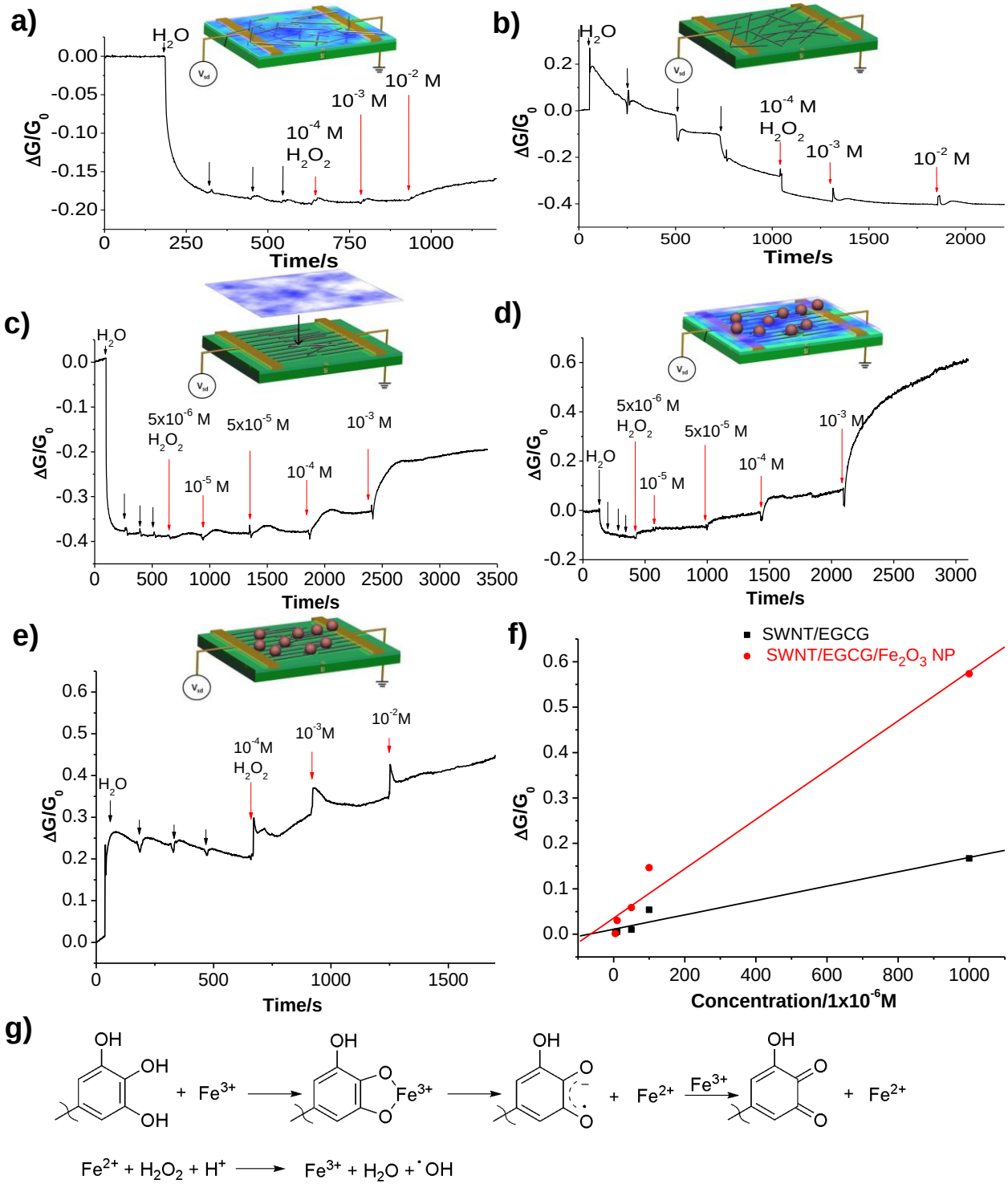
a)
H2O
10-2 M
10-3 M
10-4 M
H2O2
ΔG/G0
Time/s
b)
H2O
10-4 M
H2O2
10-3 M
10-2 M
ΔG/G0
Time/s
c)
H2O
5x10-6 M
H2O2
5x10-5 M
10-3 M
10-5 M
10-4 M
ΔG/G0
Time/s
d)
5x10-6 M
H2O2
5x10-5 M
10-3 M
H2O
10-5 M
10-4 M
ΔG/G0
Time/s
e)
10-2M
10-3M
10-4M
H2O2
H2O
ΔG/G0
Time/s
f)
SWNT/EGCG
SWNT/EGCG/Fe2O3 NP
ΔG/G0
Concentration/1x10-6M
g)
OH
OH
OH
+ Fe3+
Fe3+
O
O
+ Fe2+
Fe3+
+ Fe2+
Fe2+ + H2O2 + H+
Fe3+ + H2O + ·OH

Figure 2-3. Relative conductance versus time response to varying concentrations of H_2O_2 of (a) SWNT/EGCG pre-mixed composite, (b) of bare SWNT device, (c) of SWNT/EGCG layer-by-layer composite, (d) SWNT/EGCG/(Fe_2O_3 nanoparticles) layer-by-layer composite and (e) SWNT/(Fe_2O_3 nanoparticles) layer-by-layer composite. Insets show the schematic device architectures. (f) Relative conductance change vs. concentration plot of SWNT/EGCG (black) and SWNT/EGCG/(Fe_2O_3 nanoparticles) (red). (g) Fenton's catalysis mechanism includes the coordination of Fe^{3+} by polyphenols in EGCG, subsequent iron reduction and semiquinone formation, and reduction of Fe^{3+} to form a quinone species and Fe^{2+} (reaction 1). H_2O_2 is reduced by Fe^{2+}, resulting in the formation of •OH radical (reaction 2). (Ref [74])

We examined SWNT/EGCG composite devices for changes in conductance in real time. Devices were initially exposed to four additions of 10 μL deionized water to create a stable hydrated layer within SWNT/EGCG composites. As can be seen from Figure 2-3a, the initial exposure to 10 μL of water elicited the same conductance decrease as witnessed in the relative humidity experiments. After four additions of deionized water, any subsequent response should be solely due to the concentrations of H_2O_2. An addition of 10^{-4} M H_2O_2 (10 μL) resulted in a slight increase in the conductance of the device. Then the higher concentrations of H_2O_2 (10^{-3} M and 10^{-2} M) were added subsequently and the responses increased accordingly. As a control experiment, bare nanotube device were tested for the same concentrations of H_2O_2, as well as the initial additions of deionized water. As can be seen from Figure 2-3b, after additions of deionized water, the bare SWNT device cannot reach a stable baseline as effectively as the SWNT/EGCG composite, which may be due to the hydrophobicity of bare nanotubes, and the device has no obvious response to the subsequent additions of H_2O_2.

The response of the SWNT/EGCG composite to H_2O_2, however, is relatively smaller than the response to water. To explore a method to improve the H_2O_2 response, we adopted layer-by-layer architecture to fabricate the SWNT/EGCG device (Figure 2-3c inset). We first deposited

SWNTs (DMF suspension) onto the electrodes using a dielectrophoresis (DEP) method.[75] After washing with DMF and drying at 180 ℃, the chips were incubated with EGCG solution (in water, 4.4×10^{-4} M) for two hours to deposit EGCG on the surface of SWNTs and then washed with deionized water and dried in ambient. This device architecture demonstrated improved response to H_2O_2 (Figure 2-3c). H_2O_2 concentration as low as 5×10^{-6} M was detected with signal to noise ratio of 8. The improvement in the sensor performance can be attributed to two factors namely: dielectrophoretic assembly of nanotube between the metal electrodes and layer-by-layer deposition of EGCG on bare SWNTs. DEP aids in alignment of the nanotubes between the electrodes and results in increased field-effect mobility as compared to devices fabricated by drop casting.[76] Layer-by-layer deposition of EGCG results in direct contact of nanotubes with metal electrodes, thereby reducing the contact resistance.

The proposed mechanism for the conductance response to H_2O_2 is derived from the antioxidant properties of EGCG, which has been the subject of much debate.[77] Catechins are oxidized by radicals and thus lose electrons, which segues into the response for SWNT/EGCG devices. Presumably interactions between EGCG and SWNTs are such that some electron density is transferred between the species. As EGCG is oxidized and loses electrons, it may be that this causes subsequent withdrawal of electron density from the nanotube network resulting in an increase in the majority charge carrier, holes, and increasing conductance.

To further investigate the mechanism of the conductance response of SWNT/EGCG composite to H_2O_2, we designed another experiment in which a Fe_2O_3 nanoparticle solution was drop-casted on the electrodes modified with SWNTs and EGCG using layer-by-layer setup (Figure 2-3d and e). While SWNT/(Fe_2O_3 NP)system showed insignificant improvement for H_2O_2 detection over bare SWNTs, a combination of EGCG and Fe_2O_3 nanoparticles has positive

synergy for H_2O_2 detection with SWNTs. As can be seen from calibration plot for SWNT/EGCG and SWNT/EGCG/(Fe_2O_3 NP) devices (Figure 2-3f), the H_2O_2 responses can be increased to more than 100%, due to the presence of Fe_2O_3 nanoparticles. A similar effect was observed when the SWNT/EGCG composite was mixed with Fe_2O_3 nanoparticles and drop-casted on the device chip. Compared to Figure 2-3a, a significant increase in H_2O_2 signal was observed (Figure-S 2-8). The observed increase in H_2O_2 signal can be explained by the additional OH generation *via* Fenton's catalysis mechanism shown in Figure 2-3g. The Fe^{3+} ions from the Fe_2O_3 nanoparticles first coordinate with EGCG phenol group, followed by subsequent semiquinone formation, and reduction of Fe^{3+} to form quinone species and Fe^{2+}.[74,78] The Fe^{2+} ions formed in this process will then react with H_2O_2 to form reactive oxygen species OH, which in turn will oxidize EGCG. The higher degree of EGCG oxidation leads to the observed increased relative conductance response of SWNT/EGCG composite. This further suggests that the relative conductance response of SWNT/EGCG composites to H_2O_2 arises from the antioxidant property of EGCG and the electron transfer between SWNTs and EGCG.

To confirm that EGCG is actually oxidized upon H_2O_2 exposure, we analyzed FTIR spectra of the composite before and after exposure to 10^{-2} M H_2O_2. Figure 2-4a shows the possible oxidation products of EGCG with H_2O_2.[77a,79] As can be seen in Figure 2-4b, the peak changes (from 1601 cm^{-1} to 1714 cm^{-1} and from 3360 cm^{-1} to 3440 cm^{-1}) indicate the formations of quinone groups and carboxyl group, characteristic of EGCG oxidation products (**1** and **2**). We hypothesize that EGCG oxidation and the subsequent electron transfer lead to the SWNT/EGCG composite response to H_2O_2.

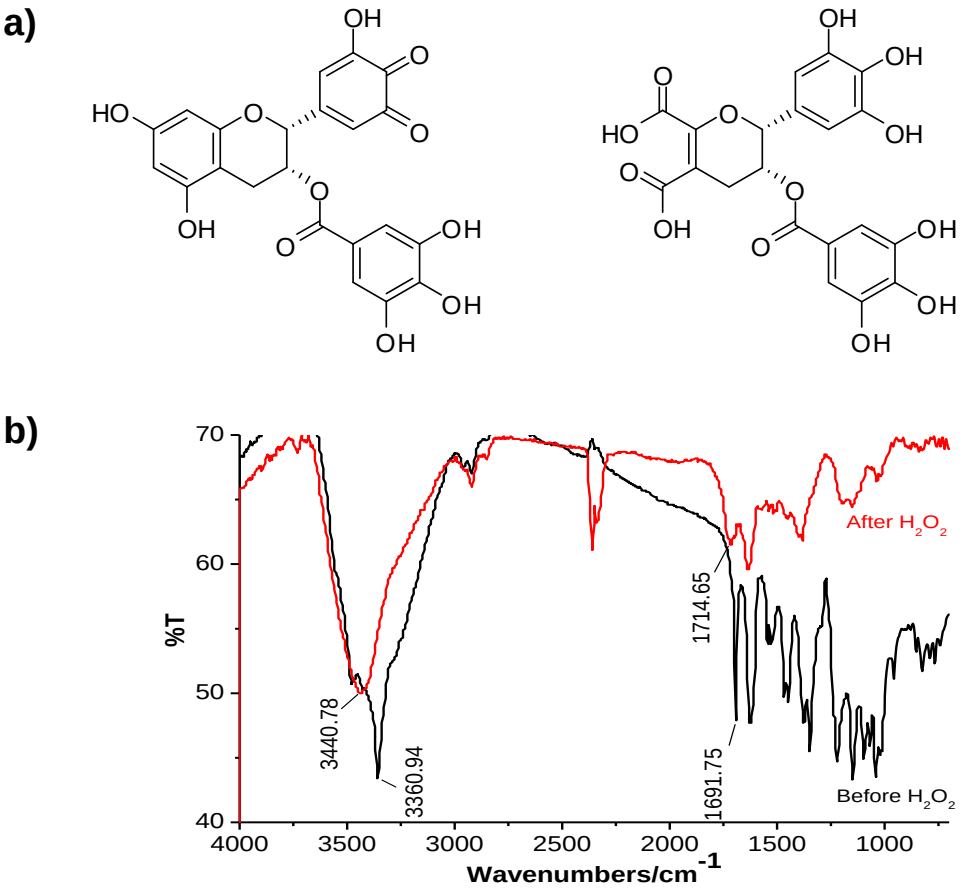

Figure 2-4. (a) Chemical structures of possible oxidation products of EGCG with H_2O_2 (Ref [79] and [77b]). (b) FTIR spectrum of SWNT/EGCG composite before (black) and after exposure to 10^{-2} M H_2O_2 (Red).

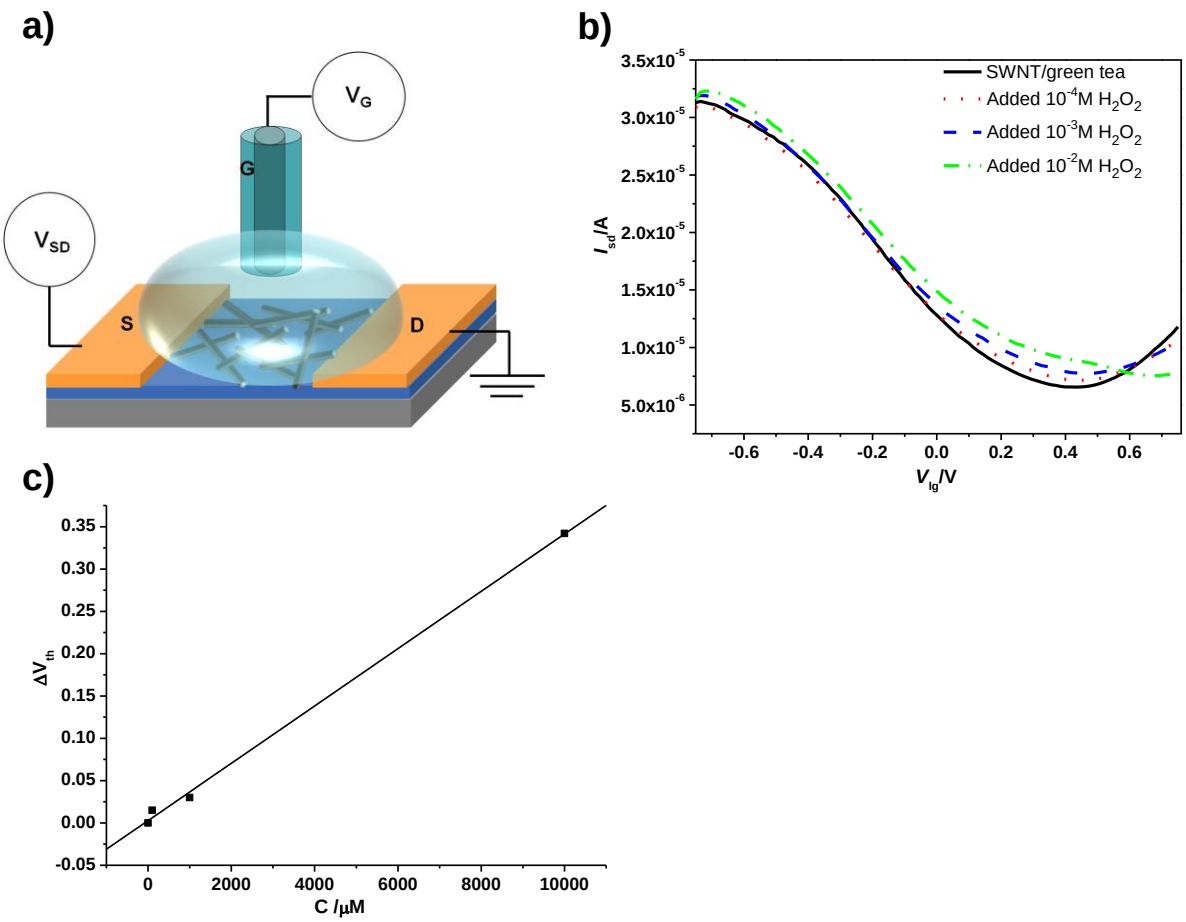

Figure 2-5. (a) Schematic illustration of the liquid-gate FET testing device setup. (b) Current versus liquid gate potential curves of SWNT/green tea composite device acquired before (black solid) and after adding 10^{-4} M (red dot), 10^{-3} M (blue dash) and 10^{-2} M (green dot dash) H_2O_2. (c) Threshold voltage shift versus H_2O_2 concentration plot.

To further understand the sensing mechanism and show application of green tea in chemical sensing, we studied the effect of H_2O_2 concentrations on SWNT/green tea composite conductance in a liquid gate FET configuration. It has been demonstrated in earlier reports that an electrolyte-gated FET configuration can be effectively used for understanding the interaction of various molecules (charged ions or biomolecules) with SWNTs.[80] Figure 2-5a shows a schematic illustration of the FET device. Figure 2-5b shows the I_d *vs* V_{lg} for SWNT/green tea composite device measured at different concentrations of H_2O_2. A gradual shift in the threshold voltage for each curve was observed with the increasing concentrations of H_2O_2 from 10^{-4} M to 10^{-2} M (Figure 2-5c). This shift towards positive gate voltages indicates a p-doping of the FET device which can be attributed to the negative charge donated into the channel from the H_2O_2 molecule. These results strongly correlate with the SWNT/EGCG data shown in Figure 2-3a which shows the increase in relative conductance with increasing concentrations of H_2O_2.

2.5 CONCLUSIONS

In conclusion, we studied SWNT/green tea and SWNT/EGCG composites using various characterization methods and most importantly, present here the chemical sensitivity of the composites to ROS. Because of EGCG's antioxidant properties and hydrophilic nature, this composite exhibits sensitivity to hydrogen peroxide in aqueous solution. We propose that these responses are the result of the oxidation of EGCG and electron transfer between EGCG and SWNTs. The H_2O_2 response was further improved by changes in the device architecture and the use of Fe_2O_3 nanoparticles, which promote ROS formation through Fenton's catalysis. Such

solid-state electrical measurements indicate that SWNTs functionalized with common-or-garden green tea have great potential for electronic detection of ROS.

2.6 ACKNOWLEDGEMENT

The project described was supported by NIEHS R01ES019304. Y. D. L. acknowledges support of the Korea Research Foundation Grant (KRF-2007-357-D00051) funded by the Korean Government (MOEHRD). We thank the Department of Materials Science and Engineering at the University of Pittsburgh for access to the SEM and TEM instrumentation.

2.7 SUPPORTING INFORMATION

Thermogravimetric analysis (TGA), Raman spectroscopy, atomic force microscopy (AFM) and transmission electron microscopy (TEM) characterizations of the composite, AFM images of SWNT/EGCG thin film thickness before and after water exposure, conductance of SWNT/EGCG thin film immersed in water, responses of bare SWNTs to H_2O_2 vapors and relative humidity (RH), optical images of SWNT/EGCG composite before and after exposing to high humidity, relative conductance versus time response to H_2O_2 of SWNT/EGCG/(Fe_2O_3 nanoparticle) composite, and calculation of the SWNT/EGCG and bare SWNT thin films conductivities available.

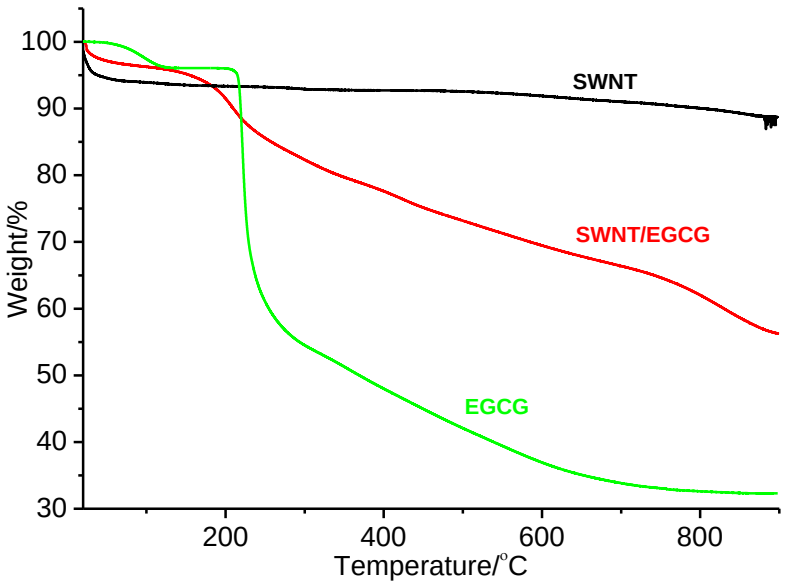

Figure-S 2-1. TGA of SWNT (black), EGCG (green) and SWNT/EGCG composite (red).

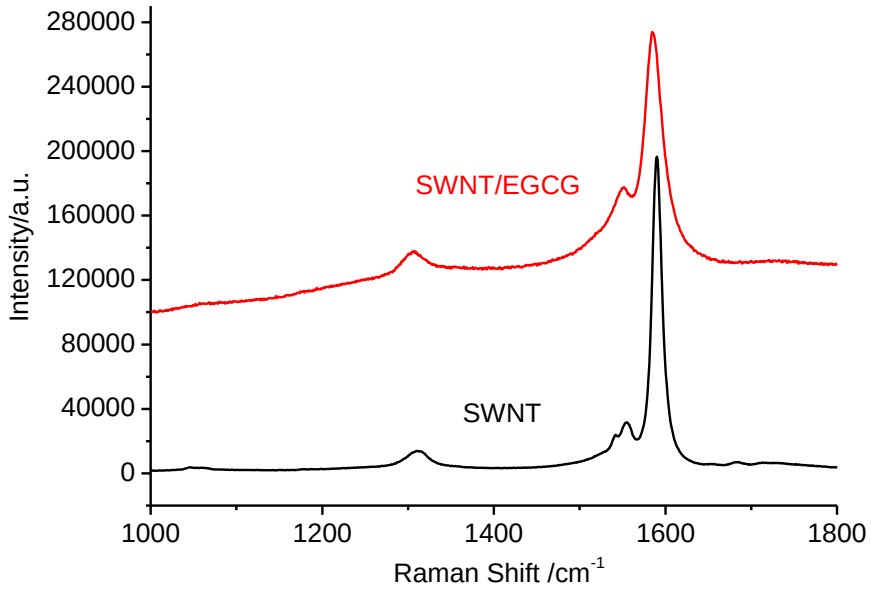

Figure-S 2-2. Raman spectra of pristine SWNTs (black) and SWNT/EGCG composite (red).

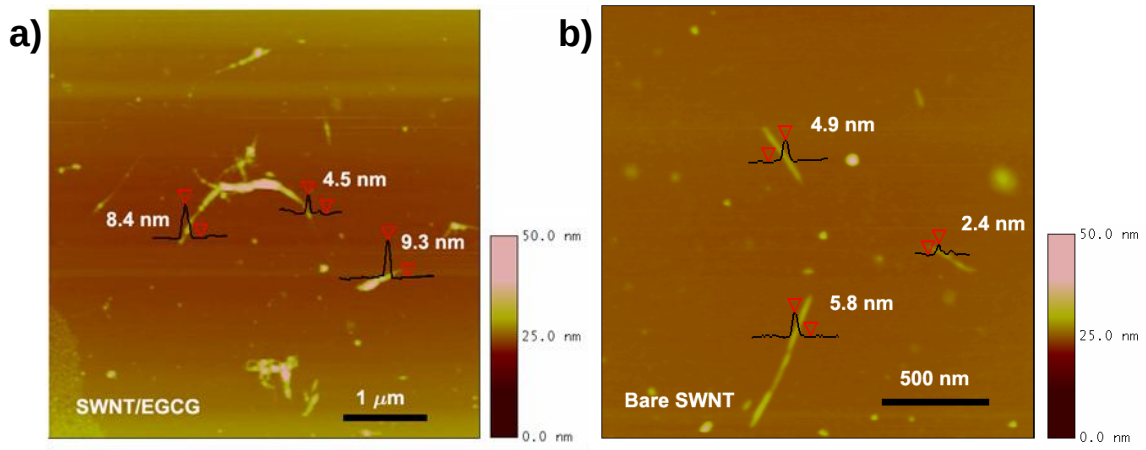

Figure-S 2-3. (a) AFM image of SWNTs treated with 4.4 × 10^{-4} M EGCG. Section analysis reveals that SWNTs appear 4–9 nm in diameter after modification with EGCG. (b) AFM image of bare SWNTs. Section analysis reveals that bare SWNTs exist as small bundles with diameter around 2 – 6 nm.

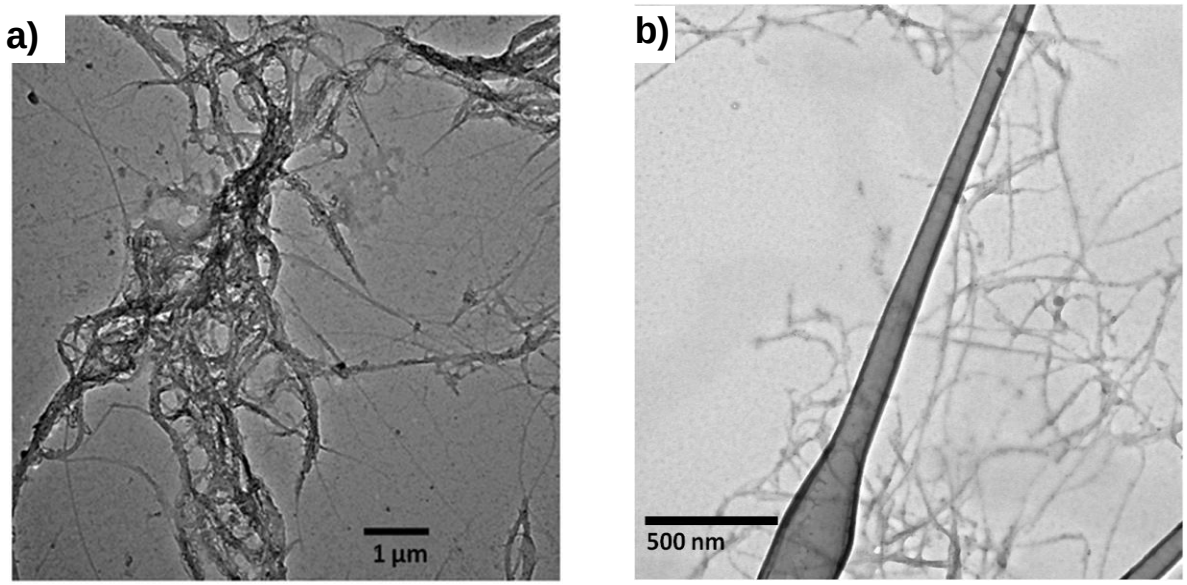

Figure-S 2-4. Transmission electron microscopy (TEM) images of SWNTs treated with (a) 4.4 × 10^{-4}M EGCG in water and (b) bare SWNTs in DMF solution (bare SWNTs cannot be dispersed in pure water).

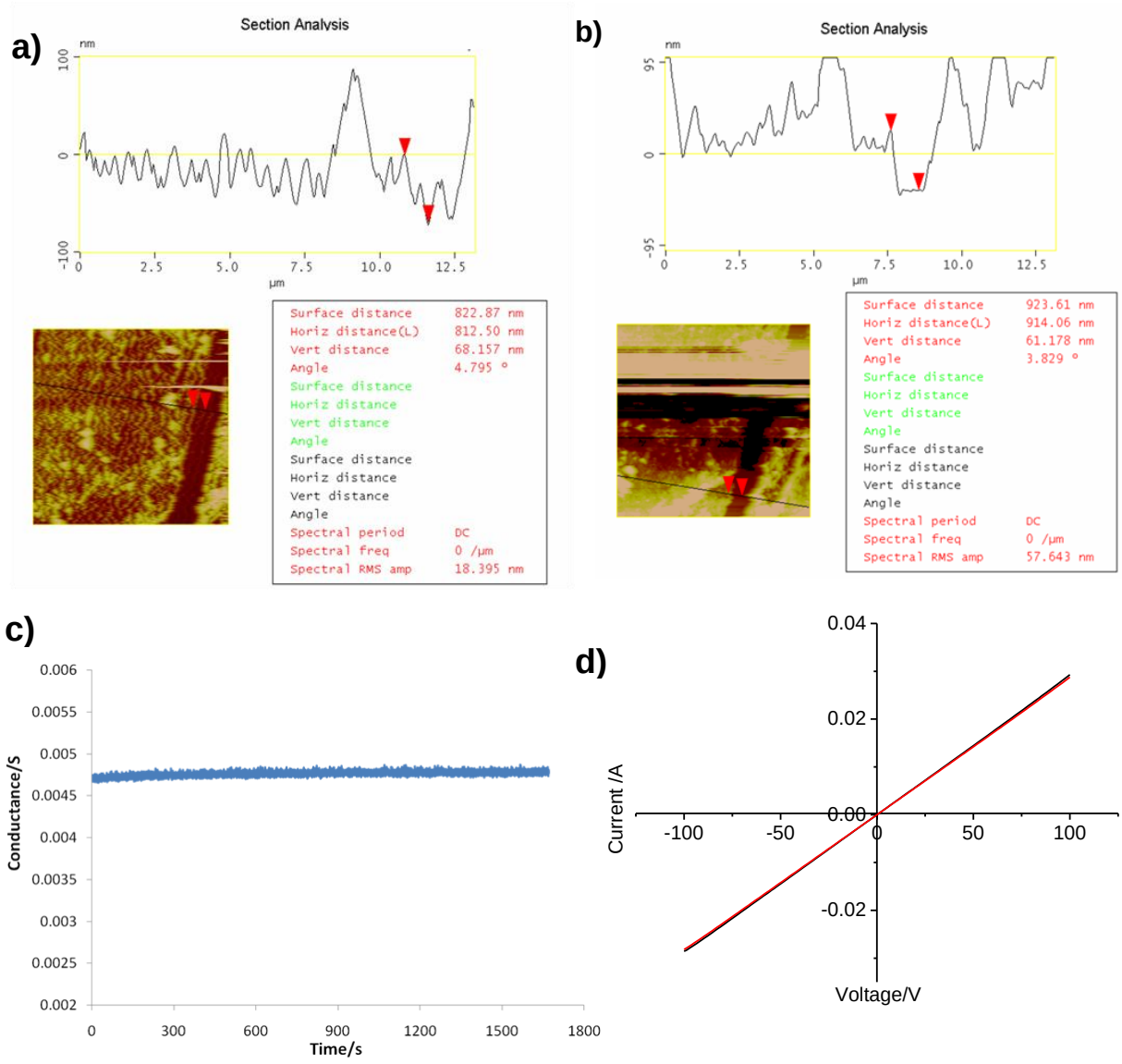

Figure-S 2-5. Atomic Force Microscopy (AFM) images of the SWNT/EGCG composite thin film (a) before and (b) after incubation in water for 4 hours. AFM section analysis demonstrates 10% decrease in the film thicknesses from 68 nm to 61 nm after incubation in water, indicating insignificant leaching over the tested time period. (c) Electrical conductance of SWNT/EGCG composite device versus time after addition of water. The device demonstrates a stable baseline while it is immersed in water. (d) Current vs. voltage measurement of bare SWNTs thin film before addition of water (black) and after the added water is dried (red), showing no change in the film conductance.

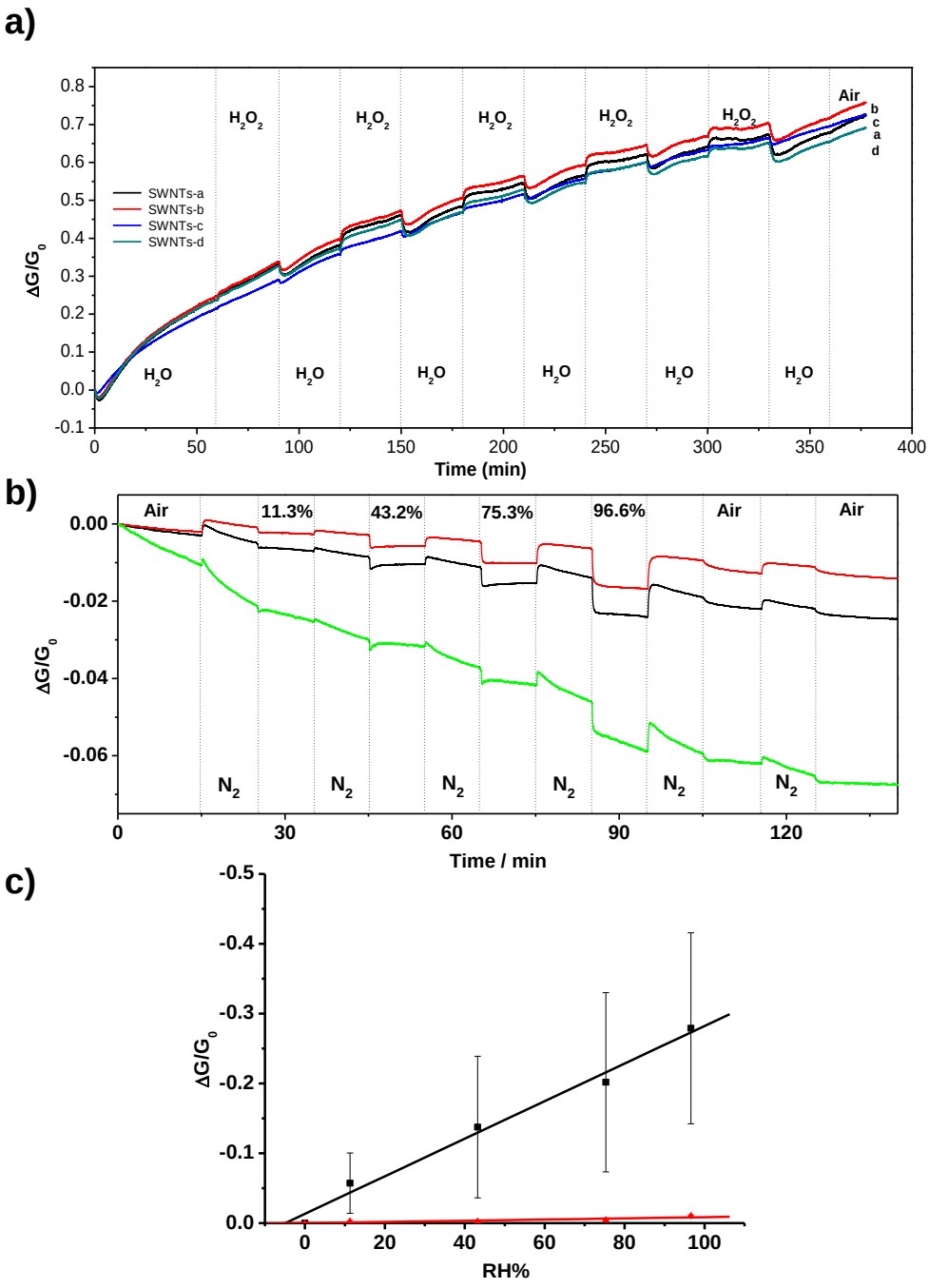

Figure-S 2-6. (a) Relative conductance response versus time dependence of four interdigitated devices coated with bare SWNTs exposed to H_2O_2 vapor pulses. (b) Relative conductance response versus time dependence of three interdigitated devices coated with bare SWNTs and exposed to varying relative humidity pulses. (c) Relative humidity (RH) calibration plot of SWNT/EGCG composite material (black) and bare SWNTs (red).

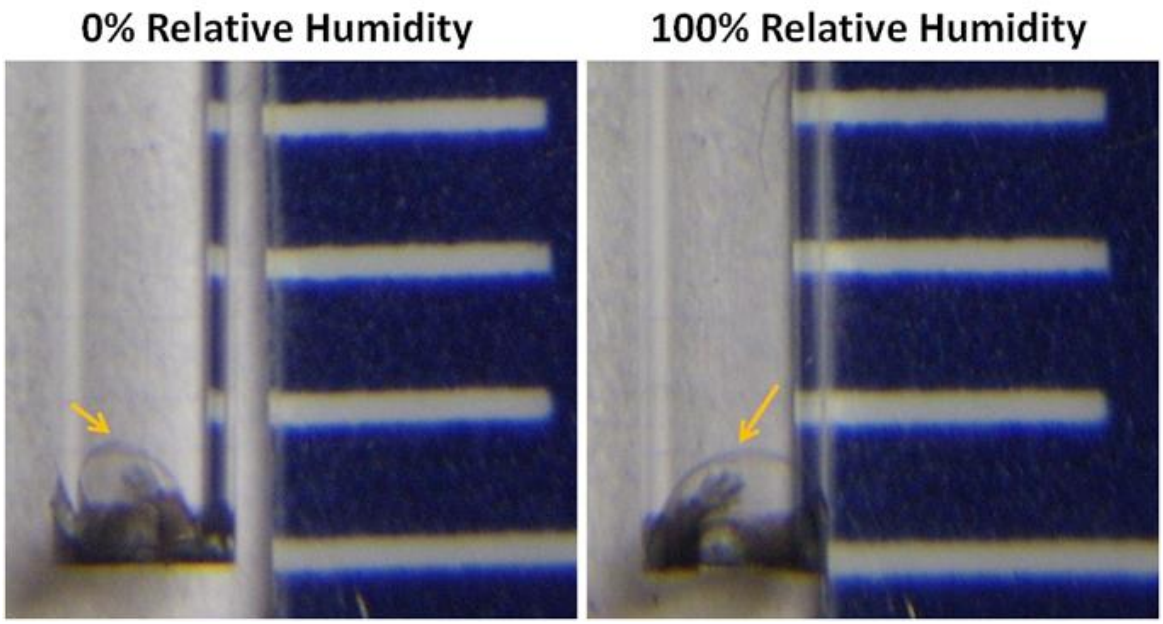

Figure-S 2-7. Optical image depicting the swelling of a SWNT/EGCG composite because of increasing relative humidity (scale in millimetres).

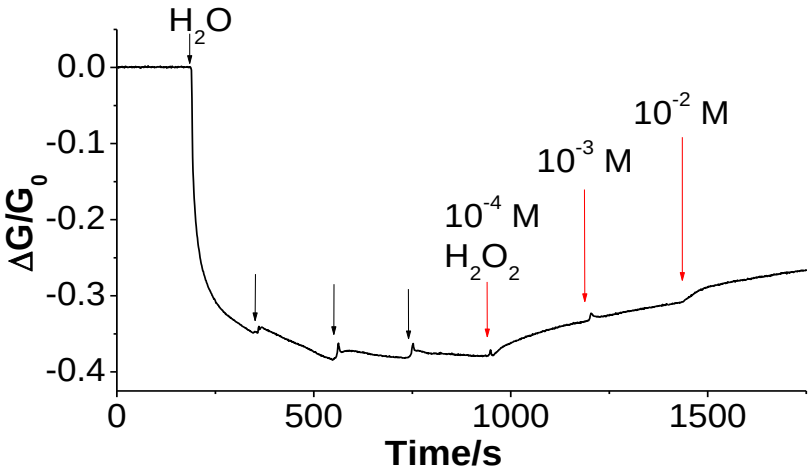

Figure-S 2-8. Relative conductance versus time response to varying concentrations of H_2O_2 of SWNT/EGCG/(Fe_2O_3 Nanoparticle) composite. The composite was prepared by mixing and sonicating the components together.

Calculation of the Thin Film Conductivities:

We measured the conductances of the thin films of SWNT/EGCG or SWNT spray-coated on quartz slides (1 in × 1 in) (Figure-S 2-9a). To calculate the conductivity, we can visualize the thin film as illustrated by Figure-S 2-9b.

Conductivity $\sigma = \frac{1}{\rho}$, where ρ is the Resistivity. (1)

Resistivity $\rho = \frac{RA}{L}$, where R is the electrical resistance,(2)

Electrical resistance $R = \frac{1}{G}$, where G is the electrical conductance,(3)

Conductivity $\sigma = \frac{1}{\rho} = \frac{L}{RA} = \frac{GL}{A}$, where L is the length of the film and A is the cross-sectional area. (4)

As can be seen from Figure S9a, L is 1.5 cm. The thickness of thin film was measured to be approximately 70 nm (Figure-S 2-5) and the width is 2.54 cm (1 inch), so the area A is 1.78×10^{-5} cm^2. Using the equation (4) above, we can convert the measured electrical conductance into conductivity. The conductivity of the SWNT/EGCG thin film is 22.9±5.1 S/cm and the conductivity of the SWNT thin film is approximately 27.4±8.9 S/cm.

a)

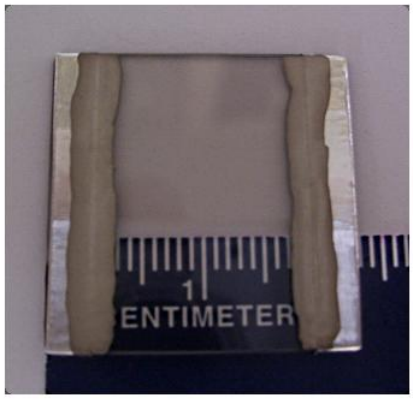

b)

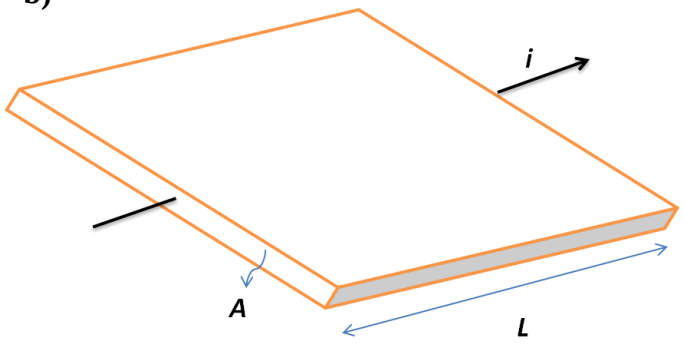

Figure-S 2-9. (a) A photograph of transparent and conductive SWNT/EGCG film on a quartz slide. (b) Schematic illustration of thin film. The black arrow shows the direction of the current *i*, *L* is the length of the film and *A* is the cross-sectional area.

3.0 NANOELECTRONIC DETECTION OF LECTIN-CARBOHYDRATE INTERACTIONS USING CARBON NANOTUBES

3.1 CHAPTER PREFACE

The aim of this work was to use SWNTs and porphyrin-glycoconjugate platforms for the detection of lectin-carbohydrate interactions. These interactions are involved in a wide range of biological processes. Specifically, SWNT FETs were functionalized noncovalently with prophyrin-based glycoconjugates synthesized using "click" chemistry, and changes in electrical conductance was observed upon binding of specific lectins. The material contained in this chapter was published as an article in the journal *Nano Letters*; the figures and tables in this chapter have been reproduced with permission from *Nano Letters* **2011**, *11*, 170. Copyright 2011 American Chemical Society; the full citation is listed as Reference 81 in the bibliography section.

List of Authors: Harindra Vedala, Yanan Chen, Samy Cecioni, Anne Imberty, Sébastien Vidal, and Alexander Star

3.2 INTRODUCTION

Carbohydrates are major components of the cell membrane and are involved in diverse biological processes such as cell growth and development, cell-cell communication, pathogen binding, inflammation, tumor cell metastasis, immune responses, and mediating cell adhesion through carbohydrate-carbohydrate or carbohydrate-receptor interactions.[82] Lectins are sugar-binding proteins that play an important role in biological recognition involving glycoconjugates and possess high specificity for their cognate sugar moieties. In general, they have weaker interactions than antigen-antibody complexes and their dissociation constants are in the range of $K_d = 10^{-6}$ - 10^{-7} M for glycoproteins.[83] Understanding and mimicking specific interactions between carbohydrates and lectins which are used in bacterial or viral adhesion[84] is a challenging task that could lead to improvements in pathogen detection and inhibition of bacterial or viral infections. The existing methods for probing lectin−carbohydrate interactions using biosensors are tedious, requiring extensive instrumental setup and technical expertise.[85] Accordingly, there are critical needs for developing effective new glycotechnologies and biosensors that are sensitive, rapid, simple, reliable and cost-effective. In this regard, single-walled carbon nanotubes (SWNTs) because of their excellent electronic properties, high surface-to-volume ratio, and extreme sensitivity to surface adsorption events can be an ideal candidate for investigating carbohydrate interactions.

Some recent examples have demonstrated the possible applications of carbon nanotubes (CNT) for the detection of pathogens[86] or cancer biomarkers.[87] The sensitivity of CNT-containing devices is very impressive, and they in principle should be able to detect ultralow bacterial concentrations in few minutes. The specific interaction of CNTs with bacteria has been already studied by covalent[88] or noncovalent[88c,89] functionalization with carbohydrate

derivatives. Several reports have shown the interactions of carbohydrate-coated CNTs with lectins using pyrene-based glycoconjugates,[89a,b] glycolipids,[89d] glycopolymers,[90] for the noncovalent systems. The covalent functionalization with galactose dendrimers led to selective interactions with *Bacillus* spores.[91] The main focus of these studies has been to develop novel strategies to tailor the interface between CNTs and cells so as to mitigate the toxicity of CNTs, promote drug delivery or to detect dynamic biomolecular cellular secretion.[92] However, the use of CNTs for electronic detection of carbohydrate-protein interactions has not been yet utilized. As it has been demonstrated by our group and others, NTFET devices can electronically transduce interactions with proteins and other biomolecules.[93]

In this work, we investigate the specific binding of glycoconjugates and lectins using SWNTs configured into electrolyte gated field-effect transistors (FETs). SWNT networks act as conducting channels which transduce the binding between glycoconjugates and lectins into electrical signal. Figure 3-1a shows a schematic illustration of glycoconjugate-functionalized NTFET detection platform.

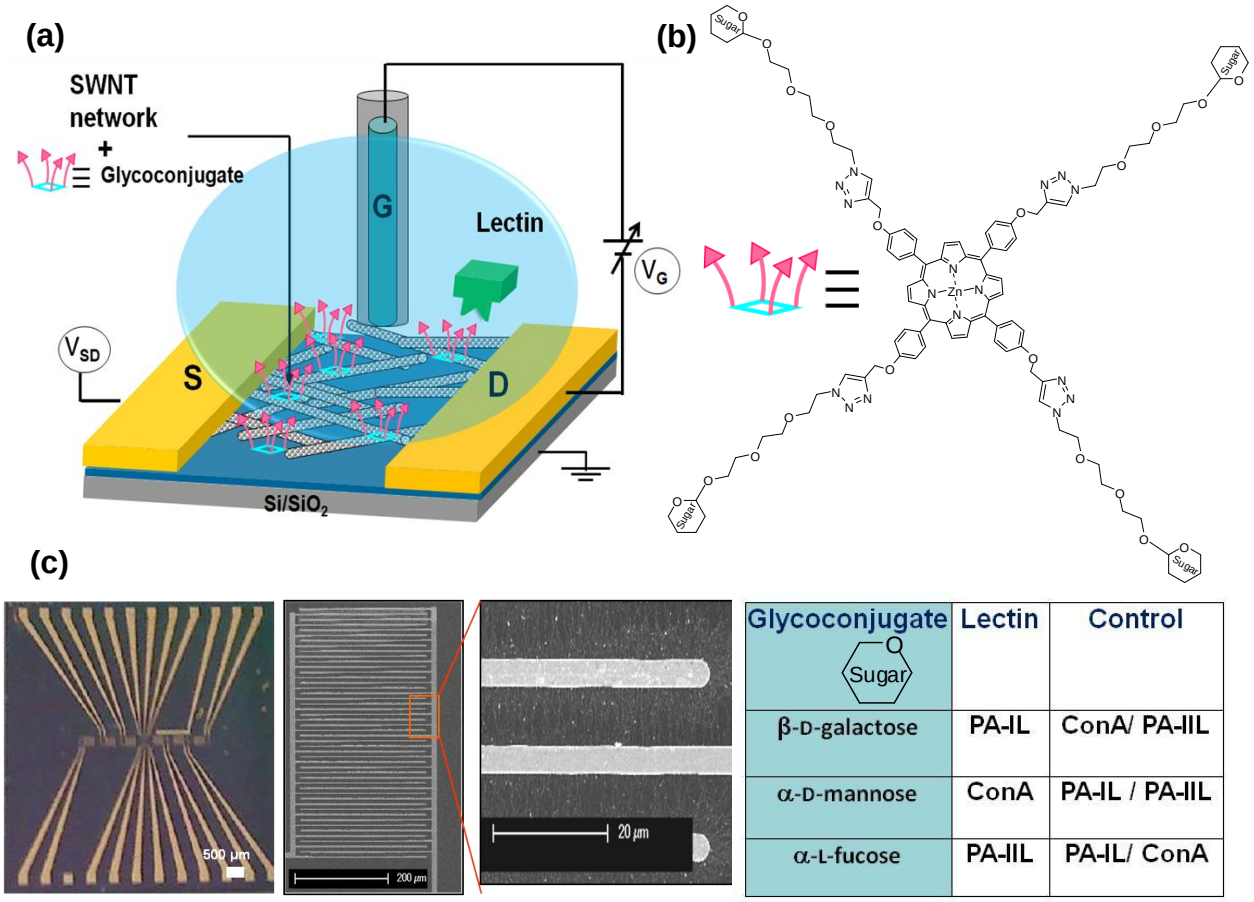

Glycoconjugate (Sugar)	Lectin	Control
β-D-galactose	PA-IL	ConA/ PA-IIL
α-D-mannose	ConA	PA-IL / PA-IIL
α-L-fucose	PA-IIL	PA-IL/ ConA

Figure 3-1. (a) Schematic illustration of glycoconjugate-functionalized single-walled carbon nanotubes (SWNTs)-FET for selective detection of lectins. (b) Chemical structure of porphyrin-based glycoconjugates for noncovalent functionalization of SWNTs. Table shows the selected glycoconjugates and their specific lectins and controls. (c) Optical image of a Si/SiO_2 chip with micropatterned interdigitated electrodes. SEM image of interdigitated electrodes used for device fabrication. Inset shows the SWNTs deposited by dielectrophoresis technique between the microelectrodes.

Using these devices we studied the interaction between three porphyrin-based glycoconjugates carrying β-D-galactose, α-L-fucose and α-D-mannose epitopes and their selective lectins PA-IL, PA-IIL and Concanavalin A (ConA), respectively. Lectin PA-IL (12 kDa) is composed of four subunits of 121 amino acids, binds D-galactose plus its derivatives, and the lectin PA-IIL (11 kDa), composed of four subunits of 114 amino acids, binds L-fucose and other monosaccharides.[94] They are produced in *Pseudomonas aeruginosa* and are involved in the infection process as demonstrated on murine model.[95] *P. aeruginosa* bacteria are involved in cystic fibrosis lung infections, community-infections like otitis and pneumonia, and hospital-acquired infections. ConA (25 kDa) lectin is tetrameric lectin, specific for mannose and glucose and is purified from jack-bean, *Canavalia ensiformis*. These three lectins require divalent cations for activity; calcium ions play a direct role in bridging amino acids and sugars in PA-IL and PA-IIL binding sites[96] while calcium and manganese maintain the active conformation of a loop in ConA.[97] In addition to FET measurements, several other characterization methods, such as fluorescence microscopy, UV-vis-NIR absorption spectroscopy, atomic force microscopy (AFM), and contact angle measurements were performed to substantiate the electronic detection results.

3.3 EXPERIMENTAL

Materials and Methods. Single-walled carbon nanotubes (SWNTs) were procured from Carbon Solutions Inc. (P2-SWNT). PA-IL and PA-IIL lectins were provided by collaborators in France. ConA (25 kDa) lectin was purchased from Sigma and was used without further purification.

Glycoconjugates were synthesized by collaborators and the details of synthesis can be found in reference. [81]

FET Measurements. NTFET devices were fabricated by patterning interdigitated microelectrodes (source-drain spacing of 5 μm) on top of 200 nm oxide layer on Si substrates using photolithography and e-beam evaporation of 30 nm Ti and 100 nm of Au. SWNTs were procured from Carbon Solutions Inc. and were used as conducting channels in these FETs. Alternating current dielectrophoresis (DEP) technique was used for selective deposition of SWNT networks from N,N-dimethylformamide (DMF) suspension onto each interdigitated microelectrodes pattern.[75] The dielectrophoresis parameters namely a.c frequency (10MHz), bias voltage (8 Vpp) and bias duration (60 s) were used to yield SWNT network devices with similar electrical conductance (0.1 – 1 mS). Each Si chip comprising of multiple FET devices was then placed onto a standard ceramic dual in-line package (CERDIP) and wirebonded. Two Keithley 2400 sourcemeters were used for FET measurements. The electrical performance of each device was investigated in electrolyte gated FET device configuration. The conductance of NTFET device was tuned using the electrolyte as a highly effective gate.[80a,98] A small fluid chamber (1 mL) was placed over the NTFET device to control the liquid environment using phosphate buffer solution (PBS) (20 mM) at pH 7. A liquid gate potential (−0.75 V to +0.75 V) with respect to the grounded drain electrode was applied using an Ag/AgCl (3 M KCl) reference electrode submerged in the electrolyte. The drain current of the device was measured at a constant source-drain voltage of 50 mV. Transfer characteristics (i.e., conductance (G) versus gate voltage (V_g)) were measured to investigate the interactions between glycoconjugates and lectins. Figure 3-1c shows the optical image of the chip consisting of multiple devices and scanning electron microscope (SEM) images (Phillips XL30 FEG) of a single device after DEP of SWNTs.

Imaging. Scanning electron microscopy (SEM) was performed with a Phillips XL30 FEG at acceleration voltage of 10keV. Atomic force microscope (AFM) images were obtained using scanning probe microscope (Veeco Nanoscope II) in a tapping mode configuration. Samples were prepared by spin coating bare SWNTs onto a poly-L-lysine treated freshly cleaved sheet of mica substrate. Then the mica was incubated with porphyrin-glycoconjugates for noncovalent functionalization. Lectin incubation was done following the same procedure as FET device incubation. The images were taken after 30 min of drying in ambient and subsequent washing with PBS solution (for functionalized SWNTs).

UV-vis-NIR Spectroscopy. UV-vis-NIR spectra were obtained using Perkin-Elmer Lambda 900 UV-vis-NIR spectrophotometer. Samples were prepared by spray casting SWNTs (in DMF suspension) onto 1" x 1" quartz substrates quartz plate heated to 185 ℃ using a commercial air gun (Iwata, Inc.). Subsequent glycoconjugate functionalization was performed at room temperature.

Fluorescence Microscopy. Fluorescence microscopy was performed using Olympus Provis (AX 80). Lectins, Canavalia ensiformis agglutinin (ConA) conjugated with Alexa Fluor 488 (ConA-Alexa 488), were obtained from Invitrogen. In a typical experiment, a 1 mL solution of lectin-Alexa 488 conjugates (300 μg / mL) in PBS buffer containing 5 μM Ca2+ was added to the suspensions of glycoconjugate coated SWNT devices. The reactions were incubated for 40 min at room temperature in the dark. The chips were analyzed at 517 nm using a fluorescence microplate reader. Fluorescence intensities were corrected for background fluorescence by subtracting the fluorescence intensities of glycoconjugate coated SWNT alone.

3.4 RESULTS AND DISCUSSION

To selectively detect lectins, NTFET devices were noncovalently functionalized with porphyrin-based glycoconjugates. The experimental details for their synthesis are described in the reference [81]. Briefly, propargylated porphyrin was prepared from *p*-propargyl-benzaldehyde and pyrrole then metallated with $ZnCl_2$ to afford the desired propargylated core. The corresponding azido-functionalized carbohydrates were then conjugated by azide-alkyne "click" chemistry to afford the acetylated glycoclusters which were then converted to the hydroxylated final glycoconjugates. Surface functionalization of NTFETs with each glycoconjugate was performed by incubating the Si chips in 2 μM solution of the glycoconjugates (in deionized water) for two hours followed by rinsing with deionized water. This was followed by incubating the chips for 40 minutes in different concentrations of lectin solutions prepared in PBS with 5 μM $CaCl_2$ and latter washed three times with PBS solution. Figure 3-1b shows the chemical structure of porphyrin-based glycoconjugates with their specific binding lectins and controls, used in this study.

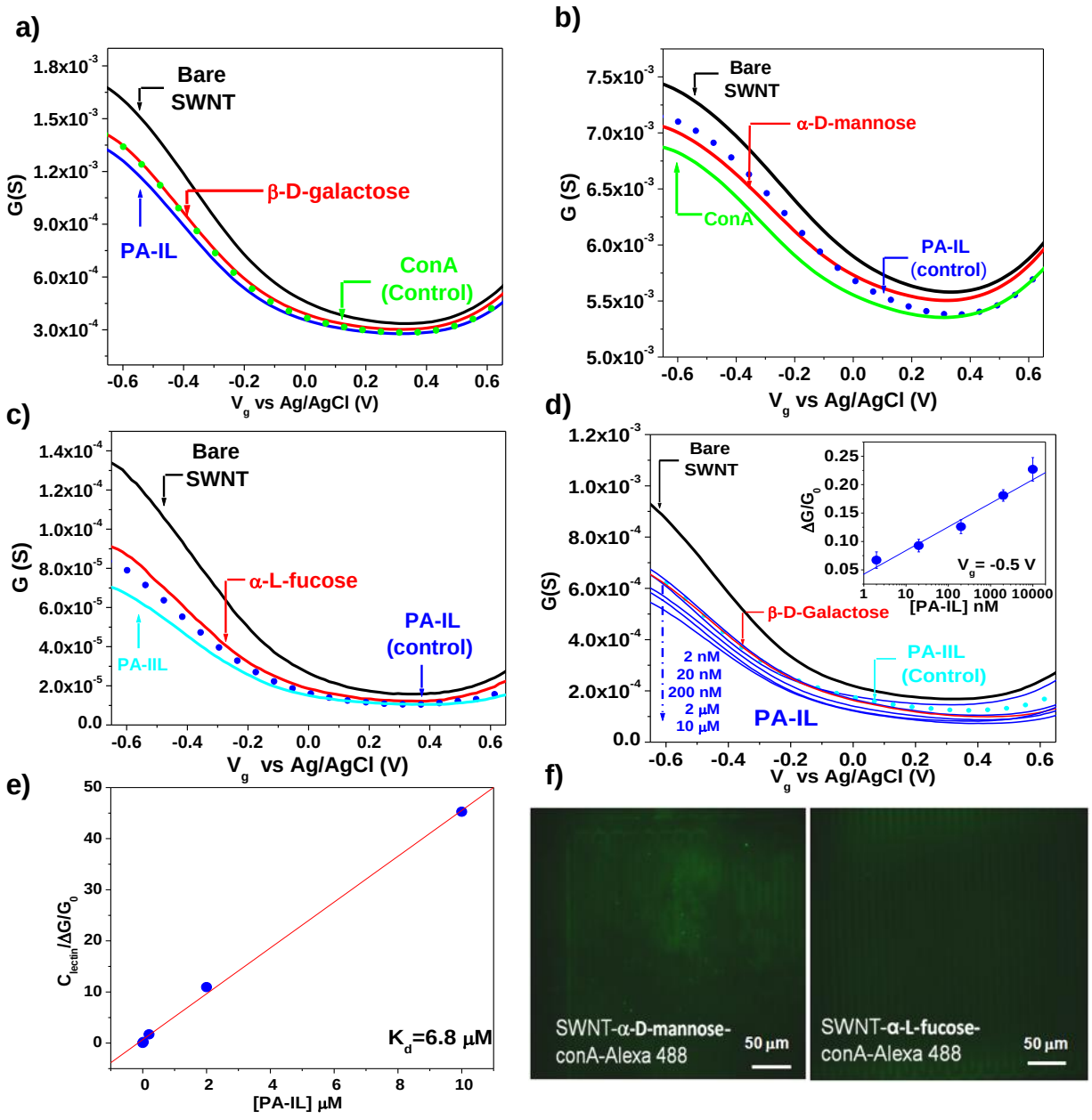

Figure 3-2. Electronic detection of carbohydrate-lectin interactions: Conductance (G) vs gate voltage (V_g) of bare NTFET device, after functionalization with (a) β-D-galactose, (b) α-D-mannose, (c) α-L-fucose and after attachment with 2 μM selective lectin and their controls. (d) Same experiment as in panel (a) with PA-IIL as control and varying concentration of the selective lectin (PA-IL) (2 nM-10 μM). Inset shows the biosensor calibration plot: normalized change in the device conductance versus PA-IL concentration. (e) Langmuir isotherm of data presented in panel (d) with calculated lectin dissociation constant (K_d). Lectin

binding experiments were performed in the presence of 5 μM Ca^{2+}. (f) Fluorescence image of ConA-Alexa 488 attached on α-D-mannose (left panel) and α-L-fucose (right panel) functionalized SWNTs.

We measured a total of 20 NTFET devices. The liquid gate FET measurements of bare NTFETs exhibited either a p-type or ambipolar device characteristics (Figure 3-2). Because of the presence of metallic SWNTs in the network the ON/OFF ratio of the device was below 10^2. After functionalization with the porphyrin-based glycoconjugates, a decrease in ON conductance with a slight negative shift in gate voltage was observed (Figure 3-2a). Similar decrease in conductance was observed for all the three glycoconjugates indicating that the noncovalent interactions between metalloporphyrin core and SWNT dominate the signal (Figure 3-2b and c). Furthermore, the decrease in device conductance can be attributed to the screening of charge in the SWNT network as a result of the presence of electron donating Zn-porphyrin molecules.[99] In a control experiment, zinc tetraphenyl porphyrin (ZnTPP) showed a similar response on transfer characteristics of NTFETs confirming the dominant role of Zn-porphyrin and its π-π interaction with SWNT sidewalls Figure 3-2a).

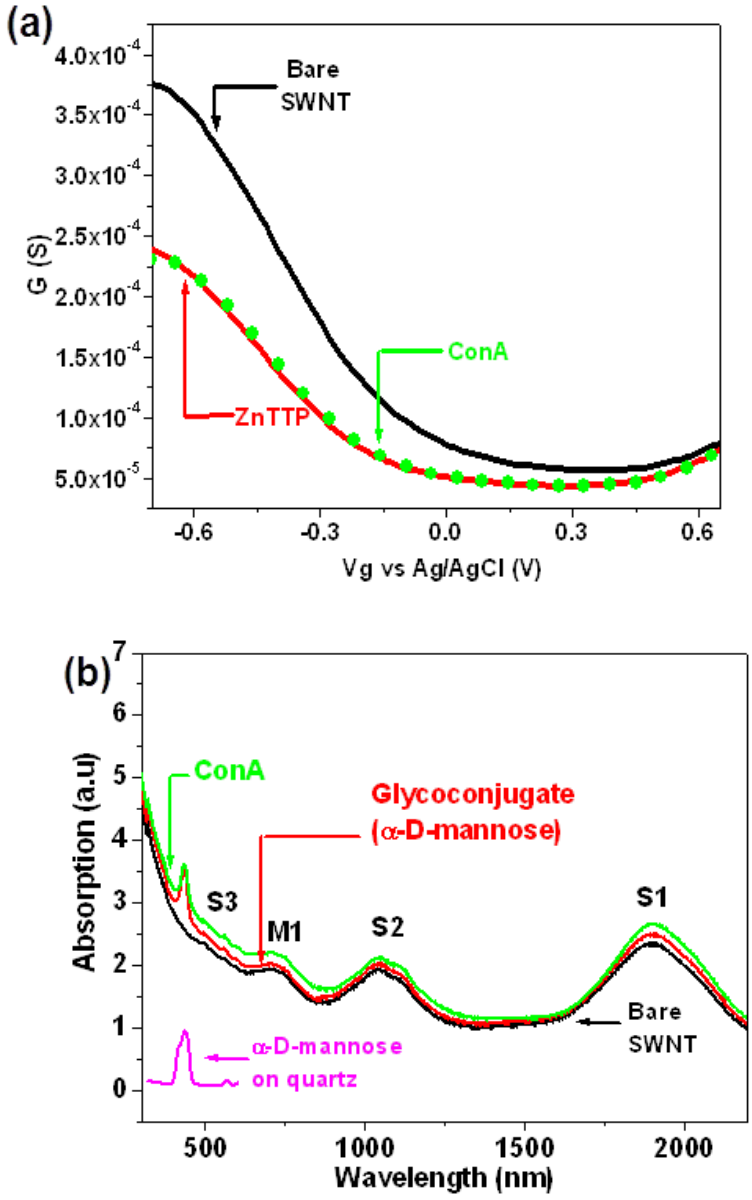

Figure 3-3. (a) G vs V_g curves for bare SWNT, after ZnTTP functionalization (without glycoconjugate) and after ConA (mannose specific lectin)(green). (b) UV-vis absorption spectra of pristine SWNTs, after functionalization with α-D-mannose and after ConA (mannose specific lectin).

Additionally, UV-vis-NIR absorption spectroscopy was employed to investigate the interaction between SWNTs and metalloporphyrin. UV-vis-NIR absorption spectroscopy is a useful technique to probe electron transfer in SWNTs as they have unique electronic structure with several van Hove singularities.[100] These singularities produce peaks in the SWNT UV-vis-NIR absorption spectra that correspond to either metallic or semiconducting SWNTs. Three semiconducting transitions, called S_1 (1845 nm), S_2 (1020 nm), and S_3 (475 nm), and one metallic transition, called M_1 (700 nm), are typically observed in the UV-vis-NIR absorption spectra of a sample of SWNTs, and it has been reported that the intensity of these transitions can be modified via doping the SWNT with holes or electrons. [100] The S_1 band is the most sensitive to the charge transfer as it corresponds to the top of SWNT valence band. In Figure 3-3b besides S_1, S_2 and M_1 bands corresponding to SWNTs an additional peak at 425 nm was observed for SWNT-α-D-mannose conjugates confirming the formation of the desired complex. We also observed an increase in the S_1 band intensity by 6.5% and 13.6% when SWNTs were functionalized with α-D-mannose and its specific binding lectin, ConA, respectively. This increase in S_1 intensity and decrease in the NTFET conductance (Figure 3-2b) can be attributed to the refilling of the partially depleted SWNT valence band with electronic density donated by the binding molecules.

After glycoconjugate functionalization, devices were treated with specific binding lectins and their controls. Figure 3-2a shows the response of a β-D-galactose glycoconjugate functionalized device to various lectins. Upon incubation with non-specific lectin (ConA, 2 μM) the transfer characteristics remained unaffected. However, when treated with the galactose specific lectin (PA-IL, 2 μM) a decrease in ON conductance was observed indicating the selective interaction between the glycoconjugate and the lectin. The decrease in ON conductance can be attributed to the net negative charge of the PA-IL (isoelectric point of 4.94) at the

measured pH of 7 and charge transfer to SWNTs . A similar trend was observed for the other two glycoconjugate functionalizations namely α-D-mannose and α-L-fucose (Figure 3-2b and c and Figure-S 3-1) when treated with their respective specific lectins ConA and PA-IIL and the corresponding controls. In a different control experiment, when a NTFET device was functionalized with only ZnTPP and treated with ConA, the transfer characteristics remained unchanged (Figure 3-3a). This observation indicates that the responses obtained in Figure 3-2 are indeed from specific interaction between glycoconjugates and lectin and not due to non-specific adsorption on Zn-porphyrins or SWNTs. Also we did not observe any significant change in the transfer characteristics of NTFET devices when incubation period was increased from 40 min to overnight (~18 hr) (SI, Figure-S 3-2).

Additionally, the sensitivity of NTFET devices was investigated by plotting the G vs V_g for β-D-galactose glycoconjugate functionalized device (control measurements with 10 μM PA-IIL) for varying concentration (2 nM to 10 μM) of selective lectin PA-IL (Figure 3-2d). The NTFET response to the lowest measured concentration (2 nM) of lectin was similar to the response to 10 μM of the nonspecific lectin (PA-IIL), demonstrating excellent selectivity. The detection limit of NTFET devices was comparable to other techniques traditionally used for different lectin detection such as optical microarray (1.4 nM), electrochemical surface plasmon resonance (E-SPR) (41 nM), electrochemical impedance spectroscopy (5 nM), voltammetric (7 nM) and colorimetric (64 nM).[101] To further understand the kinetics of the glycoconjugate-lectin interactions, and to determine dissociation constant (K_d), $\frac{C_{lectin}}{\Delta G / G_0}$ as a function of C_{lectin} were plotted (where C_{lectin} is lectin concentration and $\Delta G / G_0$ is the relative change in conductance after lectin attachment). Figure 3-2e shows a linear relationship representing a Langmuir isotherm adsorption and a calculated $K_d \sim 6.8$ μM (from the relation:

$\frac{C_{lectin}}{\Delta G/G_0} = \frac{1}{(\Delta G/G_0)_{max}} C_{lectin} + \frac{K_d}{(\Delta G/G_0)_{max}}$).[101c] This value appears to be slightly higher than previously determined by titration microcalorimetry (ITC) for the interaction between PA-IL and the galactosylated porphyrin in solution (K_d = 133 nM).[102] The affinity is one order of magnitude weaker, a difference that results likely from the fact that the ligand is free in solution in the ITC experiment, and adsorbed to the surface of a carbon nanotube in the NTFET device. Other techniques based on competing for PA-IL binding to a galactosylated surface, such as inhibition of hemagglutination and SPR, did not give access directly to dissociation constants, but to IC_{50} values in the order of 63 μM and 1.4 μM, respectively.[102] Again these values are in good agreement with the data presented here, confirming that NFTETs can be used for the quantitative determination of affinity constants.

Fluorescence microscopy was utilized to further characterize the specific binding between glycoconjugates and lectins (experimental details in SI). Figure 3-2f shows the fluorescence image of α-D-mannose (left panel) and α-L-fucose (right panel) functionalized NTFETs devices incubated with fluorescently labeled lectin ConA-Alexa 488 which shows specific binding to α-D-mannose. Fluorescence signal can be clearly observed from the device with α-D-mannose functionalized device where as only background signal was observed from α-L-fucose indicating specific binding between carbohydrate epitopes and lectins.

To investigate the nonspecific binding of the protein with SWNTs, we incubated bare NTFET device with ConA. We found a decrease in ON conductance for the device indicating that lectin is nonspecifically adsorbed on to the SWNT surface (SI, Figure-S 3-3). Earlier reports on protein adsorption have shown that many different types of proteins adsorb spontaneously onto bare SWNTs from aqueous solution and result in change of transfer characteristics of NTFET.[93c,d] This phenomenon was attributed to the hydrophobic interactions between proteins

and SWNT surface.[103] A comparison of hydrophobicity of bare SWNTs and glycoconjugate-functionalized SWNTs showed a change in contact angle from nearly hydrophobic (87°) to hydrophilic (55°) (SI, Figure-S 3-4). This observation corroborates that glycoconjugate functionalization serves the dual purpose of selectively detecting lectin binding as well as preventing the nonspecific protein binding to SWNTs.

Finally, AFM imaging was performed to observe the surface morphology of the SWNTs at different stages of functionalization. An average height of around 3.4 nm was observed for bare SWNTs indicating that SWNTs were bundled (Figure 3-4a). After functionalization with glycoconjugates (α-D-mannose) the total height varied between 11 nm and 14 nm indicating an increase of 8-10 nm. Earlier reports on SWNT-porphyrin complexes have shown a height range between 2-4 nm.[104] Based on the AFM image, we attribute the further increase in the height to the presence of carbohydrate moieties on the Zn-porphyrin molecules (Figure 3-4b). Later, when glycoconjugate functionalized SWNTs were exposed to specific binding lectin (in this case ConA for α-D-mannose) an increase in height of about 5-7 nm was observed (Figure 3-4c). Typically, ConA is observed as a tetramer in solution at pH $\geq$ 7 and the molecular dimensions of tetramer are 60 x 70 x 70 Å (Protein DataBank, 1CN1) from X-ray diffraction studies.[105] The height measurements obtained by AFM are in good agreement with the results obtained from X-ray studies and AFM analysis.[106]

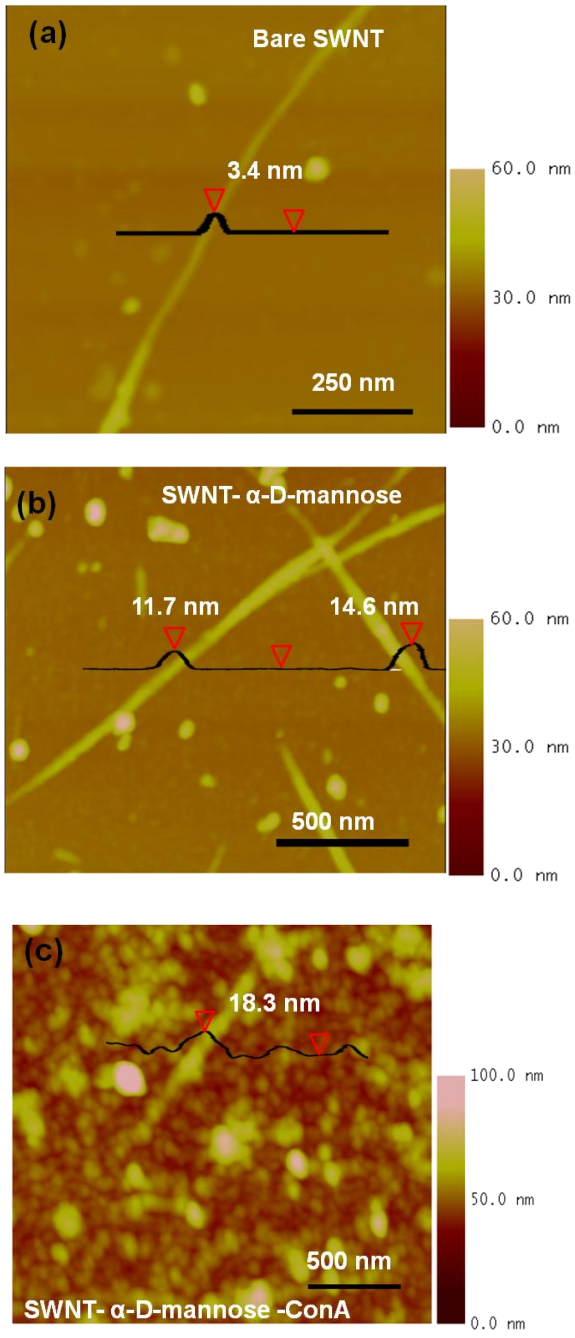

Figure 3-4. Atomic force microscope images of (a) bare SWNTs, (b) SWNT functionalized with α-D-mannose glycoconjugate, and (c) after ConA attachment. Lectin attachment was performed in the presence of 5 µM Ca^{2+}.

3.5 CONCLUSIONS

In conclusion, we have demonstrated a novel detection platform using NTFET devices for highly selective detection of interactions between glycoconjugates and bacterial lectins, which exhibit specific multivalent binding to carbohydrates. The interaction between lectins and glycoconjugates was transduced as change in the device conductance. Noncovalent functionalization of the devices with glycoconjugates facilitated in preventing non-specific protein adsorption and highly selective lectin binding. This nano-detection platform shows potential to be combined with microfluidic systems and utilized in the future to identify a bacterium within a crude sample from a water system, soils or human specimens and aid in preventing disease outbreaks and preserving public health.

3.6 ACKNOWLEDGEMENT

The authors wish to thank Albert Stuart and the Department of Materials Science and Engineering at the University of Pittsburgh for access to and assistance with the SEM. We also thank Center for Biologic Imaging at the University of Pittsburgh for access and assistance with fluorescence microscopy. The authors thank the Université Claude Bernard Lyon 1 and the CNRS for financial support. S.C. thanks the Région Rhône-Alpes (Cluster de Recherche Chimie) and the CNRS (Programme Interdisciplinaire: Chimie pour le Développement Durable) for additional funding. Financial help is acknowledged from Vaincre la Mucovisdicose and GDR Pseudomonas. A.I. acknowledges funding from ANR Glycoasterix. Dr D. Bouchu, C. Duchamp and N. Henriques are gratefully acknowledged for mass spectrometry analyses.

3.7 SUPPORTING INFORMATION

FET control experiments data and contact angle measurements are presented in the supporting informations.

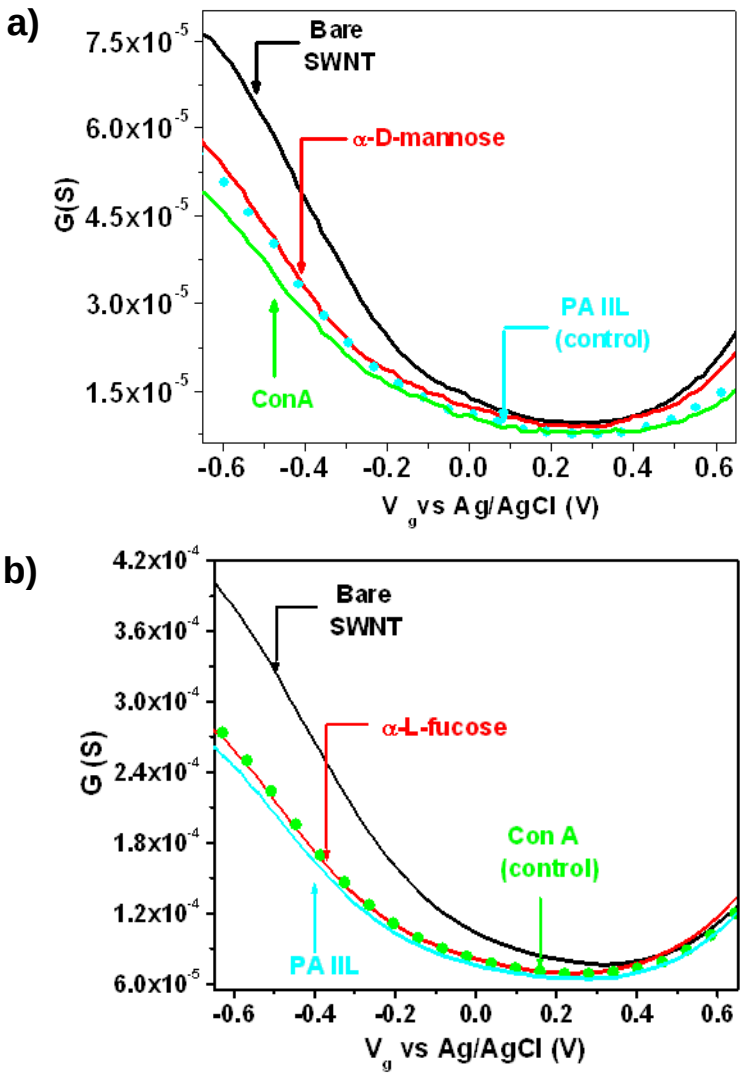

Figure-S 3-1. G vs Vg data for NTFET devices functionalized (a) with α-D-mannose glycoconjugate and measured after incubation with 2 µM ConA lectin (PA IIL as control) and (b) with α-L-fucose glycoconjugate and measured after attachment with 2 µM selective PA-IIL lectin (Con A as control). Lectin incubations were 40 min and measurements were done in 20 mM PBS (pH 7) with 5 µM Ca^{2+}. V_{ds} = 50 mV.

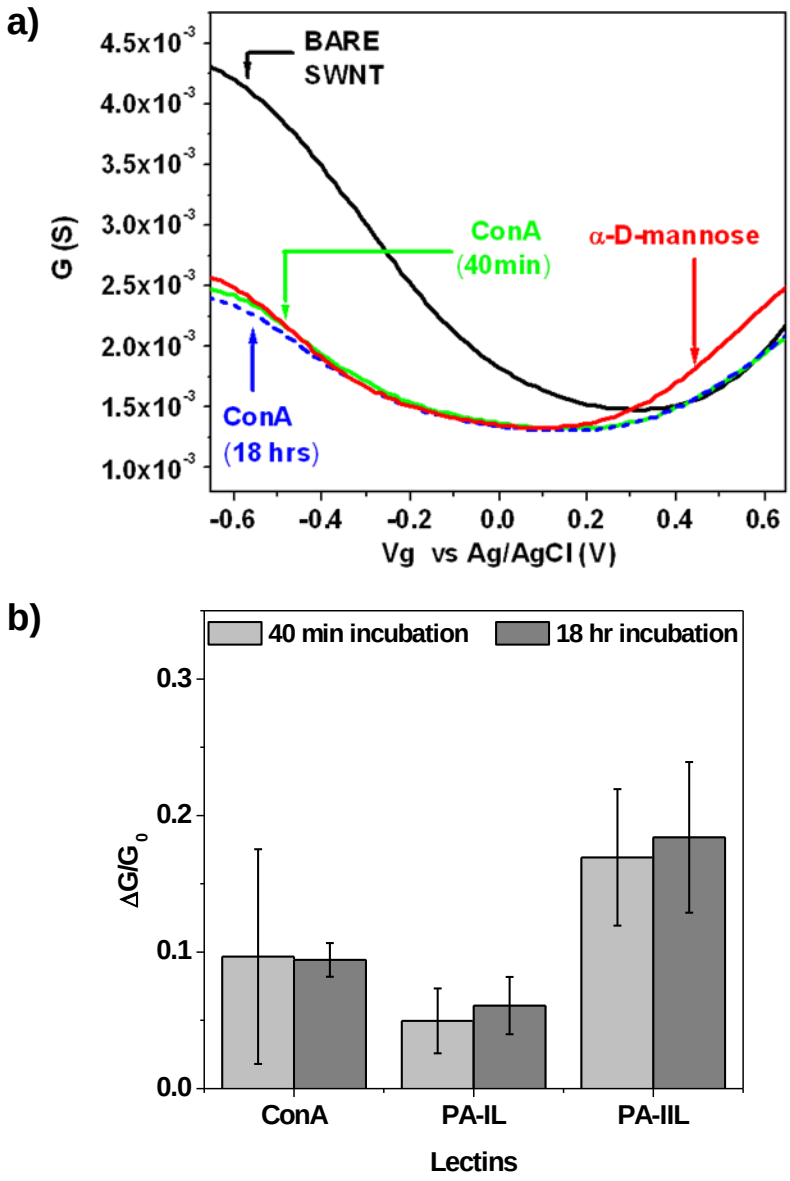

Figure-S 3-2. (a) G vs Vg curves for bare SWNT, glycoconjugate α-D-mannose functionalized SWNT device measured after 2 µM ConA lectin (in PBS(pH 7) with 5 µM Ca^{2+}) solution for 40 min (solid line) and 18 hrs (dashed line). (b) Relative response of a total of 15 different NTFET devices incubated with lectins for 40 min and 18 hrs. NTFET devices were functionalized with α-D-mannose, β-D-galactose and α-D-fucose glycoconjugates for selective detection of 2 µM PA-IL, PA-IIL and ConA lectins, respectively (in PBS (pH 7) with 5 µM Ca^{2+}). The relative response was measured at Vg = − 0.5 V.

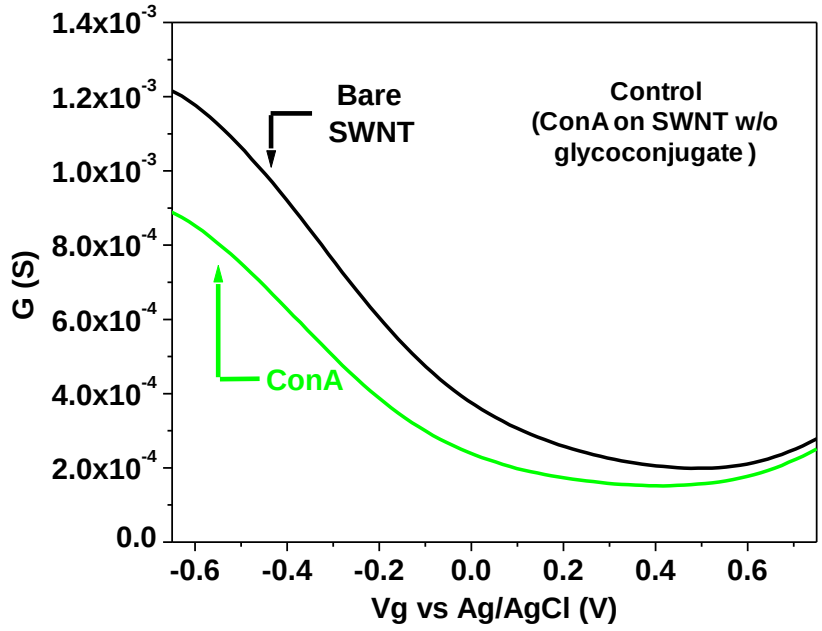

Figure-S 3-3. G vs Vg curves measured for bare SWNT, and after 2 µM ConA lectin (in PBS (pH 7) with 5 µM Ca^{2+}) attachment.

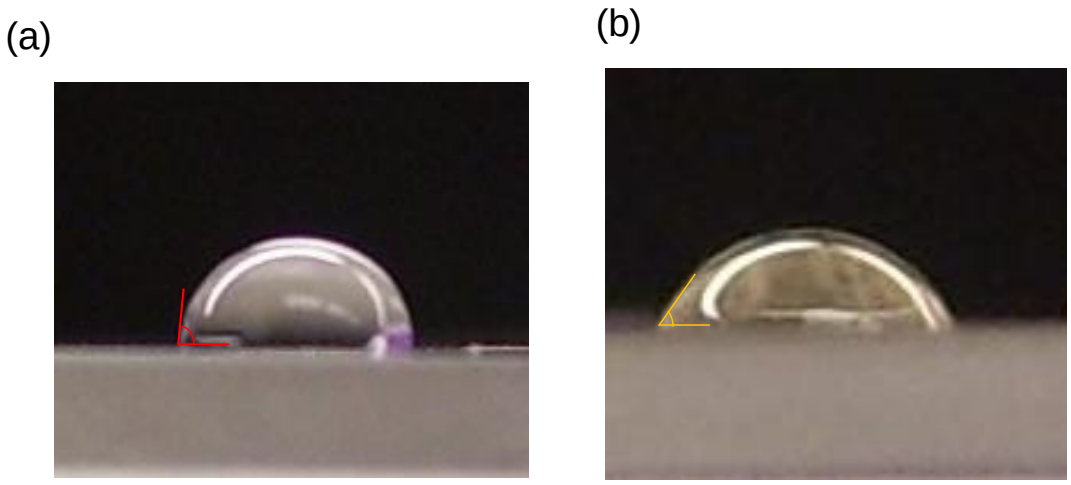

Figure-S 3-4. Contact angle of water droplet on quartz substrate with (a) spray casted bare SWNT (87°) and after (b) Glycoconjugate (α-D-mannose) functionalization (55 °).

4.0 ELECTRONIC DETECTION OF LECTINS USING CARBOHYDRATE FUNCTIONALIZED NANOSTRUCTURES: GRAPHENE *VERSUS* CARBON NANOTUBES

4.1 CHAPTER PREFACE

The aim of this work was to investigate the interactions between lectins and carbohydrates using FET devices comprised of CCG and SWNT. Pyrene- and porphyrin-based glycoconjugates were functionalized noncovalently on the surface of CCG-FET and SWNT- FET devices. Glycoconjugate surface coverage in addition to one-dimensional structures of SWNTs resulted in optimal lectin detection. The material contained in this chapter was published as an article in the journal *ACS Nano*; the figures and table in this chapter have been reproduced with permission from *ACS Nano* **2012**, *6*, 760. Copyright 2012 American Chemical Society; the full citation is listed as Reference 107 in the bibliography section.

List of Authors: Yanan Chen, Harindra Vedala, Gregg P. Kotchey, Aymeric Audfray, Samy Cecioni, Anne Imberty, Sébastien Vidal, and Alexander Star

4.2 INTRODUCTION

Because of their unique physical and chemical properties, single-walled carbon nanotubes (SWNTs) and more recently graphene have attracted considerable interest for the development of biosensors.[49,86a,108] These carbon nanostructures are both just one atom thick, and their electronic properties are extremely sensitive to adsorption of chemical species on their surface. They have been successfully configured into field-effect transistor (FET) devices, which can be used for ultrasensitive detection of many chemical and biological molecules including proteins.[49,108a]

Lectins are a class of nonimmune proteins that bind mono- and oligosaccharides reversibly and with high specificity.[82] Lectins have weak interaction with carbohydrates, in the forms of glycoprotein, glycolipids and glycans in biological systems with dissociation constants (K_d) in the millimolar to micromolar range.[83a,83c,d] These interactions are involved in various biological processes, including cell-cell communication, pathogen binding, tumor cell metastasis, and immune responses. It is important to understand and mimic carbohydrate and bacterial lectins interactions as the foundation of pathogen detection and prevention of bacterial infection.[84b,c,109]

Although carbon nanostructures have been functionalized using both covalent and noncovalent methods to induce specific lectin affinity,[89b,89d,90a,91a,92] noncovalent functionalization route preserves physico-chemical properties (*i.e.* electrical conductivity) required for FET device operation. Utilizing this methodology, we have recently reported the noncovalent functionalization of SWNTs with glycosylated porphyrins for detection of lectins with a SWNT-based FET device.[81]

In this work, we further investigated carbohydrate-lectin interactions with both SWNTs and chemically converted graphene (CCG), towards developing carbon nanostructure-based

biosensors. In addition to glycosylated porphyrins, we also used pyrene-based glycoconjugates with both nanostructures. It should be mentioned here that among polynuclear aromatic compounds,[110] pyrene derivatives are recognized as highly effective labelling agents that are capable of forming π-π stacking interactions with graphitic surfaces.[111] To date, pyrene-SWNT conjugate systems have been implemented with monosaccharides[89b,92] or glycodendrimers[89a] for lectin biosensing, drug delivery or interfacing with living cells. Here we investigated SWNT-FET and CCG-FET devices noncovalently functionalized with pyrene- and porphyrin-based glycoconjugates carrying β-D-galactose, α-D-mannose and α-L-fucose for nanoelectronic detection of lectins PA-IL, PA-IIL and concanavalin A (ConA).

Lectin PA-IL and PA-IIL are produced in *Pseudomonas aeruginosa* together with other secondary metabolism virulence factors under quorum-sensing control and are involved in the infection process as demonstrated by the murine model.[94a,112] *P. aeruginosa* bacteria are involved in cystic fibrosis lung infections, community-infections like otitis and pneumonia, and hospital-acquired infections.[113] PA-IL (12 kDa) is composed of four subunits of 121 amino acids and binds galactose plus its derivatives. PA-IIL (11 kDa) is composed of four subunits of 114 amino acids and binds fucose and other related monosaccharides. ConA (purified from jack-bean, *Canavalia ensiformis*, 25 kDa) lectin is a tetrameric lectin, which binds mannose and glucose. These three lectins require divalent cations for sugar-binding activity. Calcium ions mediate the binding of PA-IL and PA-IIL to their specific sugar moiety,[114] while calcium and manganese maintain the active conformation of a loop in ConA.[97]

4.3 EXPERIMENTAL

Materials and methods. Single-walled carbon nanotubes (SWNTs) were procured from Carbon Solutions Inc. Reduced graphene oxide (RGO), a.k.a. chemically converted graphene (CCG), was prepared as described elsewhere.[22,115] Briefly, graphite oxide was synthesized utilizing a modified Hummers' method on graphite flakes (Sigma Aldrich) that underwent a preoxidation step.[115b] Graphite oxide (~ 0.125 wt%) was exfoliated to form graphene oxide *via* 30 minutes of ultrasonification followed by 30 minutes of centrifugation at 3400 revolutions per minute (r.p.m.) to remove unexfoliated graphite oxide (GO). Graphene oxide was then reduced to CCG with hydrazine hydrate (Sigma Aldrich) following the reported procedure.[22,115a] Note that hydrazine is extremely flammable and toxic, and proper laboratory technique should be employed when handling this chemical.

PA-IL and PA-IIL lectins were produced in recombinant form, purified on affinity column, extensively dialyzed and lyophylised as described previously.[116] ConA (25 kDa) lectin was purchased from Sigma and was used without further purification.

Synthesis of the pyrene-glycoconjugates 1a, 1b, 1c. The details of carbohydrates synthesis can be found in Ref [81,107].

General procedure for 1,3-dipolar cycloaddition (Method A): The alkyne-functionalized pyrene derivative 4, copper iodide, DIPEA and carbohydrate azido-derivatives 5a-c in DMF were introduced in a Biotage Initiator 2-5 mL vial. The vial was flushed with argon and the solution was sonicated for 30 seconds. The vial was sealed with a septum cap and heated at 110 ℃ for 30 min under microwave irradiation (solvent absorption level : High). After uncapping the vial, the crude mixture was evaporated and then purified by flash silica gel column chromatography to afford the desired acetylated pyrene glycoconjugates 6a-c.

General procedure for deacetylation (Method B): The acetylated pyrene glycoconjugates 6a-c were suspended in distilled MeOH, ultra-pure water and ultra-pure triethylamine (10:1:1, v/v/v). The mixture was stirred under argon at room temperature for 1 to 3 days. Solvents were evaporated off then co-evaporated with toluene. The residue was dissolved in ultra-pure water (5 mL) and lyopholized to afford pure hydroxylated pyrene glycoconjugates 1a, 1b and 1c.

FET measurements. Metal interdigitated devices (Au/Ti, 100 nm/30 nm) with interelectrode spacing of 10 μm were patterned on a Si/SiO_2 substrate using conventional photolithography. Each chip (2 mm × 2 mm) containing six identical devices was then set into a 40-pin ceramic dual in-line package (CERDIP), wire-bonded using Au wire, and isolated by epoxying the device's inner cavity. SWNTs were deposited onto each interdigitated microelectrodes pattern by a.c. dielectrophoresis (DEP) method from a suspension in *N*,*N*-dimethylformamide (DMF) (Agilent 33250A 80 MHz Function/Arbitrary Waveform Generator, with an applied a.c. frequency (10 MHz), bias voltage (8 V_{pp}), bias duration (60 s)).[81] CCG devices were prepared using the same DEP technique but with different parameters (a.c. frequency (300 kHz), bias voltage (10 V_{pp}), bias duration (120 s)).[117]

The electrical performance of each device was investigated using an electrolyte gated FET device configuration. The conductance of the FET device was tuned using phosphate buffer solution (PBS) electrolyte as a highly effective gate. Two Keithley 2400 sourcemeters were employed for FET measurements. A small fluid chamber (1 mL) was placed over the FET device to control the liquid environment using PBS at pH 7. A liquid gate potential (−0.75 V to +0.75 V) with respect to the grounded drain electrode was applied using an Ag/AgCl (3 M KCl) reference electrode submerged in the gate electrolyte. The drain current of the device was

measured at a constant source-drain voltage (50 mV). Transfer characteristics (conductance (G) *versus* gate voltage (V_g)) were measured.

Functionalization of the FET devices with each glycoconjugate was performed by incubating the chips in 20 μM of the glycoconjugates solution (in deionized water) for 2 hr followed by rinsing three times with double-distilled water. After testing the transfer characteristics, the chips were incubated for 40 min in different concentrations of lectin solutions that were prepared in PBS with 5 μM $CaCl_2$ and subsequently washed three times with PBS solution. For each glycoconjugate functionalized device, non-specific lectins were tested first and subsequently washed away. The specific lectin was then added, and the final transfer characteristics were tested again in the configuration mentioned above.

Modeling method. SWNT and graphene sheet were generated using Nanotube Modeler Software (JCrystalSoft, http://jcrystal.com). A semiconducting SWNT with length of 10 nm and diameter of 1.3 nm was built using the chiral indices m=14 and n=4 as described previously.[118] A graphene sheet with dimension 5×10 nm^2 was built using the chiral indices m=20 and n=0. Zinc tetraphenyl porphyrin (ZnTPP) was built starting from the structure of Zn-protoporphyrin IX complexed with cytochrome C (PDB code 1I54). Pyrene and porphyrin galactosylated conjugates were built using the molecular editor in Sybyl software (Tripos, Inc. St Louis), and structures were minimized with the Tripos force-field.[119] Galactosylated porphyrin 2a was manually docked on the SWNT and sheet followed by energy minimization, while keeping the carbon structures fixed. Galactose linkers were adapted in order to generate distances between pair of galactose residues of approximately 3 nm compatible with binding to PA-IL adjacent sites. Final docking was performed by fitting galactose residues in proper location or the binding sites as previously described.[120] A different procedure was used for the two galactosylated

pyrene 1a that were first docked in two adjacent protein binding sites, before stacking the pyrene rings on the SWNT or graphene, with final energy minimization of the linker moiety.

Isothermal titration microcalorimetry (ITC). Recombinant lyophilized lectins were dissolved in buffer (0.1 M Tris-HCl, 6 μM $CaCl_2$, pH 7.5) and degassed (see the Supporting Information for concentration details). Protein concentration was checked by measurement of optical density. Ligands were dissolved directly into the same buffer, degassed, and placed in the injection syringe. ITC was performed with a VP-ITC microcalorimeter (MicroCal Inc.). Lectins were placed into the 1.4478 mL sample cell at 25 ℃. Each titration was performed with 10 μL injections of ligands every 300 s. Data were fitted with MicroCal Origin 7 software according to standard procedures. Two or three independent titrations were performed for each ligand tested.

4.4 RESULTS AND DISCUSSION

Our synthesis of pyrene-based glycoconjugates (**1a**, **1b**, **1c**) and porphyrin-based glycoconjugates (**2a, 2b, 2c**)[81] was achieved through 1,3-dipolar cycloaddition between alkynylated pyrene or porphyrin derivatives and azido-functionalized carbohydrates. The conjugation through Cu(I)-catalyzed alkyne-azide cycloaddition (CuAAC)[121] was preferred to the direct carboxylic acid-amine condensation methodology, which usually requires a significant excess of either reagent and the use of stoichiometric amounts of coupling reagents. In contrast, CuAAC only requires a catalytic amount of copper iodide and consumes a small excess of carbohydrate derivative (1.5 equivalents). The reaction of 1-pyrenebutyric acid **3** with propargyl amine afforded the corresponding amide **4**[122] in nearly quantitative yield. Subsequently CuAAC was performed between alkyne **4** and glycosylated azides **5a-c** under microwave activation[120,123]

to obtain the acetylated pyrene-functionalized carbohydrate derivatives **6a**-**c**. The final deprotection step of acetyl groups was achieved by solvolysis to afford the desired hydroxylated pyrene glycoconjugates **1a**, **1b**, **1c** in high yields (Scheme 4-1). The three glycoconjugates were fully characterized by 1D and 2D NMR and high-resolution mass spectrometry (see Supporting Information). This synthetic methodology has provided three glycosylated probes (β-D-galactose, α-D-mannose, α-L-fucose) ready to be immobilized on SWNTs or CCG for the detection of lectins with three different specificities (Table 4-1). The linker length was chosen on the basis of solubility, flexibility and commercial availability of a desymmetrized triethyleneglycol.

Scheme 4-1. Synthesis of pyrene-based glycoconjugates 1a, 1b, 1c and general structure of porphyrin-based glycoconjugates 2a, 2b, 2c[81]

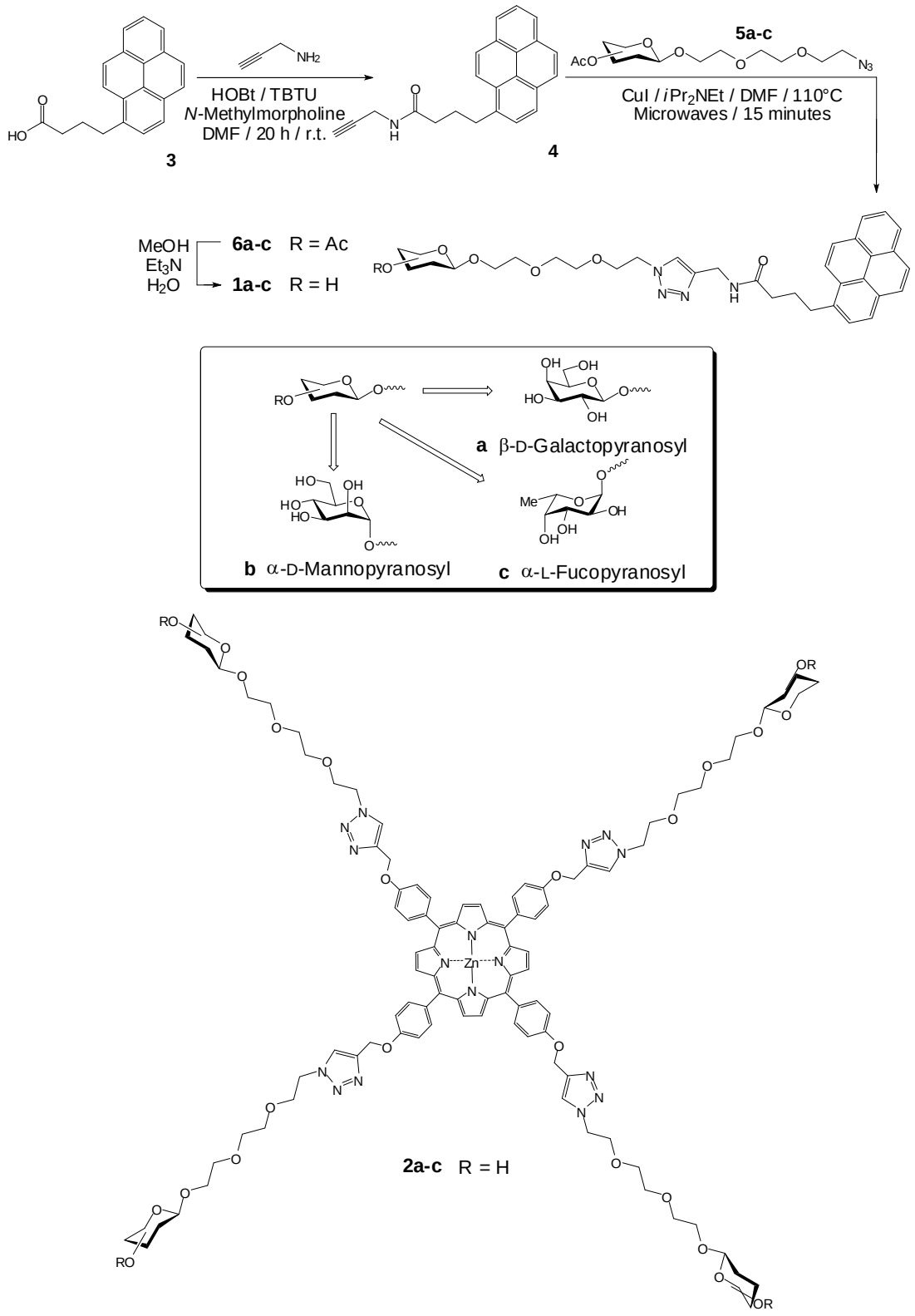

Table 4-1. Glycoconjugates used in this study with their respective specific and control (non-specific) lectins

Glycoconjugate	Lectin	
	Specific	Control
1a or **2a** (galactose)	PA-IL	ConA
1b or **2b** (mannose)	ConA	PA-IL
1c or **2c** (fucose)	PA-IIL	PA-IL

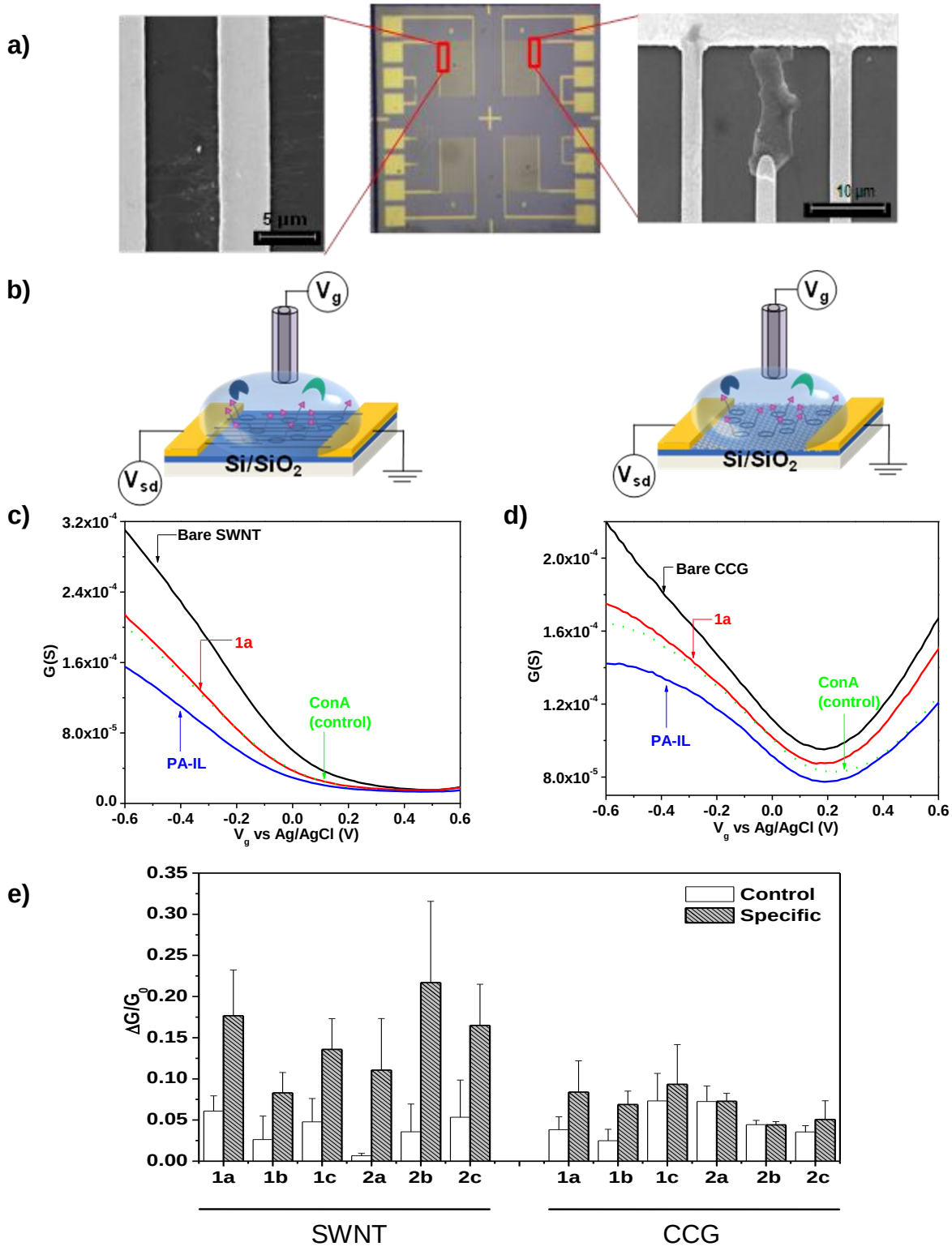

Figure 4-1. (a) Optical image of wirebonded Si chip with multiple photolithography patterned Au/Ti electrodes. Inset shows scanning electron microscopy (SEM) image of one set of the interdigitated electrodes

(left, SWNT-FET; right, CCG-FET). (b) Schematic illustration of the liquid-gated FET configuration (left, SWNT-FET; right, CCG-FET). (c, d) Nanoelectronic detection of carbohydrate-lectin interactions: Conductance (G) vs gate voltage (Vg) of (c) bare SWNT-FET and (d) bare CCG-FET device device after functionalization with β-D-galactose pyrene-based glycoconjugates (1a) and after attachment with 2 μM non-specific (control) lectin ConA and 2 μM specific lectin PA-IL. (e) Comparison of the normalized responses (Vg = –0.5 V) to 2 μM control lectin and to 2 μM specific lectin for biosensors: SWNT+1a, 1b, 1c or 2a, 2b, 2c, CCG+1a, 1b, 1c or 2a, 2b, 2c. All measurements were performed in electrolyte-gated FET configuration in PBS (pH 7), Ag/AgCl reference electrode, with source-drain voltage of 50 mV. Lectin binding experiments were performed in the presence of 5 μM Ca^{2+}.

Field-effect transistor (FET) devices comprising of a CCG or SWNT network were fabricated by patterning interdigitated microelectrodes (source-drain spacing of 10 μm) on top of 200 nm oxide layer on Si substrates using photolithography and e-beam evaporation of 30 nm Ti and 100 nm of Au (Figure 4-1a). Figure 4-1b depicts the schematic illustration of liquid-gated FET configuration with either SWNTs or CCG as the conducting channel. CCG was prepared as described elsewhere[22,115] and was employed as conducting channel in these FETs. CCG and SWNTs were deposited onto the device using an a.c. dielectrophoresis (DEP) method[117] (see Experimental Section). Carbon nanostructures were deposited between fingers of interdigitated microelectrodes, and the DEP method facilitated the alignment of SWNTs.[81]

To selectively detect lectins, SWNT-FET and CCG-FET devices were noncovalently functionalized with pyrene-based glycoconjugates. The noncovalent functionalization of carbon nanostructures with pyrene-based glycoconjugates was performed by incubating the Si chip with FET devices in 20 μM solution of the glycoconjugates (in deionized water) for two hours followed by rinsing with deionized water three times. Upon interaction with pyrene-based glycoconjugates (**1a-c**), a decrease in the FET device conductance with a slight negative shift in

gate voltage was observed (Figure 4-1c and 1d). The decrease in device conductance was attributed to electron donation from pyrene molecules to SWNTs or CCG conducting channels. The interactions were also studied by ultraviolet-visible-near infrared (UV-Vis-NIR) absorption spectroscopy, which indicated the attachment of glycoconjugate to the carbon nanostructures (Figure-S 4-1).

After glycoconjugate functionalization, the FET devices were treated with non-specific lectin (control) and then with specific binding lectins (both 2 μM of lectins in PBS with 5 μM Ca^{2+}). Calcium ions were added to mediate the binding of lectins to their specific sugar moiety.[97,114] As presented in Figure 4-1c, SWNT-FET device functionalized with pyrene-glycoconjugate **1a** was treated with 2 μM non-specific (ConA) and specific (PA-IL) lectins (in PBS with 5 μM Ca^{2+}). Upon treatment with non-specific lectin, the transfer characteristics of the device remained unaffected. A decrease in device conductance was observed after treatment with specific lectin, which indicated selective interaction between the lectin and glycoconjugate. The same experiment with α-D-mannose and α-L-fucose pyrene-based glycoconjugate **1b** and **1c** also demonstrated a similar trend in response and selectivity (Figure-S 4-2).

To compare the CCG- and SWNT-FET devices for lectin detection, similar experiments were performed on pyrene glycoconjugates **1a-c** functionalized CCG-FET devices as well. Figure 4-1d shows the response of the **1a** functionalized CCG-FET devices to various lectins. Compared to p-type SWNT-FET devices, CCG-FET had an ambipolar transfer characteristic and demonstrated different lectin responses at negative and positive gate voltages (p-type and n-type regions). For consistency with SWNT data, we compared the response in p-type region only. Upon incubation with non-specific lectin (ConA), there was a small decrease in conductance at the negative gate voltages, while the decrease in positive voltage region was larger. When

treated with the galactose specific lectin (PA-IL), a decrease was observed primarily at the negative gate voltages. Incidentally, the maximum selectivity of CCG-FET devices was observed at p-type region that allowed direct comparison with SWNT-FET. The same experiments with α-D-mannose and α-L-fucose pyrene-based glycoconjugates **1b** and **1c** showed similar response as the CCG/**1a** configuration (Figure-S 4-3). As an additional control, when bare CCG-FET devices were exposed to ConA, the device conductance decreased due to the non-specific adsorption (Figure-S 4-4).

Figure 4-1e summaries the responses of all tested SWNT and CCG biodetectors to specific and non-specific lectins (**1b**, **1c**, **2a**, **2b** and **2c** data presented in Supporting Info). In all cases we plotted the responses at negative gate voltages (V_g= -0.5 V) that allowed direct comparison between two types of devices. For pyrene-based receptor molecules, SWNT-FET devices demonstrated a larger response and better selectivity for lectin detection than CCG. This may be attributed to the greater sensitivity to lectin adsorption on the transport properties of 1D SWNT than 2D CCG.[124] We also compared the performance of SWNT-porphyrin and CCG-porphyrin (**2a, 2b, 2c**) biodetectors and again SWNT-FET devices showed higher selectivity and response. Although glycoconjugates can have different interactions with either SWNTs or CCG, 1D systems should be generally more sensitive to the lectin binding (Scheme 4-2). Because lectin molecules have a comparable size to the diameter of SWNT, even one molecule can effectively alter the electrical conductivity of SWNTs compared to significantly larger CCG flakes.

Scheme 4-2. Schematic illustration of lectin adsorption effects on an individual SWNT *versus* a single CCG flake.

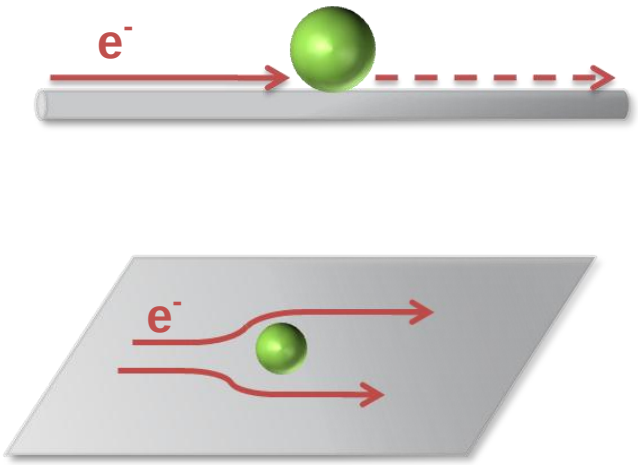

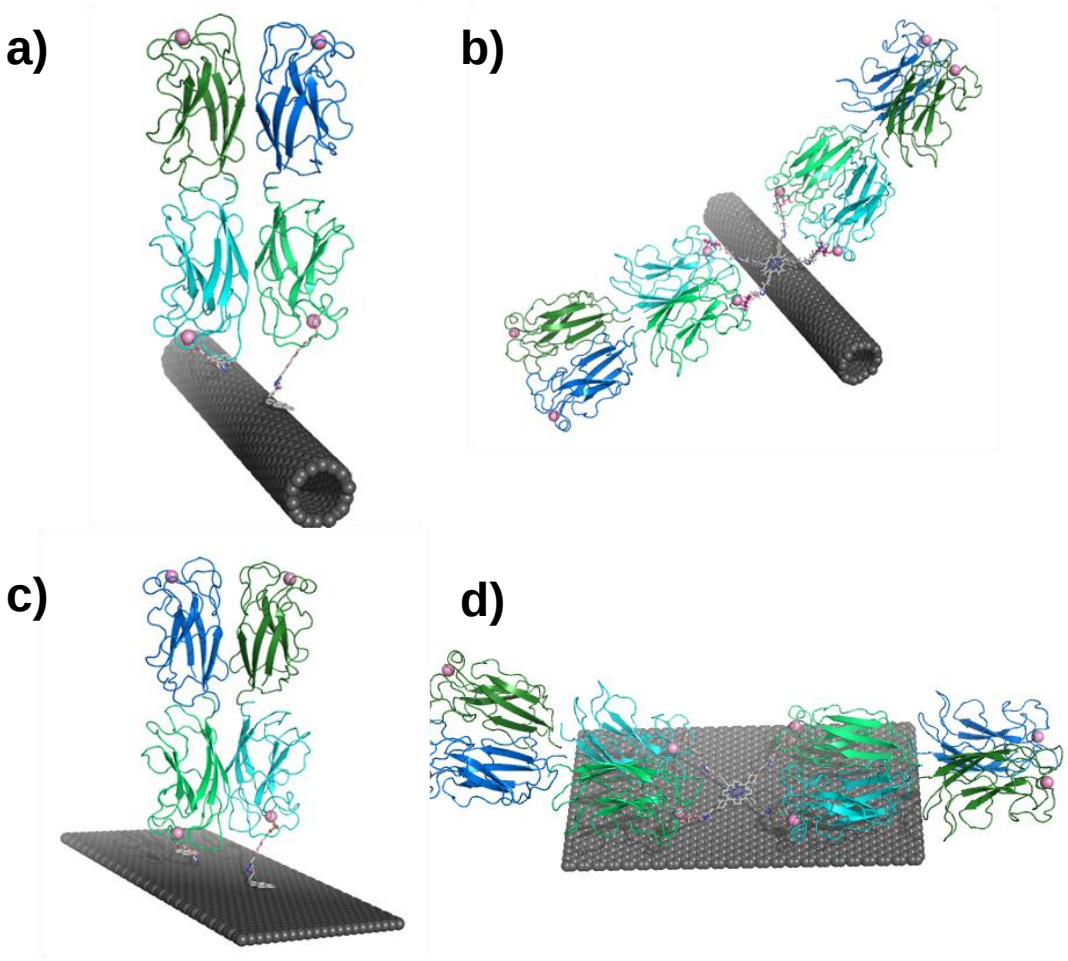

Figure 4-2. Computer-aided models of (a) SWNT/1a/PA-IL interaction, (b) SWNT/2a/PA-IL interaction, (c) CCG/ 1a/PA-IL interaction, and (d) CCG/ 2a/PA-IL interaction.

Since the better response of SWNTs may also be due to carbohydrate accessibility, computational modeling was performed to further understand the interaction between glycoconjugates, carbon nanomaterials, and lectins. Figure 4-2 illustrates molecular models of the interactions between the different carbon nanomaterials associated with galactosylated glycoconjugates and PA-IL lectin. Semiconducting SWNTs were built with chiral indices m=14 and n=4 as described previously,[118] which resulted in nanotubes with 1.3 nm diameter. As displayed in Figure 4-2a and b, the diameter of the SWNT is much smaller than the size of the lectin. The stacking of pyrene or porphyrin moieties of the glycoconjugates on the SWNT yielded galactose residues that are easily accessible for the lectins. Alternatively, stacking the same molecules on CCG resulted in galactose residues that were in close proximity to the carbon sheet and therefore less accessible for lectin binding. This is particularly true for porphyrin conjugates as displayed in Figure 4-2d. Therefore, it can be concluded that the SWNT system provides more flexibility for the sugar moieties to interact with lectin leading to higher sensitivity than the CCG system.

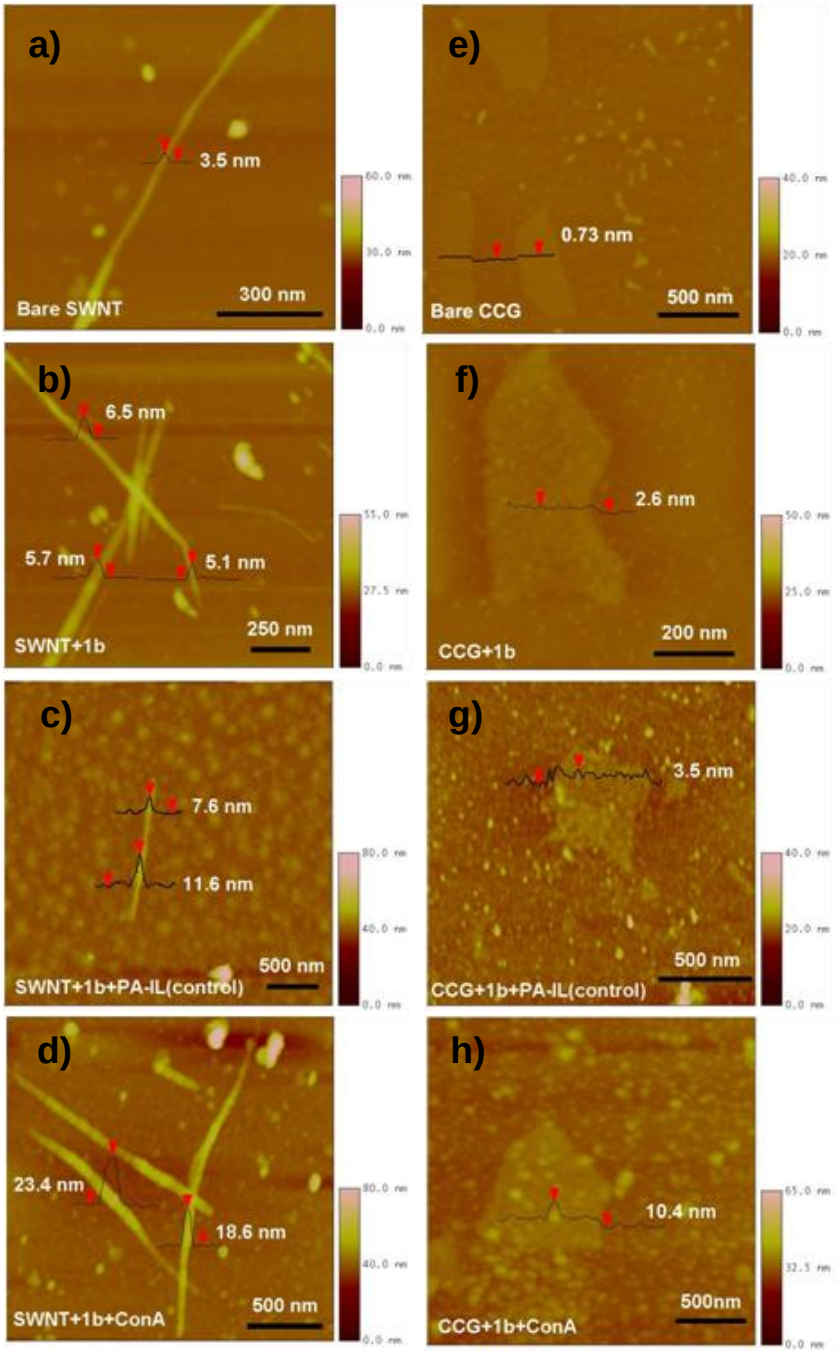

Figure 4-3. Atomic force microscope (AFM) images of (a) bare SWNTs, (b) SWNT functionalized with 1b, (c) after incubation with PA-IL (control) and (d) after ConA attachment; (e) bare CCG, (f) CCG functionalized with 1b, (g) after incubation with PA-IL (control) and (h) after ConA attachment. Lectin attachment was performed in the presence of 5 μM Ca^{2+}.

To obtain evidence of the attachment of glycoconjugates onto the carbon nanostructure surfaces and the interaction between glycoconjugates and lectins, atomic force microscopy (AFM) imaging was performed at different stages of functionalization. The height of bare SWNTs was observed to be around 3-4 nm indicating the presence of SWNT bundles (Figure 4-3a). After functionalization with α-D-mannose glycoconjugates **1b**, the total height increased to 5-7 nm (Figure 4-3b). After incubation with the non-specific lectin PA-IL, the increase in height was 1-3 nm (Figure 4-3c). On the other hand, after exposing the glycoconjugate functionalized SWNTs to the specific binding lectin (ConA for α-D-mannose), an increase in height of more than 10 nm was observed (Figure 4-3d). Bare CCG was observed to be 0.67 ± 0.15 nm in thickness (Figure 4-3e), which indicated the presence of single sheet structure. After functionalization with α-D-mannose glycoconjugates **1b**, the total height increased to 2.44 ± 0.35 nm (Figure 4-3f). When incubating with non-specific lectin PA-IL, the increase in height was merely around 1nm (Figure 4-3g). After exposing the glycoconjugate functionalized CCG to specific binding lectin (ConA for α-D-mannose), an increase in height to 8.25 ± 1.73 nm was observed (Figure 4-3h). The height measurements obtained by AFM were in good agreement with the literature values.[106] Typically, ConA was observed as a tetramer in solution at pH≥7, and the molecular dimensions of tetramer are $60 \times 70 \times 70$ Å (Protein DataBank, 1CN1) as determined from X-ray diffraction studies. It should be mentioned here that, as can be visualized from Figure 4-3d and h, SWNTs are covered continuously while the binding sites are scattered randomly on CCG surface. This indicates that SWNT system provides more adsorption sites for lectins, which is consistent with the computer modelling studies. Additionally, the basal plane of CCG could contain oxygen functional groups (*i.e.* epoxides and tertiary alcohols),[22] which could hinder the π-π stacking of polynuclear aromatic compounds (glycoconjugates) and result in the

lower lectin coverage. It should be mentioned here that the attachment of glycoconjugate to the nanostructure surfaces can effectively prevent the nonspecific binding of lectin. For example, in Figure 4-3c and d, although PA-IL can adsorb nonspecificly onto the poly-*l*-lysine decorated mica surface and form agglomerates, no evidence of nonspecific binding onto the **1b**-decorated carbon nanostructure surfaces was observed. The high coverage of lectins on SWNTs in SWNT-FET devices was further illustrated by fluorescence microscopy. Figure 4-4 depicts the fluorescence image of α-D-mannose functionalized SWNT-FET device incubated with fluorescently labeled lectin ConA-Alexa488, which shows specific binding to α-D-mannose. SWNTs (aligned by DEP between fingers of interdigitated electrodes) clearly exhibit high fluorescence indicating high coverage of ConA. Due to the fluorescence quenching effect of graphene,[30] no representative image of graphene flakes was obtained using fluorescence microscopy. The preferential lectin binding in addition to its pronounced effect on the electrical conductivity (Scheme 4-2) can explain the observed larger response and better selectivity of SWNT-FET devices.

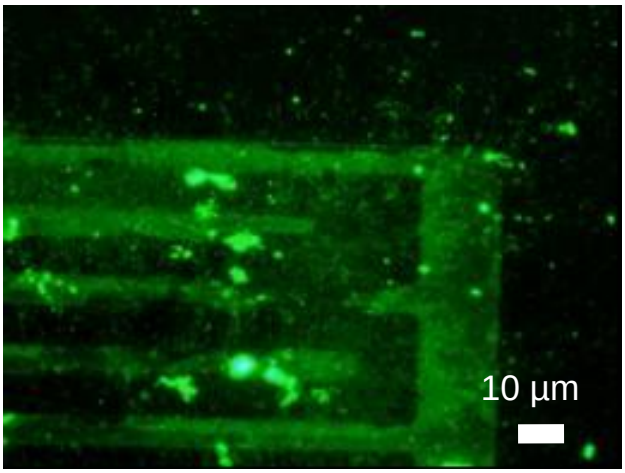

Figure 4-4. Fluorescence image of α-D-mannose glycoconjugates functionalized SWNT-FET device incubated with fluorescently-labeled lectin ConA-Alexa488.

Additionally, the sensitivity of SWNT-FET and CCG-FET devices was investigated by plotting the G *vs* V_g for β-D-galactose functionalized device (control measurements with 10 µM ConA) for varying concentration (2 nM to 10 µM) of specific lectin PA-IL (Figure-S 4-6). The response of both types of devices to 10 µM specific lectin PA-IL is almost two times higher than the response to 10 µM non-specific lectin ConA, which demonstrates good selectivity. Figure 4-5a, c and e depict the biosensor calibration plot derived from multi-concentration experiments (data from three devices) for SWNT/**1a**, CCG/**1a** and CCG/**1c**, respectively. The detection ability of the devices was also tested in the mixed sample of specific and non-specific lectins. The device showed similar signal compared to the pure sample of specific lectin (Figure-S 4-7).

To further understand the kinetics of the lectin-glycoconjugate interactions and to determine the dissociation constant (K_d) of the interaction, $C_{lectin}/(\Delta G/G_0)$ as a function of C_{lectin} were plotted, where C_{lectin} is the lectin concentration and $\Delta G / G_0$ is the relative change in conductance after lectin attachment (Figure 4-5).[101a,101c] A linear relationship was obtained,

which indicated a Langmuir isotherm adsorption, and the **1a**/PA-IL K_d was calculated for SWNT-FET and CCG-FET as 135 nM and 106 nM, respectively. **1c**/PA-IIL K_d was calculated for CCG-FET as 20 nM. These K_d values were compared with the values obtained by isothermal titration microcalorimetry (ITC) to explore the correlation between surface and solution binding (Table 4-2). The titration of the galactose and fucose pyrene-based conjugate (**1a** and **1c**) by their specific lectins (PA-IL and PA-IIL) followed by ITC (Figure 4-6a and b) indicated the occurrence of two binding events probably due to additional interaction of the pyrene aromatic group with a hydrophobic region on the lectins as previously evidenced for PA-IL.[125] Data treatment was performed using a the two sites model (see Supporting Information), and only values for the carbohydrate binding sites were discussed below.

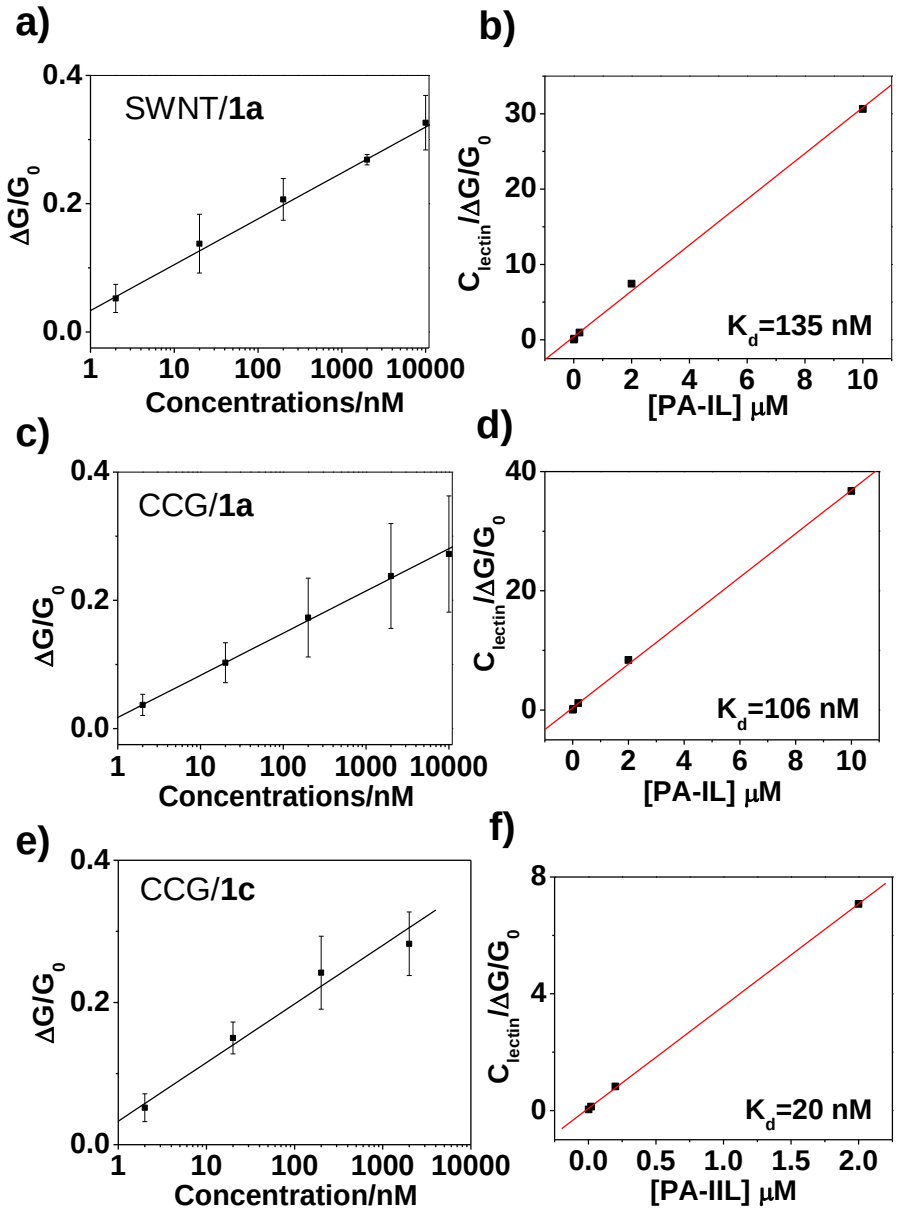

Figure 4-5. Biosensor calibration plot: normalized change in the device conductance (V_g = –0.5 V) *versus* PA-IL concentration of (a) SWNT-FET and (c, e) CCG-FET (data from three devices). Langmuir isotherm of (b) SWNT-FET data presented in panel (a), (d) for CCG-FET with their corresponding calculated lectin dissociation constants (K_d). (f) Langmuir isotherm of CCG/1c and PA-IIL interaction, with calculated lectin dissociation constant K_d.

Table 4-2. Comparison of K_d values obtained by FET and ITC methods

[a] K_d value for the carbohydrate binding site

Glycoconjugate	Lectin	FET		ITC
		SWNT	CCG	
1a/2a	PA-IL	135 nM /147.7 nM	106 nM	100 μM[a] /133 nM
1c	PA-IIL		20 nM	50 nM[a]

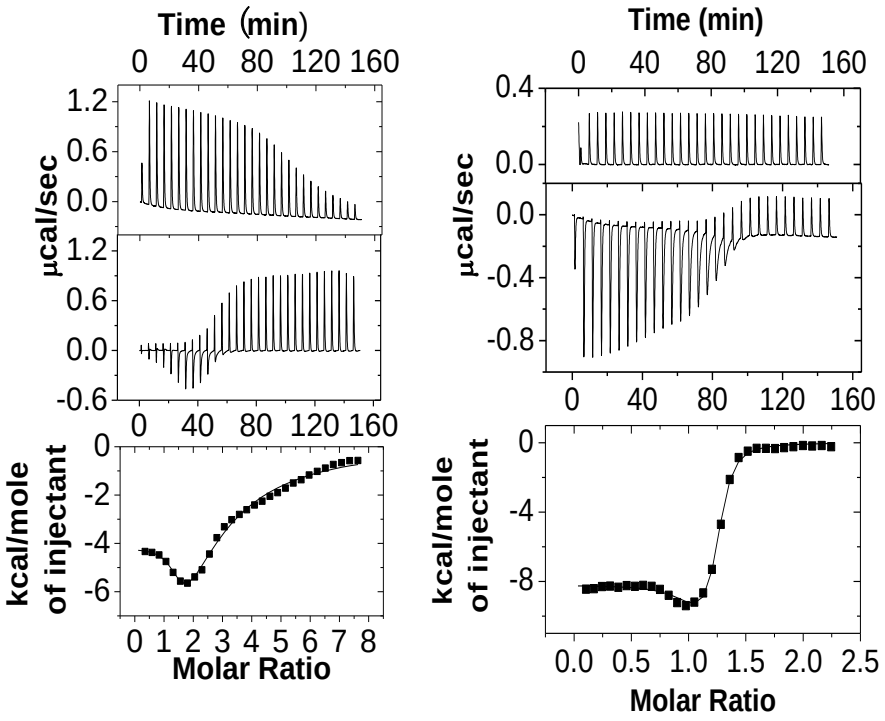

Figure 4-6. Titration of (a) PA-IL (0.05 mM) by compound 1a (1.7 mM) and (b) titration of PA-IIL (0.05 mM) by compound 1c (0.5 mM). Top: control (injection of glycocompound in buffer), middle: titration of lectin, bottom: integration of peaks with a fitting curve obtained from a two site model.

For PA-IL interacting with the galactose pyrene-based conjugate **1a**, the binding event in the galactose binding site had a dissociation constant of 0.1 mM, which was in agreement with data obtained on PA-IL/galactosides,[116a] but is much weaker than the K_d of 106 nM and 135 nM obtained by FET measurement, when glycoconjugate **1a** is attached to CCG or SWNT, respectively (Figure 4-5b and d). This result was likely due to the chelating effect that has been evidenced for PA-IL binding to multivalent glycoconjugates with a two to three orders of magnitude increase in affinity between monovalent ligands and multivalent ones.[116a,120,126] Binding of PA-IL to glyconjugates on surfaces or membranes has also been demonstrated to be much more efficient than to monovalent compounds in solution.[127] The data obtained from the ITC experment on porphyrin **2a**/PA-IL were in the range of 100 nM for both the solution and FET experiments, in agreement with the chelating effect since compound 2a is tetravalent.

For PA-IIL interacting with fucose pyrene-based conjugate **1c**, a dissociation constant (K_d) of 50 nM was obtained for the fucose binding site, which was stronger than the one measured for methyl α-L-fucoside (430 nM).[128] The K_d value of **1c**/PA-IIL measured by FET experiment in Figure 4-5f was calculated as 20 nM and was consistent with the above mentioned K_d value. No chelating effect has been observed for **1c**/PA-IIL binding.

ITC demonstrated that the carbohydrate moiety of the pyrene glycoconjugate is efficiently recognized by the corresponding lectin. The additional interaction of pyrene and the hydrophobic regions of the lectin occurs only in solution; therefore, this was not an issue in the FET experiment, where the pyrene moiety was stacked on the graphitic surface of either SWNT or CCG and not accessible for binding. Moreover, the K_d values obtained by ITC and FET are well correlated, which provided evidence of the effectiveness of carbon nanomaterial-based FET systems to detect carbohydrate-lectin interactions.

4.5 CONCLUSIONS

In conclusion, we have demonstrated the detection of interactions between glycoconjugates and bacterial lectins using SWNT-FET and CCG-FET devices functionalized with two receptor molecules, namely porphyrin and pyrene-based glycoconjugates. The interactions between lectins and glycoconjugates were transduced as conductance changes measured by SWNT-FET and CCG-FET devices. SWNT-FET showed larger response and better selectivity than CCG-FET, and we propose that this difference was the result of 1D and 2D structural difference between the two materials as well as more favorable lectin binding to sugar moieties attached to SWNT surface. Because this nano-electronic detection platform has the potential to be employed for the rapid identification of bacterium in samples consisting of water systems, soils, or human specimens, this technology upon further development may aid in preventing disease outbreaks and preserving public health.

4.6 ACKNOWLEDGEMENT

Y.C acknowledges a graduate student fellowship through Bayer MaterialScience. G. P. K. acknowledges an EPA STAR Graduate Fellowship FP-91713801. The authors thank the Université Claude Bernard Lyon 1 and the CNRS for financial support. S.C. thanks the Région Rhône-Alpes (Cluster de Recherche Chimie) and the CNRS (Programme Interdisciplinaire: Chimie pour le Développement Durable) for additional funding. Dr F. Albrieux, C. Duchamp and N. Henriques are gratefully acknowledged for mass spectrometry analyses. Financial help is

acknowledged from Vaincre la Mucoviscidose and GDR Pseudomonas. A.I. acknowledges funding from ANR Glycoasterix.

4.7 SUPPORTING INFORMATION

Experimental details of UV-vis-NIR spectroscopy and AFM imaging, FET experiment of CCG and lectin interaction, UV-vis-NIR spectroscopy, AFM and fluorescence microscopy imaging, FET experiments of CCG and SWNT with pyrene-glycoconjugates functionalization, titration experiment of CCG and SWNTs with pyrene-glycoconjugates functionalization, FET experiments of CCG with porphyrin-glycoconjugates functionalization, Langmuir isotherm of CCG FET and SWNT FET data, experimental details for treatment of ITC data, and characterizations of glycoconjugates **1a-c** by 1D and 2D NMR and high-resolution mass spectrometry were included in the Supporting Information.

Ultraviolet-visible-near infrared (UV-vis-NIR) absorption spectroscopy of carbon nanomaterial thin films: UV-vis-NIR absorption spectra were obtained using Perkin-Elmer Lambda 900 UV-vis-NIR spectrophotometer. Samples were prepared by spray-casting CCG or SWNT (in DMF suspension) onto quartz plate (1″ ×1″) at 185°C using a commercial air gun (Iwata, Inc.). Glycoconjugate functionalization was performed by incubating the quartz plate in 20 μM glycoconjugate in DI water solution for 2 hr at room temperature. Interaction with specific lectin was performed by incubating the quartz plate with 2 μM lectin solution (in PBS with 5 μM $CaCl_2$) and subsequent washing with PBS solution and drying in ambient for 45 min.

AFM imaging: Atomic force microscope (AFM) images were obtained using scanning probe microscope (Veeco Nanoscope II) in a tapping mode configuration. Samples were

prepared by spin-coating bare SWNTs onto a poly-L-lysine treated freshly cleaved sheet of mica substrate. The bare SWNTs and CCG images were taken after 45 min of drying in ambient. Glycoconjugate functionalization was performed by incubating the SWNTs or CCG deposited mica substrate with 20 μM glycoconjugate in DI water solution for 2 hr at room temperature. Images of functionalized SWNTs and CCG were taken after washing the substrate with DI water and drying in ambient for 45 min. Interaction with specific lectin was investigated by incubating the treated substrate with 2 μM lectin solution (in PBS with 5 μM $CaCl_2$) and subsequent washing with PBS solution and drying in ambient for 45 min.

Fluorescence microscope imaging: Fluorescence microscopy was performed using Olympus (BX 63). Lectins, *Canavalia ensiformis* agglutinin (ConA) conjugated with Alexa Fluor 488 (ConA-Alexa488), were obtained from Invitrogen. In a typical experiment, a 1 mL solution of lectin-Alexa488 conjugates (300 μg / mL) in PBS buffer containing 5 μM Ca^{2+} was added to the suspensions of glycoconjugate coated SWNT-FET devices. The reactions were incubated for 40 min at room temperature in the dark.

Experimental details for isothermal titration microcalorimetry treatment of data: For the interaction between compound 1a and PA-IL, fitting the data with the two sites model was performed while fixing one stoichiometry value to 1.0 (corresponding to known galactose binding site). In this case, the binding event in the galactose binding site has a dissociation constant of 0.1 mM, which was in agreement with data obtained on PA-IL/galactosides. The other binding event displayed a stoichiometry close to 1.5 with dissociation constant of 10 μM thereby indicating the strong affinity of PA-IL for the pyrene group. Aggregation occurred at the end of the titration, confirming that the ligand has two binding epitopes and is therefore able to cluster the tetrameric lectin.

For the interaction between compound 1c and PA-IIL, the stoichiometry of the first binding event between the fucose residue and the fucose-binding pocket of PA-IIL was set to 0.95. A dissociation constant (K_d) of 50 nM is obtained. The dissociation constant for the secondary binding site that was related to the interaction of pyrene with PA-IIL was then evaluated to 50 μM with a stoichiometry of 0.2 (i.e. one pyrene moiety per PA-IIL tetramer). Aggregation of the protein was clearly observed at the end of the titration experiment, which indicates that the monovalent carbohydrate ligand 1c interacts with a lectin that possesses two distinct moieties (i.e. fucose and pyrene groups).

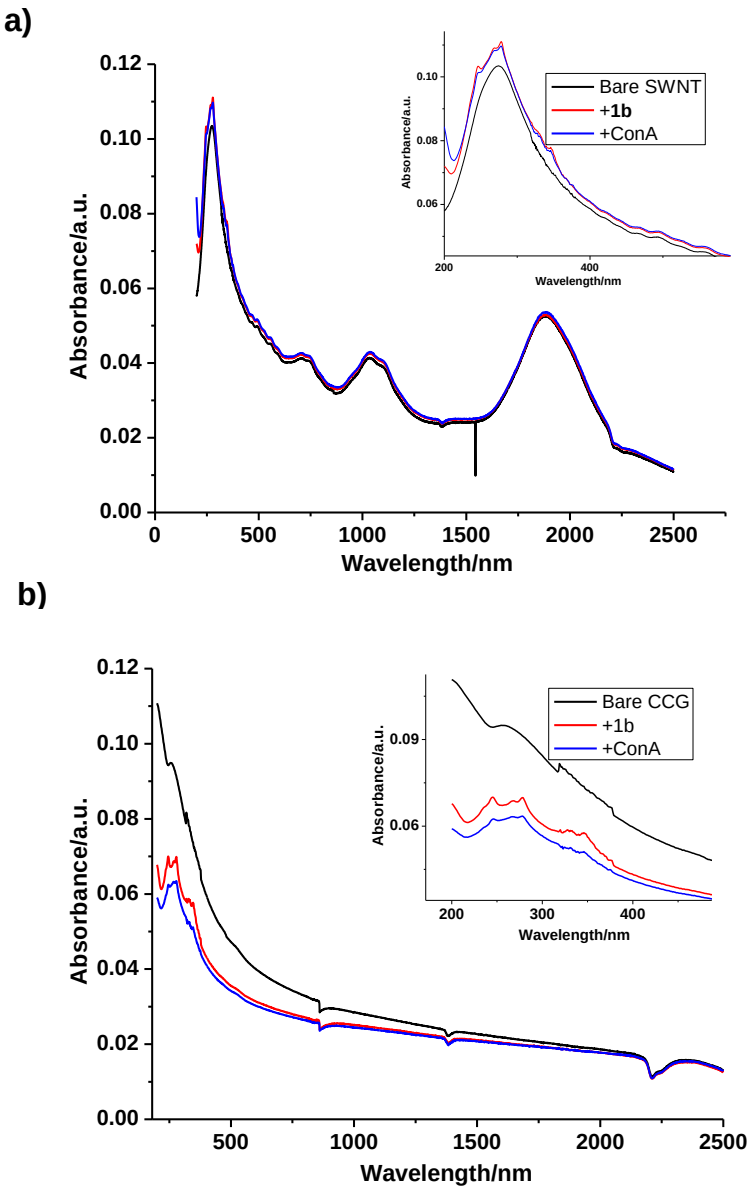

Figure-S 4-1. (a) UV-vis-NIR spectra of bare SWNT (black), SWNT functionalized with 1b (red) and after interaction with ConA (blue). (b) UV-vis-NIR spectra of bare CCG (black), CCG functionalized with 1b (red) and after interaction with ConA (blue).

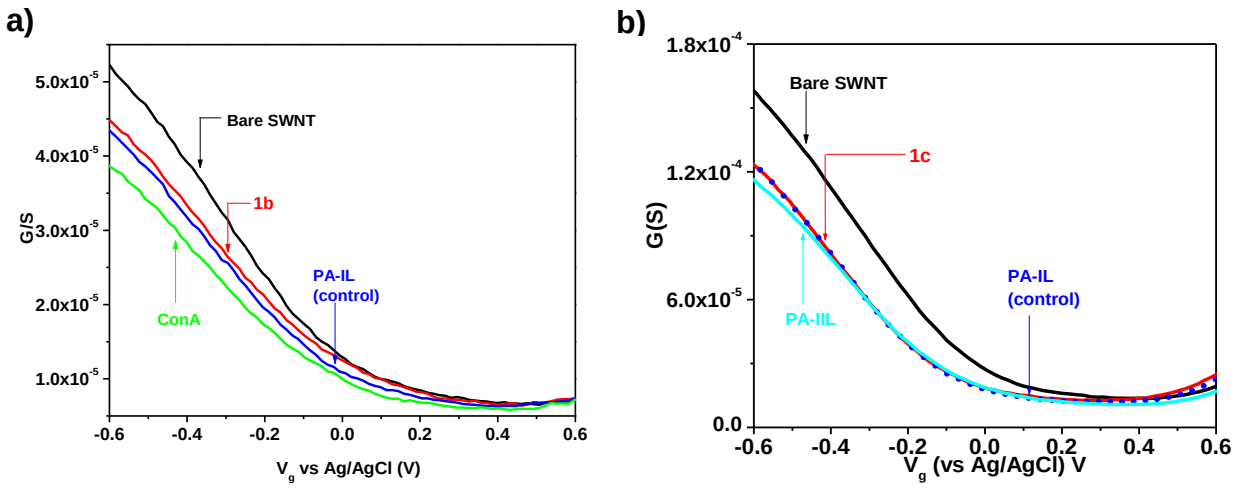

Figure-S 4-2. Nanoelectronic detection of carbohydrate-lectin interactions: Conductance (G) vs gate voltage (Vg) of bare SWNT-FET device, after functionalization with (a) α-D-mannose (1b) and (b) α-L-fucose (1c) pyrene-based glycoconjugates and after attachment with 2 μM control lectin and 2 μM specific lectin (in the presence of 5 μM Ca^{2+}).

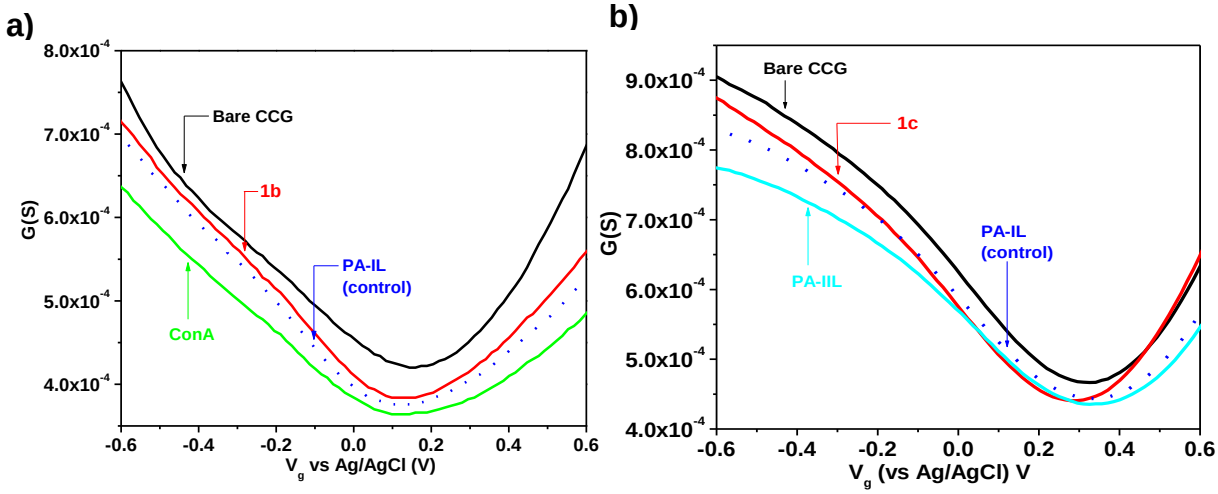

Figure-S 4-3. Nanoelectronic detection of carbohydrate-lectin interactions: Conductance (G) vs gate voltage (Vg) of bare CCG-FET device, after functionalization with (a) α-D-mannose (1b) and (b) α-L-fucose (1c) pyrene-based glycoconjugates and after attachment with 2 μM non-specific (control) lectin and 2 μM specific lectin (in the presence of 5 μM Ca^{2+}).

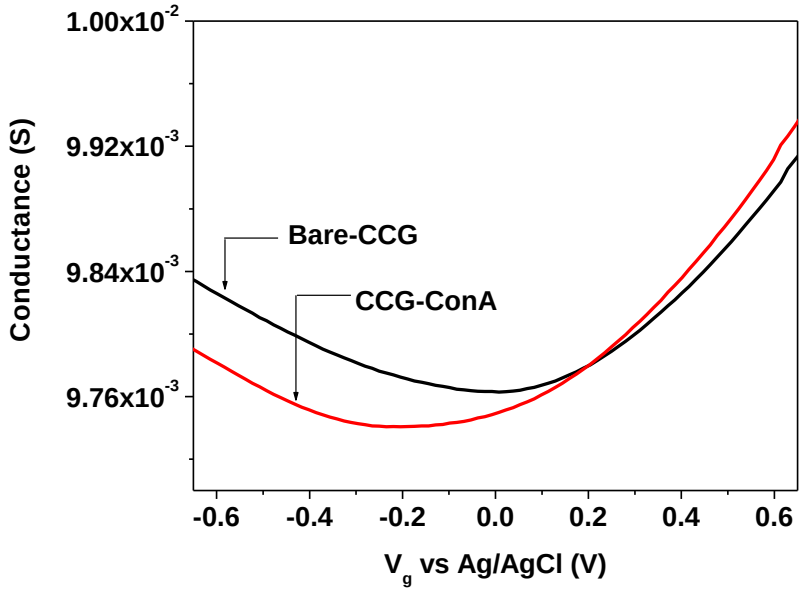

Figure-S 4-4. Control experiment: (G) vs gate voltage (Vg) of bare CCG FET device, after exposure to 2 µM control lectin ConA (in the presence of 5 µM Ca^{2+}).

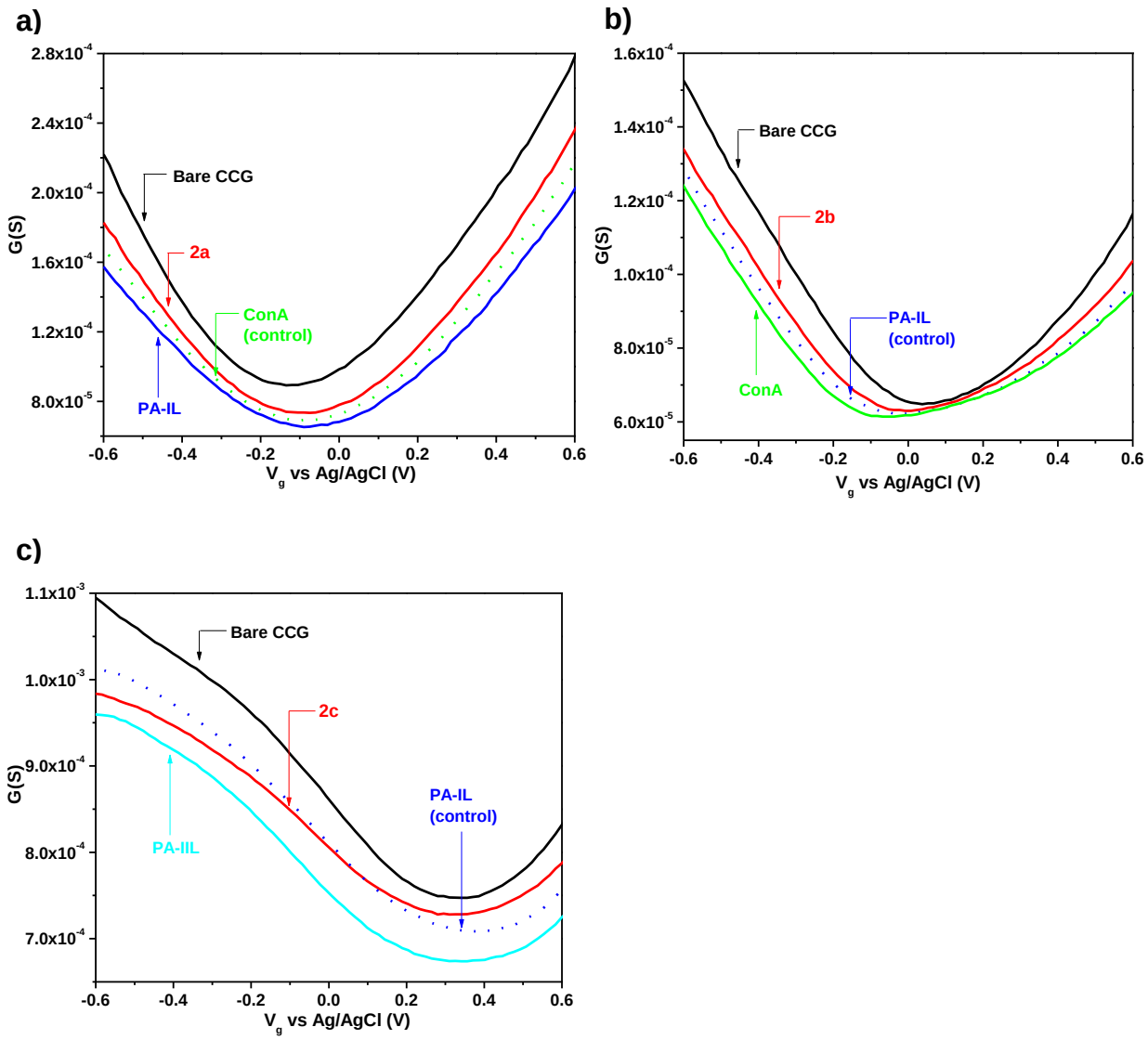

Figure-S 4-5. Nanoelectronic detection of carbohydrate-lectin interactions: Conductance (G) vs gate voltage (Vg) of bare CCG FET device, after functionalization with (a) β-D-galactose (2a), (b) α-D-mannose (2b), and (c) α-L-fucose (2c) porphyrin-based glycoconjugates and after attachment with 2 μM non-specific (control) lectin and 2 μM specific lectin (in the presence of 5 μM Ca^{2+}).

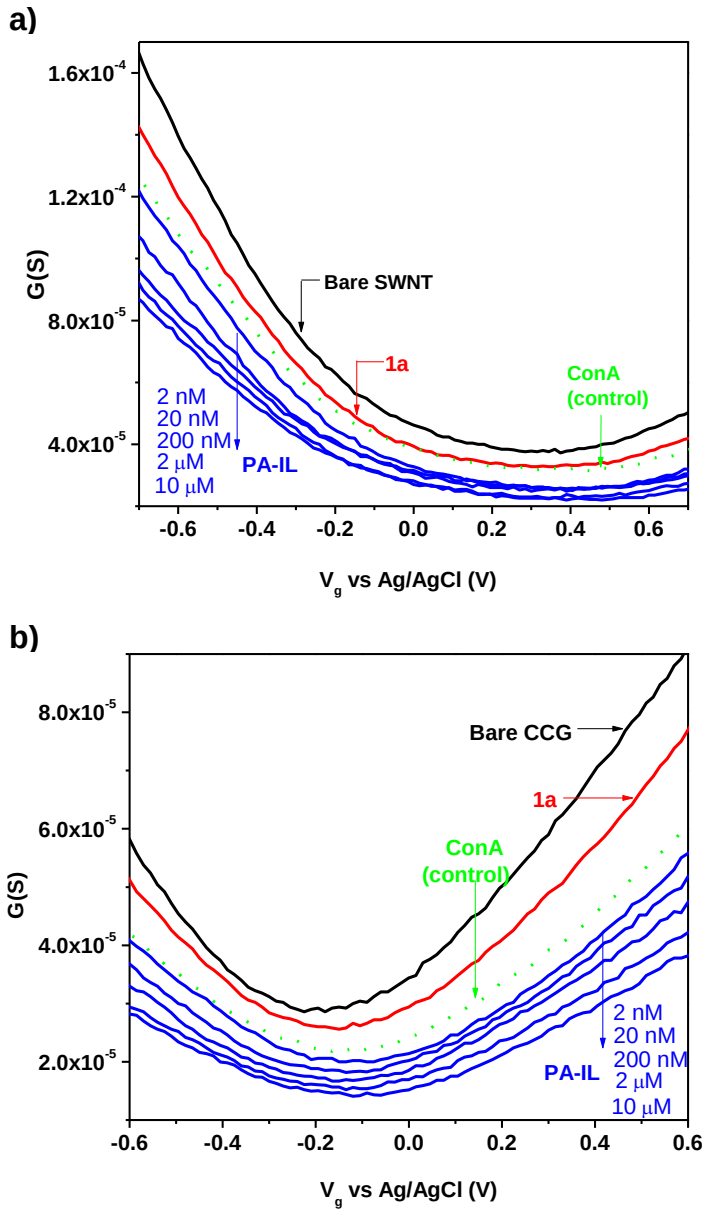

Figure-S 4-6. (a) Same experiment as in Figure 2c with 10 μM ConA as control and varying concentration of the specific lectin (PA-IL) (2 nM-10 μM). (b) Same experiment as in Figure 2c with 10 μM ConA as control and varying concentration of the specific lectin (PA-IL) (2 nM-10 μM).

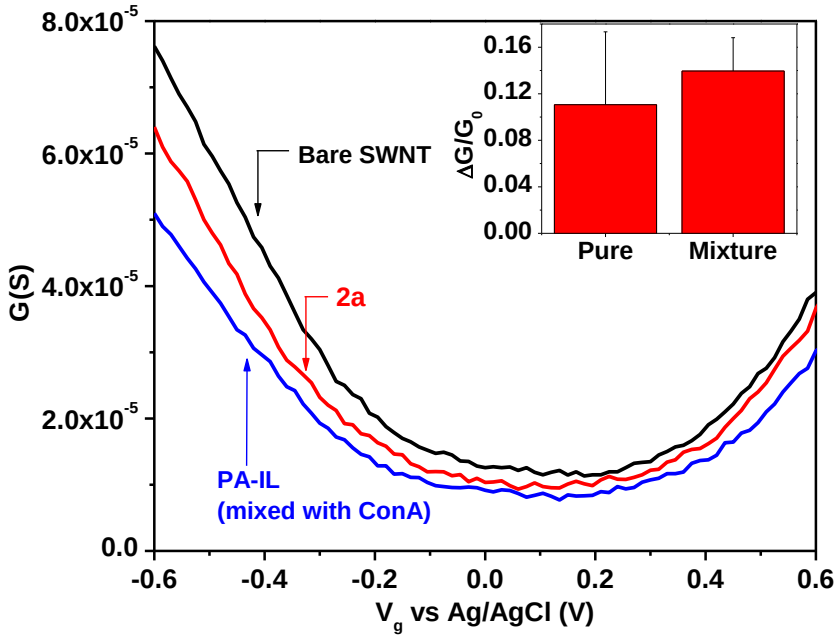

Figure-S 4-7. Nanoelectronic detection of carbohydrate-lectin interactions: Conductance (G) vs gate voltage (Vg) of bare NTFET device, after functionalization with β-D-galactose prophyrin-based glycoconjugate and after incubation with a mixture solution of 2 μM of PA-IL (specific) and 2 μM of ConA (non-specific) (in the presence of 5 μM Ca^{2+}). Inset shows the comparison between the normalized responses to a pure sample of specific lectin and a mixed sample of specific and non-specific lectins.

5.0 CARBON NANOMATERIALS FOR BACTERIA DETECTION

5.1 CHAPTER PREFACE

The aim of this work was to fabricate a bacteria detector using carbon nanomaterials. Antimicrobial peptides were used to functionalize FET devices based on holey reduced graphene oxide (hRGO) and oxidized-SWNTs. These devices exhibited electrical responses to specific bacterial cells. Antimicrobial peptide Magainin I was used in this work as a broad-spectrum probe for gram-negative bacteria, with relatively higher specificity towards *E.coli* O157:H7. The results presented here are still preliminary and more characterizations and some control experiments are still in progress. The results presented in this chapter will be submitted for publication in the near future.

List of Authors: Yanan Chen, Gregg P. Kotchey, and Alexander Star

5.2 INTRODUCTION

Over 70% of the reported foodborne illnesses and food-related deaths in the United States are associated with *Escherichia coli* and *Salmonella*.[129] The current methods for detection of these bacteria mainly include enzyme-linked immunosorbent assay (ELISA) and polymerase chain reaction (PCR).[130] ELISA utilizes the specificity of antibody-antigen interaction; however, antibodies lack the stability for long-term detection. The sensitivity of PCR is extremely high, but it requires the extraction of nucleic acid and is demanding to operate. Researchers are still exploring for a simple-to-use and reliable pathogen detector.

Antimicrobial peptides (AMPs) are part of the host's innate immune system in many organisms and they are considered to serve as the first line of defense against microbial invasion.[131] AMPs recognize target pathogens by interacting with surface components of the cells.[129] The exact mechanism for their antimicrobial activities is still not determined yet.[132] The microbicidal or microbiostatic activity is generally postulated to occur *via* membrane disruption.[129] The binding of AMPs to cell surfaces is reported to be semi-selective. Usually one AMP can bind to multiple microbial species and thus considered a broad-spectrum bacterial probe. The reported examples using AMP for pathogen detection include impedance sensor[130] and fluorescence assays.[129,131] The AMP used in this study, Magainin I (GIGKFLHSAGKFGKAFVGEIMKS), binds most selectively to *E.coli* O157:H7, but also show bioactivity towards other gram-negative bacteria, which comprised the majority of pathogenic infections. [190]

SWNTs and graphene, because of their nanometer-scale sizes and unique electronic properties, are considered to be ideal materials for biosensing application. SWNTs have been reported to be functionalized with antibodies and used in FET biosensors for fast detection of

Salmonella Infantis.[133] An electrochemical sensor using SWNT-aptamer composite for bacteria detection was reported to exhibit ultra-low detection limit.[134] Graphene FETs were decorated with antibody or AMP for the electronic detection of E. coli.[135] Recently, our group explored the synthesis and applications of a new graphene derivative, holey reduced graphene oxide (hRGO). hRGO can be visualized as interconnected graphene nanoribbons; this material exhibited p-type semiconducting behavior and was demonstrated to be sensitive to H_2 gas upon decoration with Pt nanoparticles.[52] hRGO also has abundant oxygen-containing groups on the surface (especially on the edges of the holes), which allow further chemical functionalization with various detection probes.

Here we utilize the unique electronic property of hRGO, as well as the abundant chemical groups on hRGO surfaces, to fabricate a detection platform for bacterial cells. Commercial samples of oxidized SWNTs were also functionalized with AMPs for detection of bacterial cells; however, they didn't exhibit satisfactory response towards the bacteria cells. The data reported here are preliminary data, and more experiments are in progress in this project, including control experiments to prove the attachment of peptide moieties to hRGO and tests with live bacteria (in collaboration with another lab).

5.3 EXPERIMENTAL

Materials. Antimicrobial peptide Magainin I was procured from AnaSpec. The stock solution of AMP was prepared by dispersing the lyophilized product in phosphate buffer saline (PBS) (Fisher Scientific). Heat-killed bacteria cells of *E. coli* O157:H7, *Salmonella typhimurium*, and *Listeria* were obtained from KPL. The heat-killed bacterial cells were rehydrated in 50%

glycerol and diluted by PBS, according to the manufacturer recommendations. P3-SWNTs were procured from Carbon Solution, Inc. This material was purified from as prepared AP-SWNT with nitric acid and left in highly functionalized form. This material contains 1.0-3.0 atomic% carboxylic acid groups which can be derivatitized with a variety of functional groups (specifications were provided by the manufacturer).

Holey reduced graphene oxide (hRGO) was prepared following the published procedure.[22] Briefly, a sample of graphene oxide was subjected to 8 days of HRP/H_2O_2 oxidation in PBS to produce holey graphene oxide. A mixture containing 5.0 mL of 0.125 wt% holey graphene oxide, 4.8 mL of double distilled water, 200 μL of hydrazine hydrate (50 wt%) and 35 μL of NH_4OH (28 wt%) was stirred for 5 min and heated at 95 ℃ for 1 h. The suspension containing hRGO was subsequently dialyzed against distilled water with 0.5% NH_4OH to remove hydrazine.

FET Measurements. Metal interdigitated devices (Au/Ti, 100 nm/30 nm) with an interelectrode spacing of 10 μm were patterned on Si/SiO_2 substrate using photolithography. hRGO was deposited onto each interdigitated microelectrode pattern by ac dielectrophoresis (DEP) method from a suspension in water (Angilent 33250A waveform generator, with an applied ac frequency (300 kHz), bias voltage (10 Vpp), bias duration (60 s)). P3-SWNT was deposited onto the device by DEP method from a suspension in DMF (Angilent 33250A waveform generator, with an applied ac frequency (10 MHz), bias voltage (8 Vpp), bias duration (30 s)).

The electrical performance of each device was investigated using an electrolyte-gated FET device configuration. PBS was used as electrolyte and was placed in a small fluid chamber over the FET device. Two Keithley 2400 source meters were used for FET measurements. An

Ag/AgCl (3 M KCl) reference electrode was used to apply liquid gate potential (-0.75 V to +0.75 V, with respect to the grounded drain electrode). The source-drain current was measured at a constant source-drain voltage (50 mV). Transfer characteristics of each device were measured (conductance (G) *versus* gate voltage (V_g)).

The transfer characteristics of bare FETs were first measured before further functionalization. AMP functionalization was performed by covalent method. The oxygen-containing functional groups on the deposited hRGO or P3-SWNTs were first activated using a solution of 100 nmol of EDC and 25 nmol of NHS in a 50 mM MES buffer (pH 5.5) for 30 minutes.[134] The transfer characteristics of FETs were measured at this point to monitor the change due to AMP functionalization. The FET devices were then soaked overnight with 1 mL of 2 μM AMP solution in PBS (pH 7) overnite. After the overnight incubation with AMP solution, the devices were thoroughly washed with PBS to remove any loosely bond AMPs and their transfer characteristics were measured. Tween 20 (0.1%) in PBS solution was used as blocking buffer to prevent non-specific binding. The bacterial cells solutions were prepared according to the dilution guide provided by the manufacturer. After testing the devices, the devices were incubated with bacterial cell solutions for 1 hr before testing.

Imaging. Scanning electron microscopy (SEM) of the devices was performed on a Philips XL30 FEG microscope at an accelerating voltage of 10 keV to monitor the attachment of bacterial cells to the device surfaces. Atomic force microscope (AFM) images were obtained using scanning probe microscope (Veeco Nanoscope II) in a tapping mode configuration. hRGO was spin-coated onto a poly-L-lysine treated freshly cleaved sheet of mica substrate. The image of bare hRGO was taken after 45 min of drying in ambient. AMP functionalization and *E.coli* O157:H7 incubation was done following the same procedure as in FET functionalization. After

bacterial cells incubation, the mica surface was washed three times with PBS and allowed to dry under ambient for 45 min before the image was taken.

5.4 RESULTS AND DISCUSSION

Figure 5-1 shows schematic illustration of the AMP functionalized hRGO FET for bacteria detection. Briefly, hRGO was deposited between the interdigitated electrodes on each device using DEP method. AMP Magainin I was attached to the hRGO through covalent functionalization (see experimental section). Maigainin I is known to exhibit specificity toward gram-negative bacterial cells.

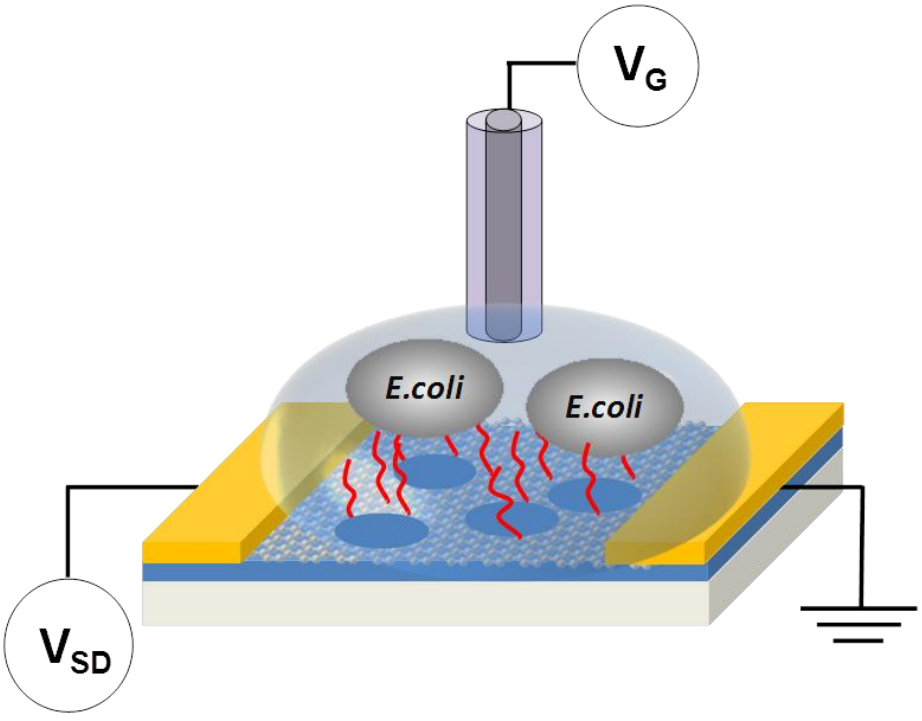

Figure 5-1. Schematic illustration of AMP functionalized hRGO-FET for selective detection of bacterial cells.

The transfer characteristics of bare hRGO FET were first measured. In the measurement, source-drain conductance was plotted as a function of applied gate voltage in the range of -0.75 V to +0.75 V. As reported previously,[22,52] hRGO exhibited p-type semiconducting behavior. In our devices, they showed slightly ambipolar characteristics (Figure 5-2, a). It was observed that the response mainly occurred in the p-type region (negative gate voltage region). The p-type behavior of hRGO can be attributed mainly to the presence of holes in the basal plane, which resulted in a highly interconnected network of graphene nanoribbons.[52]

After covalent attachment of AMP, a decrease in the FET device conductance and a slight negative shift in gate voltages were observed primarily at the negative gate voltages, indicating the functionalization with AMP (Figure 5-2, a and b, red). After incubating with blocking buffer (0.1% Tween 20), there was a further decrease in the p-type region (Figure 5-2, a and b, blue). This decrease indicated that the nonspecific binding spots were blocked by the buffer. Upon exposure to solutions with specific bacterial cells (10^7 cfu/mL bacterial cells solutions in PBS), the devices showed a large response in the p-type region. It is proposed that this response is due to the specific interaction between the attached AMP and the bacterial cells in solution. Presumably, the interaction induced electron transfer which decreased the conductivity of the hRGO material by depleting the main carriers (holes) and caused the change in the device conductance.

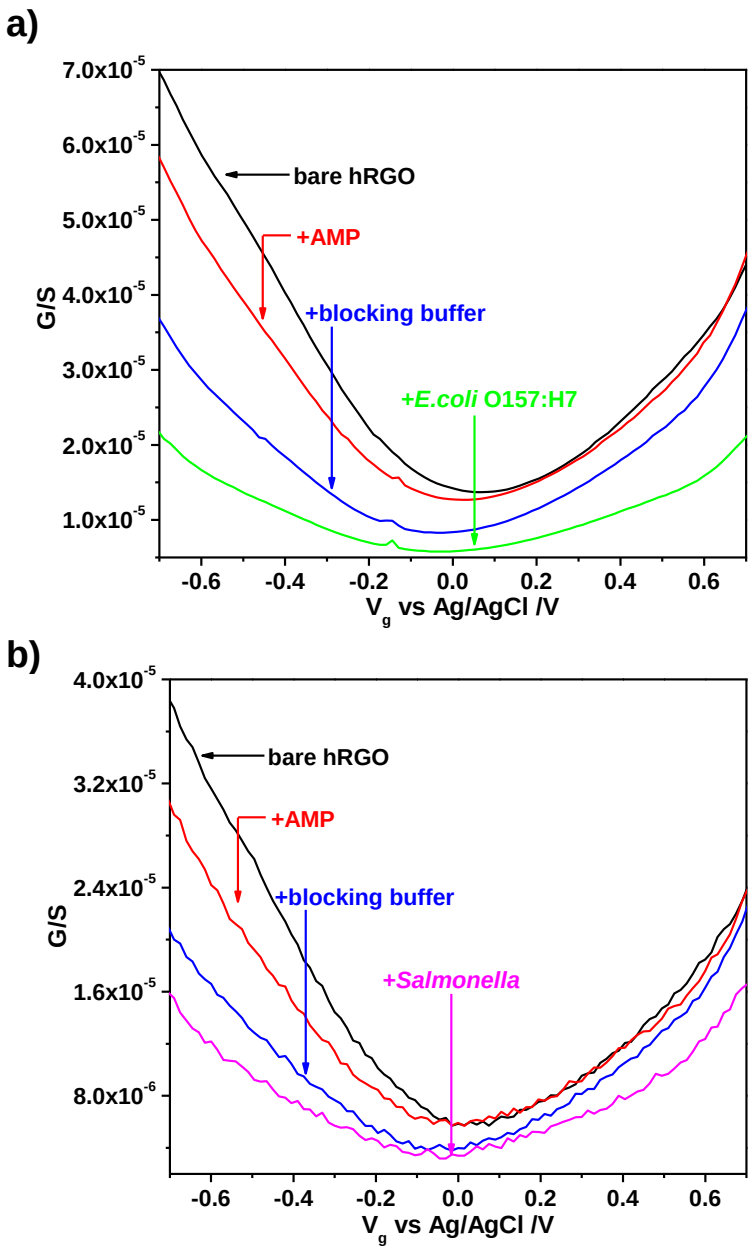

Figure 5-2. Electronic detection of bacteria-AMP interactions. Conductance (G) vs gate voltage (V_g) of bare hRGO FET device, after functionalization with AMP, after incubation with blocking buffer and after incubation with (a) 10^7 cfu/mL *E. coli* O157:H7 and (b) 10^7 cfu/mL *Salmonella typhimurium.*

As a control experiment, we also tested the functionalized devices with nonspecific bacterial cells. It can be seen from Figure 5-3a that after incubation with nonspecific bacterial cells (*Listeria*), the transfer characteristic changed very slightly, indicating little or no binding between AMP and the bacterial cells. *Listeria* bacterial cells are gram-positive, thus showed no specific interaction with AMP Magainin I. We also tested a common biological interference, bovine serum albumin (BSA), to see if there is any non-specific binding that may affect the detection. The device showed very little response to BSA (Figure 5-3b).

Figure 5-4 summarizes the responses of all tested devices. We plotted the responses at negative gate voltages (V_g=-0.5V) since the maximum responses occurred in the negative gate voltage region. The response of each sample was averaged from four devices. It can be seen from the summary that the devices exhibited very small responses to the negative control samples, showing good selectivity. For specific samples, the response to *E.coli* O157:H7 was larger than the response to *Listeria*. This may be the result of the difference in the surface properties of the two bacterial cells and is consistent with previous report. [129]

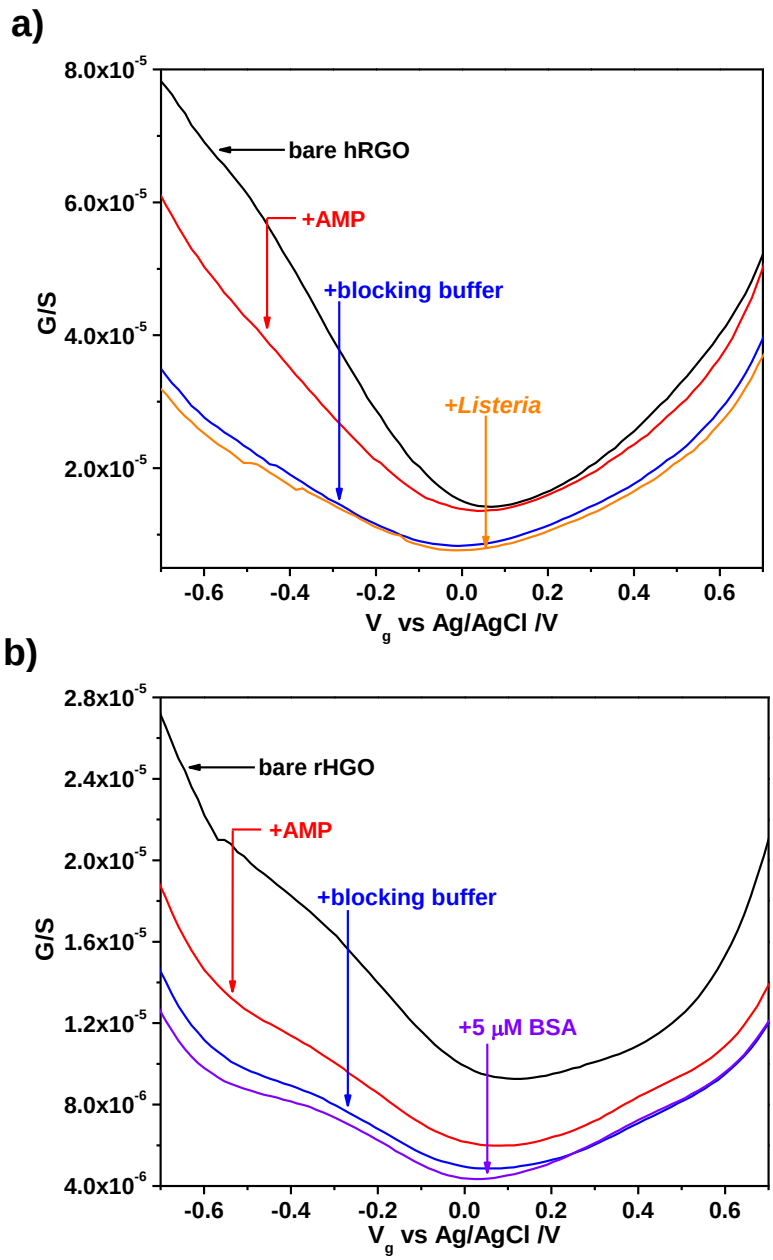

Figure 5-3. Control experiment with nonspecific bacteria. Conductance (G) vs gate voltage (V_g) of bare hRGO FET device, after functionalization with AMP, after incubation with blocking buffer and after incubation with (a) 10^7 cfu/mL *Listeria*, (b) 5 μM BSA.

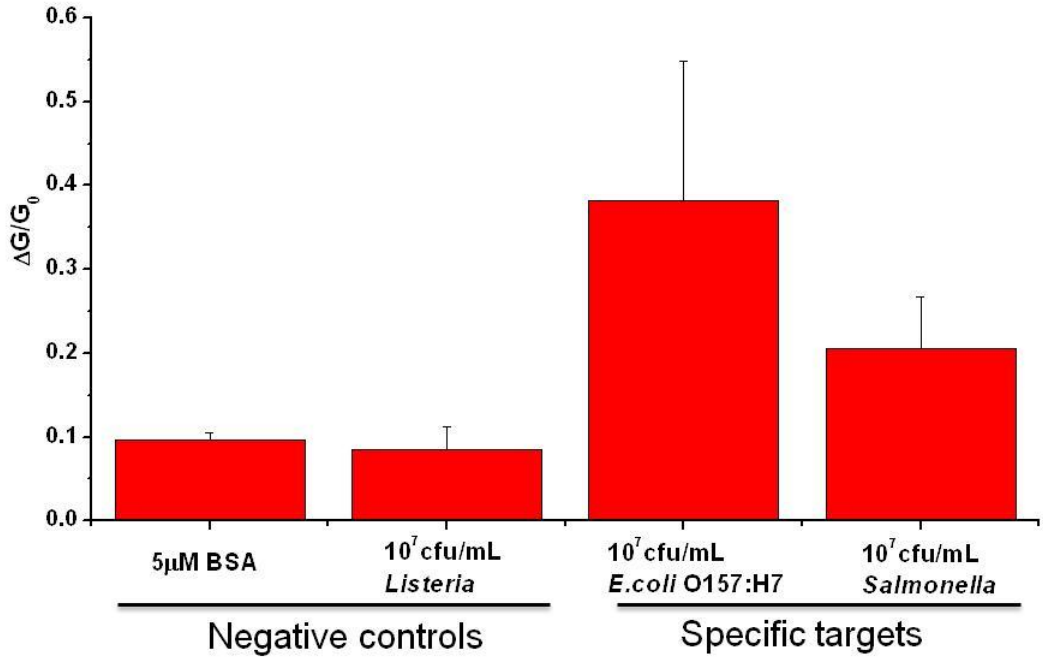

Figure 5-4. Comparison of the normalized responses (V_g=-0.5V) of Magaini I functionalized hRGO FET devices to controls: 10^7 cfu/mL of *Listeria* and 5 μM BSA; and specifics: 10^7 cfu/mL of *E.coli* O157:H7 and *Salmonella*.

Additional control experiments included (1) incubation of bare hRGO with blocking buffer, followed by the exposure to 10^7 cfu/mL *E.coli* O157:H7 (Figure 5-5a), (2) incubation of hRGO devices with AMP solution without EDC/NHS activation, then incubation with blocking buffer and finally exposure to 10^7 cfu/mL *E.coli* O157:H7 (Figure 5-5b). The results were summarized in Figure 5-6. From the summarized results, it can be observed that the hRGO devices functionalized covalently with AMP showed much larger response to *E.coli* O157:H7. These results prove the covalent attachment of AMP to the hRGO device surface.

To visualize the attachment of bacterial cells to the surfaces of the devices, SEM was performed on the FET device used in Figure 5-2a. To increase contrast of the SEM images, a Pd sputter was applied to the surface of the device before the image was taken. It can be observed in the SEM image (Figure 5-7a) that rod-like *E.coli* O157:H7 cells were attached to the surfaces of the devices. This provided a visual proof that the bacterial cells were actually attached to the functionalized hRGO surface, in addition to the measured FET device response. AFM image was also taken showing the attachment of *E.coli* O157:H7 cells to AMP functionalized hRGO surface (Figure 5-7b).

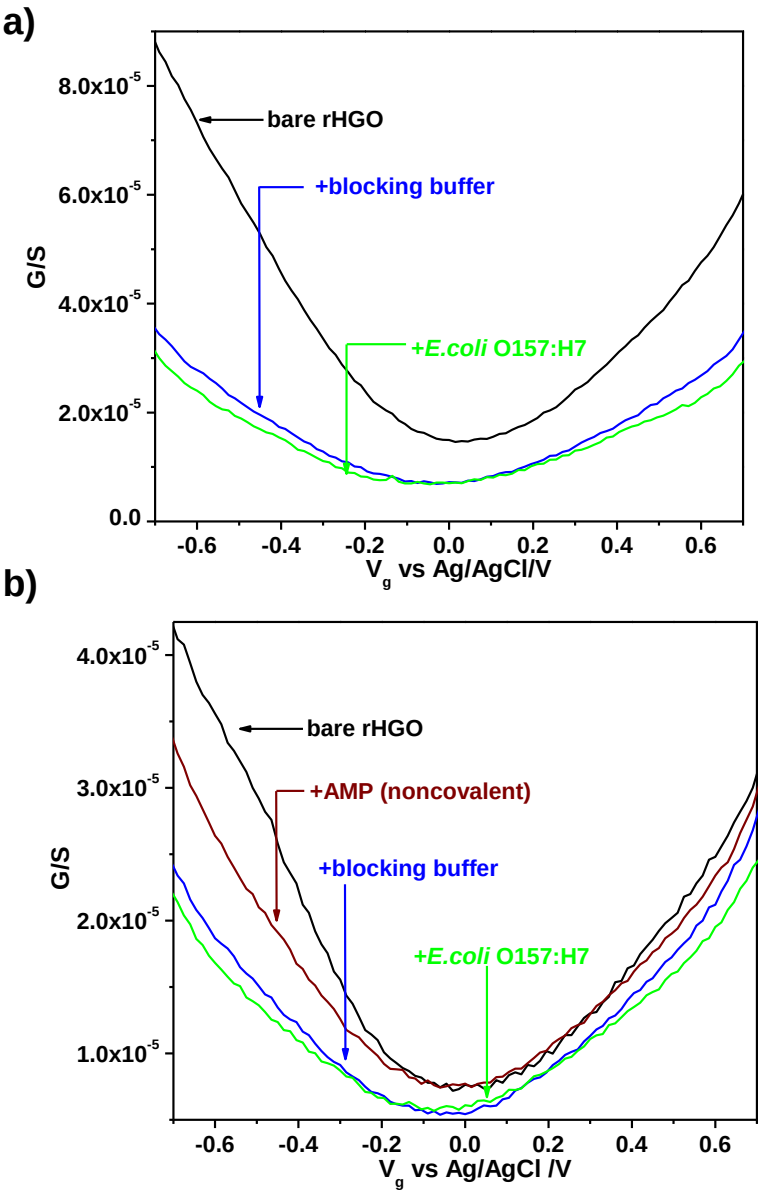

Figure 5-5. Electronic detection, control experiments. Conductance (G) vs gate voltage (V_g) of bare rHGO FET device, (a) after incubation with blocking buffer and after attachment with 10^7 cfu/mL *E. coli* O157:H7 , (b) after incubation with AMP without the carboxylic group activation step, after incubation with blocking buffer and after incubation with 10^7 cfu/mL *E. coli* O157:H7.

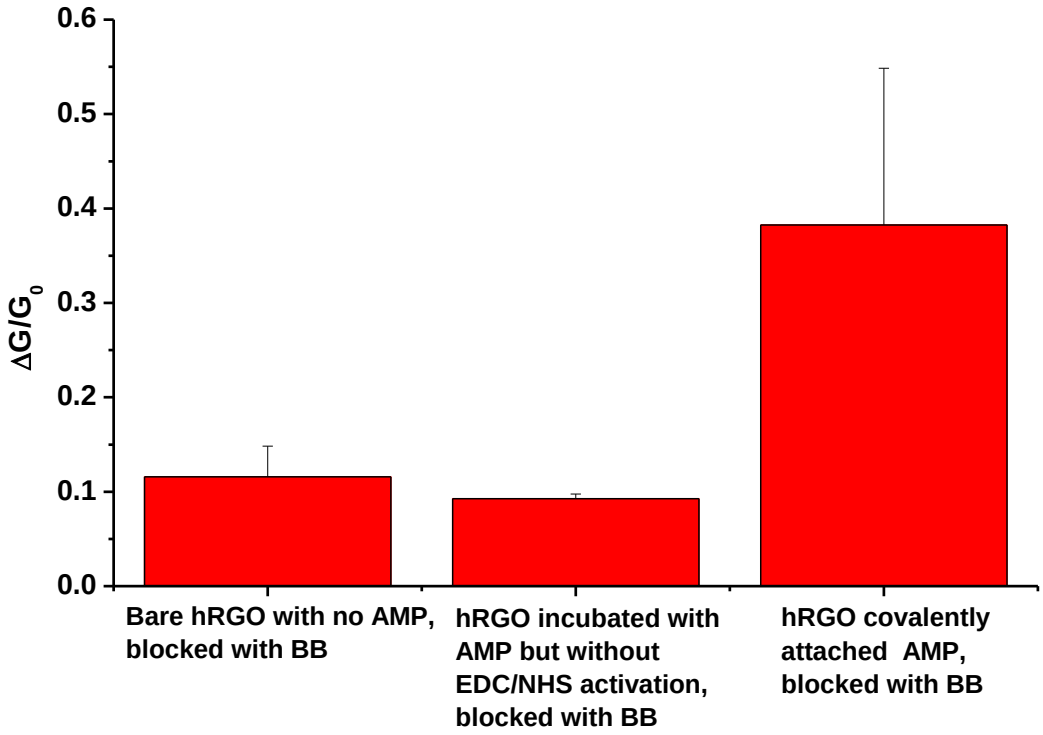

Figure 5-6. Comparison of the normalized responses (V_g=-0.5V) of hRGO FET devices to controls: 10^7 cfu/mL of *E.coli* O157:H7: Bare hRGO FET without AMP functionalization step, hRGO FET incubated with AMP solution overnite without EDC/NHS activation step, hRGO FET functionalized with AMP with EDC/NHS activation.

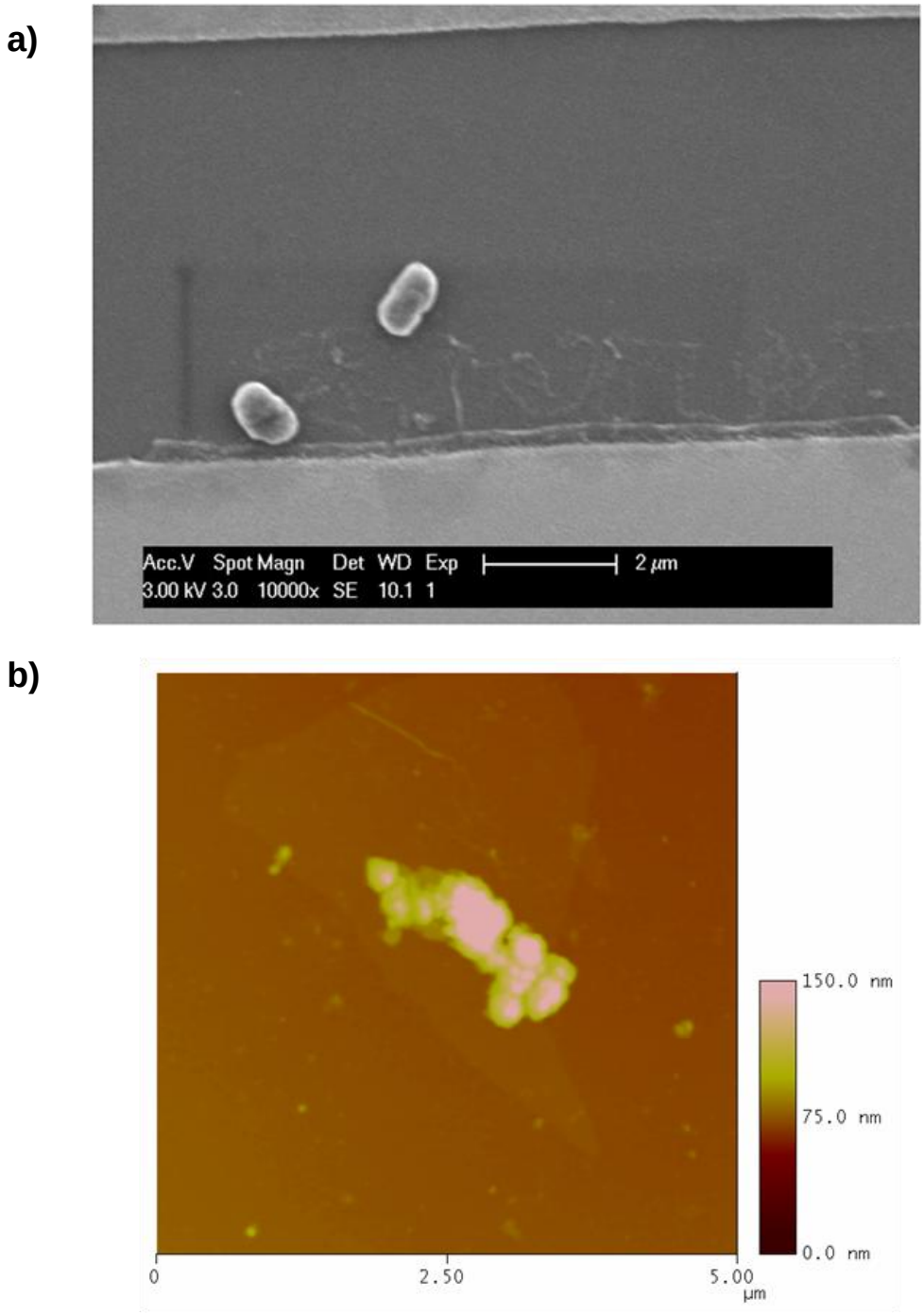

Figure 5-7. (a) SEM image of the functionalized device surface after incubation with *E. coli* O157:H7. (b) AFM image showing the attachment of bacteria to hRGO surface.

Other than hRGO, P3-SWNTs were also tested for the fabrication of bacteria detectors. P3-SWNTs were procured from Carbon Solutions, Inc. According to the manufacturer, this material contains 1.0-3.0 atomic% carboxylic groups. Similar AMP functionalization was done to the P3-SWNT FET devices. Figure 5-8a showed the electrical detection of *E. coli* O157:H7 using an AMP functionalized P3-SWNT FET device. P3-SWNT FET devices showed p-type semiconducting property. After EDC/NHS activation and AMP incubation, the conductance decreased indicating the attachment of AMP to SWNTs surfaces. Blocking buffer incubation induced further decrease in conductance. After incubation with *E. coli* O157:H7, there is a decrease in conductance again as the response to the bacterial cells. However, when compared with hRGO FET devices, the responses from P3-SWNT FET devices were much lower (Figure 5-8b). The reason for the lower response of P3-SWNT FET devices is not clear yet and it is possible that the carboxylic group abundance on P3-SWNTs is not sufficient to achieve high AMP coverage required for bacteria binding.

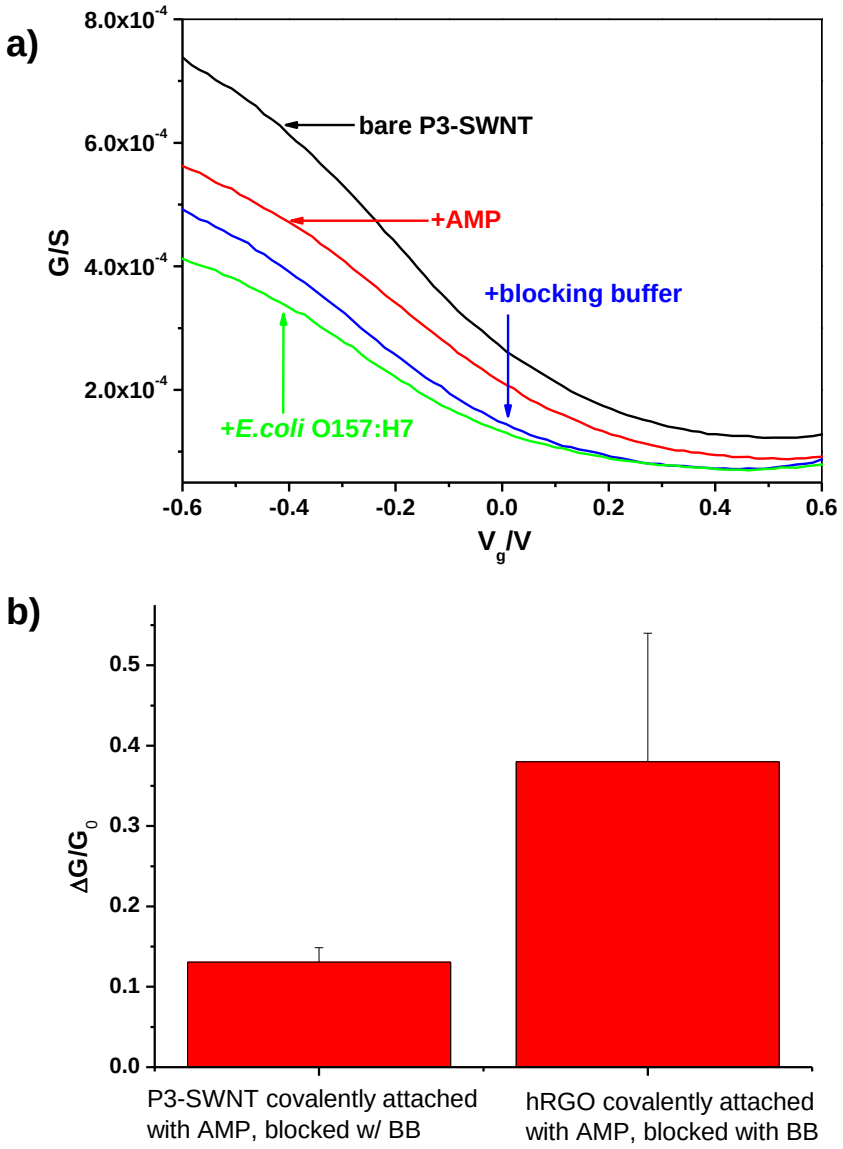

Figure 5-8. (a) Conductance (G) vs gate voltage (V_g) of bare P3-SWNT FET device, after incubation with blocking buffer and after incubation with 10^7 cfu/mL *E. coli* O157:H7, (b) comparison of the normalized responses (V_g=-0.5V) of Magaini I functionalized hRGO FET devices and P3-SWNT FET to specific bacteria: 10^7 cfu/mL of *E.coli* O157:H7.

5.5 CONCLUSIONS

In conclusion, we have demonstrated the detection of gram-negative bacterial cells using hRGO FET and P3-SWNT FET devices functionalized with antimicrobial peptides. The interactions between AMP and gram-negative bacteria were transduced into conductance changes in the FET devices. The preliminary data presented here indicated that hRGO FETs had better response than P3-SWNT FETs. More experiments will be done to directly confirm the attachment of AMP to hRGO and P3-SWNT surfaces. Oxidized P2-SWNT with a higher oxidation level will also be used to fabricate devices, as a comparison with commercially available P3-SWNTs.

6.0 SUMMARY AND FUTURE WORK

Chapters 2-5 presented the research projects I have completed while pursuing Ph. D. degree in Department of Chemistry at the University of Pittsburgh. The projects include studies using carbon nanomaterials for biosensing. I first started by using resistor sensors based on single-walled carbon nanotubes (SWNTs) for the detection of small molecules (hydrogen peroxide). After that, a more complex system involving carbohydrate and lectin molecules was explored with SWNT-based field-effect transistor (FET) devices. Furthermore, we compared SWNT and graphene nanostructures as noncovalently functionalized platform for lectin detection and found that SWNT-FETs exhibited better sensor performance. This study provided some guidelines for researchers who want to find a suitable carbon nanomaterial for sensing applications. Other than noncovalent approaches for carbon nanomaterial functionalization, we covalently functionalized SWNTs and a new graphene derivative, holey reduced graphene oxide (hRGO), and used them for the fabrication of a pathogen detector. These results will guide other researchers in the future development of biosensors based on carbon nanostructures.

For future works, I hope a bacteria detector using SWNT-glycoconjugate system can be built based on the data presented in Chapter 3 and 4. An optimized detector can be incorporated into a microfluidics system for real-time bacteria detection. hRGO is also a promising material for biosensing and I hope more work can be done based on my results in Chapter 5. Hole sizes in

the hRGO material can be tuned to increased the sensing performance. Different antimicrobial peptides can be used to fabricate a sensor array for broad-spectrum bacteria detection and alert.

BIBLIOGRAPHY

(1) Aryal, B. P. Wayne State University, 2008.

(2) Clark, L. C.; Lyons, C. *Ann. N.Y. Acad. Sci.* **1962**, *102*, 29.

(3) Eggins, B. R. *Biosensors: an introduction*; Wiley-Teubner, 1996.

(4) (a) Wang, J. *Chem. Rev.* **2007**, *108*, 814. (b) Allen, B. L.; Kichambare, P. D.; Star, A. *Adv. Mater.* **2007**, *19*, 1439.

(5) Baird, C. L.; Myszka, D. G. *J. Mol. Recognit.* **2001**, *14*, 261.

(6) Ramanathan, K.; Danielsson, B. *Biosens. Bioelectron.* **2001**, *16*, 417.

(7) Bunde, R. L.; Jarvi, E. J.; Rosentreter, J. J. *Talanta* **1998**, *46*, 1223.

(8) Malhotra, B. D.; Chaubey, A. *Sensor. Actuat. B: Chem.* **2003**, *91*, 117.

(9) Terry, L. A.; White, S. F.; Tigwell, L. J. *J. Agric. Food. Chem.* **2005**, *53*, 1309.

(10) Paitan, Y.; Biran, D.; Biran, I.; Shechter, N.; Babai, R.; Rishpon, J.; Ron, E. Z. *Biotechnol. Adv.* **2003**, *22*, 27.

(11) Gooding, J. J. *Anal. Chim. Acta* **2006**, *559*, 137.

(12) (a) Wang, J. *Analyst* **2005**, *130*, 421. (b) Pandey, P.; Datta, M.; Malhotra, B. D. *Anal. Lett.* **2008**, *41*, 159.

(13) Chopra, N.; Gavalas, V. G.; Bachas, L. G.; Hinds, B. J. *Anal. Lett.* **2007**, *40*, 2067.

(14) Радушкевич, Л. В. *Журнал Физической Химии* **1952**, *26*, 88.

(15) Iijima, S. *Nature* **1991**, *354*, 56.

(16) (a) Iijima, S.; Ichihashi, T. *Nature* **1993**, *363*, 603. (b) Bethune, D. S.; Klang, C. H.; de Vries, M. S.; Gorman, G.; Savoy, R.; Vazquez, J.; Beyers, R. *Nature* **1993**, *363*, 605.

(17) http://en.wikipedia.org/wiki/Carbon_nanotube

(18) Odom, T. W.; Huang, J.-L.; Kim, P.; Lieber, C. M. *J. Phys. Chem. B* **2000**, *104*, 2794.

(19) Yang, W. ; Thordarson, P. ; Gooding, J. J.; Ringer, S. P.; Braet, F. *Nanotechnology* **2007**, *18*, 412001.

(20) Novoselov, K. S.; Geim, A. K.; Morozov, S. V.; Jiang, D.; Zhang, Y.; Dubonos, S. V.; Grigorieva, I. V.; Firsov, A. A. *Science* **2004**, *306*, 666.

(21) Geim, A. K.; Novoselov, K. S. *Nat. Mater.* **2007**, *6*, 183.

(22) Kotchey, G. P.; Allen, B. L.; Vedala, H.; Yanamala, N.; Kapralov, A. A.; Tyurina, Y. Y.; Klein-Seetharaman, J.; Kagan, V. E.; Star, A. *ACS Nano* **2011**, *5*, 2098.

(23) Liu, Y.; Dong, X.; Chen, P. *Chem. Soc. Rev.* **2012**, *41*, 2283.

(24) Reina, A.; Jia, X.; Ho, J.; Nezich, D.; Son, H.; Bulovic, V.; Dresselhaus, M. S.; Kong, J. *Nano Lett.* **2008**, *9*, 30.

(25) Shen, H.; Zhang, L.; Liu, M.; Zhang, Z. *Theranostics* **2012**, *2*, 11.

(26) Peng, X.; Wong, S. S. *Adv. Mater.* **2009**, *21*, 625.

(27) Chen, Y.; Star, A.; Vidal, S. *Chem. Soc. Rev.* DOI: 10.1039/C2CS35396B, **2013**.

(28) Ju, S.-Y.; Papadimitrakopoulos, F. *J. Am. Chem. Soc.* **2007**, *130*, 655.

(29) Hong, S. Y.; Tobias, G.; Ballesteros, B.; El Oualid, F.; Errey, J. C.; Doores, K. J.; Kirkland, A. I.; Nellist, P. D.; Green, M. L. H.; Davis, B. G. *J. Am. Chem. Soc.* **2007**, *129*, 10966.

(30) Loh, K. P.; Bao, Q.; Ang, P. K.; Yang, J. *J. Mater. Chem.* **2010**, *20*, 2277.

(31) Dai, H. *Acc. Chem. Res.* **2002**, *35*, 1035.

(32) Liu, Z.; Fan, A. C.; Rakhra, K.; Sherlock, S.; Goodwin, A.; Chen, X.; Yang, Q.; Felsher, D. W.; Dai, H. *Angew. Chem. Int. Ed.* **2009**, *48*, 7668.

(33) Tans, S. J.; Devoret, M. H.; Dai, H.; Thess, A.; Smalley, R. E.; Geerligs, L. J.; Dekker, C. *Nature* **1997**, *386*, 474.

(34) Martel, R.; Schmidt, T.; Shea, H. R.; Hertel, T.; Avouris, P. *Appl. Phys. Lett.* **1998**, *73*, 2447.

(35) Wang, J.; Li, M.; Shi, Z.; Li, N.; Gu, Z. *Anal. Chem.* **2002**, *74*, 1993.

(36) Yu, X.; Chattopadhyay, D.; Galeska, I.; Papadimitrakopoulos, F.; Rusling, J. F. *Electrochem. Commun.* **2003**, *5*, 408.

(37) Anthony, G.-E.; Chenghong, L.; Ray, H. B. *Nanotechnology* **2002**, *13*, 559.

(38) Wang, J.; Liu, G.; Jan, M. R. *J. Am. Chem. Soc.* **2004**, *126*, 3010.

(39) Cherukuri, P.; Bachilo, S. M.; Litovsky, S. H.; Weisman, R. B. *J. Am. Chem. Soc.* **2004**, *126*, 15638.

(40) Chen, Z.; Tabakman, S. M.; Goodwin, A. P.; Kattah, M. G.; Daranciang, D.; Wang, X.; Zhang, G.; Li, X.; Liu, Z.; Utz, P. J.; Jiang, K.; Fan, S.; Dai, H. *Nat. Biotechnol.* **2008**, *26*, 7.

(41) Huang, Y.; Dong, X.; Shi, Y.; Li, C. M.; Li, L.-J.; Chen, P. *Nanoscale* **2010**, *2*, 1485.

(42) Xu, H.; Dai, H.; Chen, G. *Talanta* **2010**, *81*, 334.

(43) Kang, X.; Wang, J.; Wu, H.; Aksay, I. A.; Liu, J.; Lin, Y. *Biosens. Bioelectron.* **2009**, *25*, 901.

(44) Su, B.; Tang, J.; Huang, J.; Yang, H.; Qiu, B.; Chen, G.; Tang, D. *Electroanalysis* **2010**, *22*, 2720.

(45) Wang, Y.; Li, Y.; Tang, L.; Lu, J.; Li, J. *Electrochem. Commun.* **2009**, *11*, 889.

(46) He, S.; Song, B.; Li, D.; Zhu, C.; Qi, W.; Wen, Y.; Wang, L.; Song, S.; Fang, H.; Fan, C. *Adv. Funct. Mater.* **2010**, *20*, 453.

(47) Jung, J. H.; Cheon, D. S.; Liu, F.; Lee, K. B.; Seo, T. S. *Angew. Chem. Int. Ed.* **2010**, *49*, 5708.

(48) Merchant, C. A.; Healy, K.; Wanunu, M.; Ray, V.; Peterman, N.; Bartel, J.; Fischbein, M. D.; Venta, K.; Luo, Z.; Johnson, A. T. C.; Drndić, M. *Nano Lett.* **2010**, *10*, 2915.

(49) Mao, S.; Lu, G.; Yu, K.; Bo, Z.; Chen, J. *Adv. Mater.* **2010**, *22*, 3521.

(50) He, Q.; Wu, S.; Gao, S.; Cao, X.; Yin, Z.; Li, H.; Chen, P.; Zhang, H. *ACS Nano* **2011**, *5*, 5038.

(51) Mohanty, N.; Berry, V. *Nano Lett.* **2008**, *8*, 4469.

(52) Vedala, H.; Sorescu, D. C.; Kotchey, G. P.; Star, A. *Nano Lett.* **2011**, *11*, 2342.

(53) Chen, Y.; Lee, Y. D.; Vedala, H.; Allen, B. L.; Star, A. *ACS Nano* **2010**, *4*, 6854.

(54) (a) Baughman, R. H.; Zakhidov, A. A.; de Heer, W. A. *Science* **2002**, *297*, 787. (b) Avouris, P. *Acc. Chem. Res.* **2002**, *35*, 1026. (c) Kauffman, D. R.; Star, A. *Angew. Chem., Int. Ed.* **2008**, *47*, 6550. (d) Zhao, Q.; Gan, Z.; Zhuang, Q. *Electroanalysis* **2002**, *14*, 1609. (e) Smart, S. K.; Cassady, A. I.; Lu, G. Q.; Martin, D. J. *Carbon* **2006**, *44*, 1034. (f) Balasubramanian, K.; Burghard, M. *Anal. Bioanal. Chem.* **2006**, *385*, 452. (g) Bianco, A.; Kostarelos, K.; Prato, M. *Curr. Opin. Chem. Biol.* **2005**, *9*, 674. (h) Allen, B. L.; Kichambare, P. D.; Star, A. *Adv. Mater.* **2007**, *19*, 1439.

(55) Moore, V. C.; Strano, M. S.; Haroz, E. H.; Hauge, R. H.; Smalley, R. E.; Schmidt, J.; Talmon, Y. *Nano Lett.* **2003**, *3*, 1379.

(56) (a) O'Connell, M. J.; Boul, P.; Ericson, L. M.; Huffman, C.; Wang, Y.; Haroz, E.; Kuper, C.; Tour, J.; Ausman, K. D.; Smalley, R. E. *Chem. Phys. Lett.* **2001**, *342*, 265. (b) Star, A.; Stoddart, J. F.; Steuerman, D.; Diehl, M.; Boukai, A.; Wong, E. W.; Yang, X.; Chung, S. W.; Choi, H.; Heath, J. R. *Angew. Chem., Int. Ed.* **2001**, *40*, 1721.

(57) (a) Zheng, M.; Jagota, A.; Semke, E. D.; Diner, B. A.; McLean, R. S.; Lustig, S. R.; Richardson, R. E.; Tassi, N. G. *Nat. Mater.* **2003**, *2*, 338. (b) Xie, H.; Ortiz-Acevedo, A.; Zorbas, V.; Baughman, R. H.; Draper, R. K.; Musselman, I. H.; Dalton, A. B.; Dieckmann, G. R. *J. Mater. Chem.* **2005**, *15*, 1734. (c) Karajanagi, S. S.; Yang, H.; Asuri, P.; Sellitto, E.; Dordick, J. S.; Kane, R. S. *Langmuir* **2006**, *22*, 1392. (d) Star, A.; Steuerman, D. W.; Heath, J. R.; Stoddart, J. F. *Angew. Chem., Int. Ed.* **2002**, *41*, 2508.

(58) Nakamura, G.; Narimatsu, K.; Niidome, Y.; Nakashima, N. *Chem. Lett.* **2007**, *9*, 1140.

(59) Khan, S. G.; Katiyar, S. K.; Agarwal, R.; Mukhtar, H. *Cancer Res.* **1992**, *52*, 4050.

(60) Chang, C. J.; Chiua, K. L.; Chen, Y. L.; Chang, C. Y. *Food Chem.* **2000**, *68*, 109.

(61) Mochizuki, M.; Yamazaki, S. I.; Kano, K.; Ikeda, T. *Biochim. Biophys. Acta* **2002**, *1569*, 35.

(62) (a) Valcic, S.; Muders, A.; Jacobsen, N. E.; Liebler, D. C.; Timmermann, B. N. *Chem. Res. Toxicol.* **1999**, *12*, 382. (b) Lee, S. R.; Im, K. J.; Suh, S. I.; Jung, J. G. *Phytother. Res.* **2003**, *17*, 206.

(63) (a) Sadzuka, Y.; Sugiyama, T.; Sonobe, T. *Toxicol. Lett.* **2000**, *114*, 155. (b) Annabi, B.; Bouzeghrane, M.; Moumdjian, R.; Moghrabi, A.; Beliveau, R. *J. Neurochem.* **2005**, *94*, 906.

(64) (a) Morré, D. M.; Morré, D. J. *Cancer Lett.* **2006**, *238*, 202. (b) Tachibana, H.; Koga, K.; Fujimura, Y.; Yamada, K. *Nat. Struct. Mol. Biol.* **2004**, *11*, 380.

(65) Weisburger, J. H.; Cardenas, E.; Packer, L. *Handbook of Anitoxidants*, 1996.

(66) Sies, H. *Exp. Physiol.* **1997**, *82*, 291.

(67) Fenton, H. J. H. *J. Chem. Soc.* **1894**, *65*, 899.

(68) Landi, B. J.; Evans, C. M.; Worman, J. J.; Castro, S. L.; Bailey, S. G.; Raffaelle, R. P. *Mater. Lett.* **2006**, *60*, 3502.

(69) Zephyr Software Open Source, http://zyphyr.synopsia.net/

(70) Manatt, S. L.; Manatt, M. R. R. *Chem.—Eur. J.* **2004**, *10*, 6540.

(71) (a) O'Brien, F. E. M. *J. Sci. Instrum.* **1948**, *25*, 73. (b) Greenspan, L. *J. Res. Natl. Bur. Stand.* **1977**, *81*, 89.

(72) (a) Wang, F.; Gu, H.; Swager, T. M. *J. Am. Chem. Soc.* **2008**, *130*, 5392. (b) Star, A.; Han, T. R.; Joshi, V.; Stetter, J. R. *Electroanalysis* **2004**, *16*, 108.

(73) Kim, W.; Javey, A.; Vermesh, O.; Wang, Q.; Li, Y.; Dai, H. *Nano Lett.* **2003**, *3*, 193.

(74) Perron, N. R.; Brumaghim, J. L. *Cell Biochem. Biophys.* **2009**, *53*, 75.

(75) Zhang, Z. B.; Liu, X. J.; Campbell, E. E.; Zhang, S. L. *J. Appl. Phys.* **2005**, *98*, 056103.

(76) Lim, J. H.; Phiboolsirichit, N.; Mubeen, S.; Rheem, Y.; Deshusses, M. A.; Mulchandani, A.; Myung, N. V. *Electroanalysis* **2010**, *22*, 99.

(77) (a) Kondo, K.; Kurihara, M.; Miyata, N.; Suzuki, T.; Toyoda, M. *Arch. Biochem. Biophys.* **1999**, *362*, 79. (b) Yoshioka, H.; Sugiura, K.; Kawahara, R.; Fujita, T.; Makino, M.; Kamiya, M.; Tsuyumu, S. *Agric. Biol. Chem.* **1991**, *55*, 2717. (c) Severino, J. F.; Goodman, B. A.; Kay, C. W. M.; Stolze, K.; Tunega, D.; Reichenauer, T. G.; Pirker, K. F. *Free Radical Biol. Med.* **2009**, *46*, 1076.

(78) Ryan, P.; Hynes, M. J. *J. Inorg. Biochem.* **2007**, *101*, 585.

(79) Zhu, N.; Huang, T. C.; Yu, Y.; LaVoie, E. J.; Yang, C. S.; Ho, C. T. *J. Agric. Food Chem.* **2000**, *48*, 979.

(80) (a) Rosenblatt, S.; Yaish, Y.; Park, J.; Gore, J.; Sazonova, V.; McEuen, P. L. *Nano Lett.* **2002**, *2*, 869. (b) Krüger, M.; Buitelaar, M. R.; Nussbaumer, T.; Schönenberger, C.; Forró, L. *Appl. Phys. Lett.* **2001**, *78*, 1291. (c) Heller, I.; Janssens, A. M.; Männik, J.; Minot, E. D.; Lemay, S. G.; Dekker, C. *Nano Lett.* **2008**, *8*, 591.

(81) Vedala, H.; Chen, Y.; Cecioni, S.; Imberty, A.; Vidal, S.; Star, A. *Nano Lett.* **2010**, *11*, 170.

(82) Lis, H.; Sharon, N. *Chem. Rev.* **1998**, *98*, 637.

(83) (a) Pieters, R. J. *Org. Biomol. Chem.* **2009**, *7*, 2013. (b) Varki, A. *Glycobiology* **1993**, *3*, 97. (c) Dwek, R. A. *Chem. Rev.* **1996**, *96*, 683. (d) Bertozzi, C. R.; Kiessling, L. L. *Science* **2001**, *291*, 2357.

(84) (a) Lundquist, J. J.; Toone, E. J. *Chem. Rev.* **2002**, *102*, 555. (b) Imberty, A.; Varrot, A. *Curr. Opin. Struct. Biol.* **2008**, *18*, 567. (c) Sharon, N. *Biochim. Biophys. Acta* **2006**, *1760*, 527.

(85) Jelinek, R.; Kolusheva, S. *Chem. Rev.* **2004**, *104*, 5987.

(86) (a) Gustavo, A.; Jordi, R.; Ali, D.; Rius, F. *Angew. Chem., Int. Ed.* **2009**, *48*, 7334. (b) Gu, L.; Elkin, T.; Jiang, X.; Li, H.; Lin, Y.; Qu, L.; Tzeng, T. R. J.; Joseph, R.; Sun, Y. P. *Chem. Commun.* **2005**, 874.

(87) Chen, S.; Yuan, R.; Chai, Y.; Min, L.; Li, W.; Xu, Y. *Electrochim. Acta* **2009**, *54*, 7242.

(88) (a) Bahr, J.; Tour, J. *J. Mater. Chem.* **2002**, *12*, 1952. (b) Dyke, C. A.; Tour, J. M. *J. Phys. Chem. A* **2004**, *108*, 11151. (c) Tasis, D.; Tagmatarchis, N.; Bianco, A.; Prato, M. *Chem. Rev.* **2006**, *106*, 1105.

(89) (a) Wu, P.; Chen, X.; Hu, N.; Tam, U. C.; Blixt, O.; Zettl, A.; Bertozzi, C. R. *Angew. Chem., Int. Ed.* **2008**, *47*, 5022. (b) Assali, M.; Leal, M. P.; Fernandez, I.; Baati, R.; Mioskowski, C.; Khiar, N. *Soft Matter* **2009**, *5*, 948. (c) Haddad, R.; Cosnier, S.; Maaref, A.; Holzinger, M. *Analyst* **2009**, *134*, 2412. (d) Khiar, N.; Leal, M. P.; Baati, R.; Ruhlmann, C.; Mioskowski, C.; Schultz, P.; Fernandez, I. *Chem. Commun.* **2009**, *27*, 4121.

(90) (a) Hasegawa, T.; Fujisawa, T.; Numata, M.; Umeda, M.; Matsumoto, T.; Kimura, T.; Okumura, S.; Sakurai, K.; Shinkai, S. *Chem. Commun.* **2004**, 2150. (b) Chen, X.; Tam, U. C.; Czlapinski, J. L.; Lee, G. S.; Rabuka, D.; Zettl, A.; Bertozzi, C. R. *J. Am. Chem. Soc.* **2006**, *128*, 6292.

(91) (a) Luo, P. G.; Wang, H.; Gu, L.; Lu, F.; Lin, Y.; Christensen, K. A.; Yang, S. T.; Sun, Y. P. *ACS Nano* **2009**, *3*, 3909. (b) Gu, L.; Luo, P. G.; Wang, H.; Meziani, M. J.; Lin, Y.; Veca, L. M.; Cao, L.; Lu, F.; Wang, X.; Quinn, R. A.; Wang, W.; Zhang, P.; Lacher, S.; Sun, Y. P. *Biomacromolecules* **2008**, *9*, 2408.

(92) Sudibya, H. G.; Ma, J.; Dong, X.; Ng, S.; Li, L.; Liu, X.; Chen, P. *Angew. Chem., Int. Ed.* **2009**, *48*, 2723.

(93) (a) Bradley, K.; Briman, M.; Star, A.; Grüner, G. *Nano Lett.* **2004**, *4*, 253. (b) Ménard-Moyon, C.; Kostarelos, K.; Prato, M.; Bianco, A. *Chem. Biol.* **2010**, *17*, 107. (c) Star, A.; Gabriel, J. C. P.; Bradley, K.; Grüner, G. *Nano Lett.* **2003**, *3*, 459. (d) Shim, M.; Kam, N.; Chen, R.; Li, Y.; Dai, H. *Nano Lett.* **2002**, *2*, 285. (e) Heller, I.; Janssens, A.; Männik, J.; Minot, E.; Lemay, S. G.; Dekker, C. *Nano Lett.* **2008**, *8*, 591.

(94) (a) Gilboa-Garber, N. *Methods Enzymol.* **1982**, *83*, 378. (b) Imberty, A.; Wimmerová, M.; Mitchell, E. P.; Gilboa-Garber, N. *Microbes Infect.* **2004**, *6*, 221.

(95) Chemani, C.; Imberty, A.; de Bentzman, S.; Pierre, P.; Wimmerová, M.; Guery, B. P.; Faure, K. *Infect. Immun.* **2009**, *77*, 2065.

(96) (a) Mitchell, E.; Houles, C.; Sudakevitz, D.; Wimmerova, M.; Gautier, C.; Pérez, S.; Wu, A. M.; Gilboa-Garber, N.; Imberty, A. *Nat. Struct. Biol.* **2002**, *9*, 918. (b) Cioci, G.; Mitchell, E. P.; Gautier, C.; Wimmerova, M.; Sudakevitz, D.; Pérez, S.; Gilboa-Garber, N.; Imberty, A. *FEBS Lett.* **2003**, *555*, 297.

(97) Hardman, K. D.; Ainsworth, C. F. *Biochemistry* **1972**, *11*, 4910.

(98) Minot, E. D.; Janssens, A. M.; Heller, I.; Heering, H. A.; Dekker, C.; Lemay, S. G. *Appl. Phys. Lett.* **2007**, *91*, 093507.

(99) Hecht, D. S.; Ramirez, R. J.; Briman, M. J.; Artukovic, E.; Chichak, K. S.; Stoddart, J. S.; Grüner, G. *Nano Lett.* **2006**, *6*, 2031.

(100) (a) Kauffman, D. R.; Kuzmych, O.; Star, A. *J. Phys. Chem. C* **2007**, *111*, 3539. (b) Kauffman, D. R.; Sorescu, D. C.; Schofield, D. P.; Allen, B. L.; Jordan, K. D.; Star, A. *Nano Lett.* **2010**, *10*, 958. (c) Kauffman, D. R.; Star, A. *J. Phys. Chem. C* **2008**, *112*, 4430.

(101) (a) Seo, J. H.; Kim, C. P.; Hwang, B. H.; Cha, H. J. *Nanotechnology* **2010**, *21*, 215101. (b) Gondran, C.; Dubois, M. P.; Fort, S.; Cosnier, S.; Szunerits, S. *Analyst* **2008**, *133*, 206. (c) Szunerits, S.; Niedziołka-Jonsson, J.; Boukherroub, R.; Woisel, P.; Baumann, J. S.; Siriwardena, A. *Anal. Chem.* **2010**, *82*, 8203. (d) Sugawara, K.; Shirotori, T.; Hirabayashi, G.; Kuramitz, H.; Tanaka, S. *J. Electroanal. Chem.* **2004**, *568*, 7. (e) Hone, D. C.; Haines, A. H.; Russell, D. A. *Langmuir* **2003**, *19*, 7141.

(102) Cecioni, S.; Faure, S.; Darbost, U.; Bonnamour, I.; Parrot-Lopez, H.; Roy, O.; Taillefumier, C.; Wimmerová, M.; Praly, J.; Imberty, A.; Vidal, S. *Chem. Eur. J.* **2011**, *17*, 2146.

(103) Balavoine, F.; Schultz, P.; Richard, C.; Mallouh, V.; Ebbesen, T. W.; Mioskowski, C. *Angew. Chem., Int. Ed.* **1999**, *38*, 1912.

(104) Tanaka, H.; Yajima, T.; Matsumoto, T.; Otsuka, Y.; Ogawa, T. *Adv. Mater.* **2006**, *18*, 1411.

(105) Shoham, M.; Yonath, A.; Sussman, J. L.; Moult, J.; Traub, W.; Kalb, A. J. *J. Mol. Biol.* **1979**, *131*, 137.

(106) Waner, M. J.; Gilchrist, M.; Schindler, M.; Dantus, M. *J. Phys. Chem. B* **1998**, *102*, 1649.

(107) Chen, Y.; Vedala, H.; Kotchey, G. P.; Audfray, A.; Cecioni, S.; Imberty, A.; Vidal, S.; Star, A. *ACS Nano* **2011**, *6*, 760.

(108) (a) Star, A.; Gabriel, J. C. P.; Bradley, K.; Grüner, G. *Nano Lett.* **2003**, *3*, 459. (b) Zhang, B.; Cui, T. *Appl. Phys. Lett.* **2011**, *98*, 073116. (c) Dong, X.; Shi, Y.; Huang, W.; Chen, P.; Li, L. J. *Adv. Mater.* **2010**, *22*, 1649.

(109) Sharon, N. *Adv. Exp. Med. Biol.* **1996**, *408*, 1.

(110) Assali, M.; Leal, M.; Fernández, I.; Romero-Gomez, P.; Baati, R.; Khiar, N. *Nano Res.* **2010**, *3*, 764.

(111) (a) Holder, P. G.; Francis, M. B. *Angew. Chem., Int. Ed.* **2007**, *46*, 4370. (b) Prencipe, G.; Tabakman, S. M.; Welsher, K.; Liu, Z.; Goodwin, A. P.; Zhang, L.; Henry, J.; Dai, H. *J.*

Am. Chem. Soc. **2009**, *131*, 4783. (c) Simmons, T. J.; Bult, J.; Hashim, D. P.; Linhardt, R. J.; Ajayan, P. M. *ACS Nano* **2009**, *3*, 865.

(112) (a) Imberty, A.; Wimmerová, M.; Mitchell, E. P.; Gilboa-Garber, N. *Microbes Infect.* **2004**, *6*, 221. (b) Chemani, C.; Imberty, A.; de Bentzman, S.; Pierre, P.; Wimmerová, M.; Guery, B. P.; Faure, K. *Infect. Immun.* **2009**, *77*, 2065.

(113) Bodey, G. P.; Bolivar, R.; Fainstein, V.; Jadeja, L. *Rev. Infect. Dis.* **1983**, *5*, 279.

(114) (a) Mitchell, E.; Houles, C.; Sudakevitz, D.; Wimmerova, M.; Gautier, C.; Pérez, S.; Wu, A. M.; Gilboa-Garber, N.; Imberty, A. *Nat. Struct. Biol.* **2002**, *9*, 918. (b) Cioci, G.; Mitchell, E. P.; Gautier, C.; Wimmerova, M.; Sudakevitz, D.; Pérez, S.; Gilboa-Garber, N.; Imberty, A. *FEBS Lett.* **2003**, *555*, 297.

(115) (a) Li, D.; Müller, M. B.; Gilje, S.; Kaner, R. B.; Wallace, G. G. *Nat. Nanotechnol.* **2008**, *3*, 101. (b) Kovtyukhova, N. I.; Ollivier, P. J.; Martin, B. R.; Mallouk, T. E.; Chizhik, S. A.; Buzaneva, E. V.; Gorchinskiy, A. D. *Chem. Mater.* **1999**, *11*, 771.

(116) (a) Blanchard, B.; Nurisso, A.; Hollville, E.; Tétaud, C.; Wiels, J.; Pokorna, M.; Wimmerova, M.; Varrot, A.; Imberty, A. *J. Mol. Biol.* **2008**, *383*, 837. (b) Mitchell, E. P.; Sabin, C.; Snajdrova, L.; Budova, M.; Perret, S.; Gautier, C.; Hofr, C.; Gilboa-Garber, N.; Koča, J.; Wimmerová, M. *Proteins* **2005**, *58*, 735.

(117) Vijayaraghavan, A.; Sciascia, C.; Dehm, S.; Lombardo, A.; Bonetti, A.; Ferrari, A. C.; Krupke, R. *ACS Nano* **2009**, *3*, 1729.

(118) Allen, B. L.; Kotchey, G. P.; Chen, Y.; Yanamala, N. V. K.; Klein-Seetharaman, J.; Kagan, V. E.; Star, A. *J. Am. Chem. Soc.* **2009**, *131*, 17194.

(119) Clark, M.; Cramer, R. D.; van Opdenbosch, N. *J. Comput. Chem.* **1989**, *10*, 982.

(120) Cecioni, S.; Lalor, R.; Blanchard, B.; Praly, J. P.; Imberty, A.; Matthews, S. E.; Vidal, S. *Chem.—Eur. J.* **2009**, *15*, 13232.

(121) (a) Meldal, M.; Tornoe, C. W. *Chem. Rev.* **2008**, *108*, 2952. (b) Rostovtsev, V. V.; Green, L. G.; Fokin, V. V.; Sharpless, K. B. *Angew. Chem., Int. Ed.* **2002**, *41*, 2596. (c) Tornoe, C. W.; Christensen, C.; Meldal, M. *J. Org. Chem.* **2002**, *67*, 3057.

(122) Ahlborn, C.; Siegmund, K.; Richert, C. *J. Am. Chem. Soc.* **2007**, *129*, 15218.

(123) (a) Bouillon, C.; Meyer, A.; Vidal, S.; Jochum, A.; Chevolot, Y.; Cloarec, J. P.; Praly, J. P.; Vasseur, J. J.; Morvan, F. *J. Org. Chem.* **2006**, *71*, 4700. (b) Morvan, F.; Meyer, A.; Jochum, A.; Sabin, C.; Chevolot, Y.; Imberty, A.; Praly, J. P.; Vasseur, J. J.; Souteyrand, E.; Vidal, S. *Bioconjugate Chem.* **2007**, *18*, 1637. (c) Moni, L.; Pourceau, G.; Zhang, J.; Meyer, A.; Vidal, S.; Souteyrand, E.; Dondoni, A.; Morvan, F.; Chevolot, Y.; Vasseur, J. J. *ChemBioChem* **2009**, *10*, 1369. (d) Cecioni, S.; Faure, S.; Darbost, U.; Bonnamour, I.; Parrot-Lopez, H.; Roy, O.; Taillefumier, C.; Wimmerová, M.; Praly, J. P.; Imberty, A. *Chem.—Eur. J.* **2011**, *17*, 2146.

(124) (a) Tang, Y.; Kotchey, G. P.; Vedala, H.; Star, A. *Electroanalysis* **2011**, *23*, 870. (b) Wanekaya, A.; Chen, W.; Myung, N.; Mulchandani, A. *Electroanalysis* **2006**, *18*, 533.

(125) (a) Stoitsova, S. R.; Boteva, R. N.; Doyle, R. J. *Biochim. Biophys. Acta* **2003**, *1619*, 213. (b) Garber, N.; Guempel, U.; Belz, A.; Gilboa-Garber, N.; Doyle, R. J. *Biochim. Biophys. Acta* **1992**, *1116*, 331.

(126) (a) Kadam, R. U.; Bergmann, M.; Hurley, M.; Garg, D.; Cacciarini, M.; Swiderska, M. A.; Nativi, C.; Sattler, M.; Smyth, A. R.; Williams, P. *Angew. Chem., Int. Ed.* **2011**, *50*, 10631. (b) Chabre, Y. M.; Giguère, D.; Blanchard, B.; Rodrigue, J.; Rocheleau, S.; Neault, M.; Rauthu, S.; Papadopoulos, A.; Arnold, A. A.; Imberty, A. *Chem.—Eur. J.* **2011**, *17*, 6545.

(127) Sicard, D.; Cecioni, S.; Iazykov, M.; Chevolot, Y.; Matthews, S. E.; Praly, J. P.; Souteyrand, E.; Imberty, A.; Vidal, S.; Phaner-Goutorbe, M. *Chem. Commun.* **2011**, 9483.

(128) Sabin, C.; Mitchell, E. P.; Pokorna, M.; Gautier, C.; Utille, J. P.; Wimmerova, M.; Imberty, A. *FEBS Lett.* **2006**, *580*, 982.

(129) Kulagina, N. V.; Shaffer, K. M.; Anderson, G. P.; Ligler, F. S.; Taitt, C. R. *Anal. Chim. Acta* **2006**, *575*, 9.

(130) Mannoor, M. S.; Zhang, S.; Link, A. J.; McAlpine, M. C. *Proc. Natl. Acad. Sci. USA* **2010**, *107*, 19207.

(131) Kulagina, N. V.; Lassman, M. E.; Ligler, F. S.; Taitt, C. R. *Anal. Chem.* **2005**, *77*, 6504.

(132) Strauss, J.; Kadilak, A.; Cronin, C.; Mello, C. M.; Camesano, T. A. *Colloids Surf., B* **2010**, *75*, 156.

(133) Villamizar, R. A.; Maroto, A.; Rius, F. X.; Inza, I.; Figueras, M. J. *Biosens. Bioelectron.* **2008**, *24*, 279.

(134) Zelada-Guillén, G. A.; Riu, J.; Düzgün, A.; Rius, F. X. *Angew. Chem. Int. Ed.* **2009**, *48*, 7334.

(135) (a) Huang, Y.; Dong, X.; Liu, Y.; Li, L.-J.; Chen, P. *J. Mater. Chem.* **2011**, *21*, 12358. (b) Mannoor, M. S.; Tao, H.; Clayton, J. D.; Sengupta, A.; Kaplan, D. L.; Naik, R. R.; Verma, N.; Omenetto, F. G.; McAlpine, M. C. *Nat. Commun.* **2012**, *3*, 763.